

Development of Model-Based Correction Methods for Temperature-Dependent Electromagnetic Induction (EMI) Measurement Errors in Soil Conductivity Estimations

Tazifor Martial Tchantcho Amin

Energie & Umwelt / Energy & Environment

Band / Volume 633

ISBN 978-3-95806-761-5

Forschungszentrum Jülich GmbH
Zentralinstitut für Engineering, Elektronik und Analytik (ZEA)
Systeme der Elektronik (ZEA-2)

Development of Model-Based Correction Methods for Temperature-Dependent Electromagnetic Induction (EMI) Measurement Errors in Soil Conductivity Estimations

Tazifor Martial Tchantcho Amin

Schriften des Forschungszentrums Jülich
Reihe Energie & Umwelt / Energy & Environment

Band / Volume 633

ISSN 1866-1793

ISBN 978-3-95806-761-5

Bibliografische Information der Deutschen Nationalbibliothek.
Die Deutsche Nationalbibliothek verzeichnet diese Publikation in der
Deutschen Nationalbibliografie; detaillierte Bibliografische Daten
sind im Internet über <http://dnb.d-nb.de> abrufbar.

Herausgeber und Vertrieb: Forschungszentrum Jülich GmbH
Zentralbibliothek, Verlag
52425 Jülich
Tel.: +49 2461 61-5368
Fax: +49 2461 61-6103
zb-publikation@fz-juelich.de
www.fz-juelich.de/zb

Umschlaggestaltung: Grafische Medien, Forschungszentrum Jülich GmbH

Druck: Grafische Medien, Forschungszentrum Jülich GmbH

Copyright: Forschungszentrum Jülich 2024

Schriften des Forschungszentrums Jülich
Reihe Energie & Umwelt / Energy & Environment, Band / Volume 633

D 464 (Diss. Duisburg-Essen, Univ., 2023)

ISSN 1866-1793
ISBN 978-3-95806-761-5

Vollständig frei verfügbar über das Publikationsportal des Forschungszentrums Jülich (JuSER)
unter www.fz-juelich.de/zb/openaccess.



This is an Open Access publication distributed under the terms of the [Creative Commons Attribution License 4.0](https://creativecommons.org/licenses/by/4.0/), which permits unrestricted use, distribution, and reproduction in any medium, provided the original work is properly cited.

*Research is to see what everybody else has seen,
and to think what nobody else has thought.*

Albert Szent-Gyorgyi

Hiermit versichere ich, die vorliegende Dissertation selbstständig, ohne fremde Hilfe und ohne Benutzung anderer als den angegebenen Quellen angefertigt zu haben. Alle aus fremden Werken direkt oder indirekt übernommenen Stellen sind als solche gekennzeichnet. Die vorliegende Dissertation wurde in keinem anderen Promotionsverfahren eingereicht. Mit dieser Arbeit strebe ich die Erlangung des akademischen Grades Doktor der Ingenieurwissenschaften (Dr.-Ing.) an.

Ort, Datum

Author name (on the line the signature)

Acknowledgments

The presented thesis is developed and accomplished in the Central Institute of Engineering, Electronics and Analytics - Electronic Systems (ZEA-2) in cooperation with the Institute of Bio- and Geosciences - Agrosphere (IGB-3) of Research Center Juelich. I thank ZEA-2 and IGB-3 for all the support they provided during my doctoral research period.

I would like to express my deepest gratitude to my scientific advisor, Dr. Egon Zimmermann, who is always humorous and inspiring which makes him very approachable. His kindness, patience and meticulousness helped to guide me out from confusions and paved the way for solving challenging questions. He is always ready to assist which helped me overcome all the difficulties experienced during my thesis work.

I also take this opportunity to thank his close collaborator and my academic co-advisor Prof. Dr. Johan Alexander Huisman for his enthusiasm during each discussion, for his fruitful ideas pop-up which broke the barriers standing ahead of my research, and for his precise attitude on scientific research and reporting from which I greatly benefited.

I thank my academic advisor and the director of ZEA-2 Prof. Dr.-Ing. Stefan van Waasen who offered me this great opportunity to do my doctoral research in ZEA-2 and gave me such a great chance to work with all my colleagues. I also thank him for his refined guidance on my research and for giving me the opportunity to gather some pedagogical experience through interactions with students during my project work.

I thank my project leader M.Eng Markus Dick in ZEA-2, who is always in a jovial mood and ready to help as well as advice. I also thank our team members Mr. Walter Glaas and Dip.-Ing. Michael Ramm, who helped me a lot during the data measurement process by ensuring that the measurement device was always functional. It is a great experience to work in this lovely team.

I thank Dr. Achim Mester for his patience, understanding and detailed feedbacks on this thesis report, paper manuscripts, presentations and posters. I thank him for all his interesting ideas and helpful suggestions. I will also like to extend my gratitude to Dipl.-Ing. Tom Neubert who assisted me to review my first paper manuscript and who has always readily offered new ideas that could help improve my work. I thank my fellow PhD researchers Leon Steinbeck and Josua Florczak for suffering together through out our PhD projects.

I thank the ZEA-2 administration and IT department for the immense work they do behind the scenes to ensure that my fellow colleagues and I can complete our projects with success.

Finally, I would like to thank my dear mother Marceline Batomou, my late father David A. Tazifor and my beloved wife Odelfa Tsankeu. Their unconditional love and support helped to see me through to the finish line.

Abstract

Electromagnetic induction (EMI) systems are used for mapping of the soil electrical conductivity in near surface applications. Data measured using EMI systems are known to be susceptible to measurement influences associated with time-varying external ambient factors. Temperature variation is one of the most prominent factors causing drift in EMI data, making it challenging to obtain stable and reliable data from EMI measurements.

To mitigate these temperature drift effects, it is customary to perform a temperature drift calibration of the instrument in a temperature-controlled environment. This involves recording the apparent electrical conductivity (ECa) values at specific temperatures and the occurring drift is determined through a static thermal ECa drift correction. However static drift correction does not account for the delayed thermal variations of the system components.

In this thesis report, a novel correction method is presented that accounts for delayed thermal variations of EMI systems components by modelling the dynamic characteristics of drifts using low-pass filters (LPF) and utilises it for correction. The method is developed and tested using a customised EMI device with an intercoil spacing of 1.2 m, optimised for low drift and equipped with temperature sensors that simultaneously measure the local internal temperature across the device during measurements. The device is used to perform outdoor calibration measurements over several days for a wide range of temperature conditions ranging from 10 – 50 °C.

Scenarios with uniform and non-uniform temperature distributions in the measurement device are both considered. To parameterise the proposed correction approaches, two optimisation algorithms notably the Nelder-Mead simplex method and the Shuffled Complex Evolution (SCE-UA) were used respectively for efficient estimation of the calibration parameters. The drift model with one LPF is applied in a first scenario to 16 datasets. During the measurements, the temperature distribution in the device were uniform. Results from the first scenario shows that the measured temperature dependent ECa drift of the system without corrections is approximately $2.27 \text{ mSm}^{-1}\text{K}^{-1}$ with a standard deviation (std) of only $30 \text{ mSm}^{-1}\text{K}^{-1}$ for a temperature variation of around 30 K. The use of the novel correction method reduces the overall root mean square error (RMSE) for all datasets from 15.7 mSm^{-1} to a value of only 0.48 mSm^{-1} . In comparison, a method using a purely static characterization of drift could only reduce the error to an RMSE of 1.97 mSm^{-1} .

In the second scenario, the drift model is extended to two LPFs and applied to 15 datasets. The resulting drift effects were more complex and challenging to correct as they were acquired when the measurement instrument was partially shaded and the temperature distribution in the instrument was non-uniform. It is observed from the results obtained that the arising drifts which could not be corrected by a previous scenario with one LPF are now corrected satisfactorily with the current method. Corrections with the presented drift model resulted in a RMSE of $<1 \text{ mSm}^{-1}$ for all 15 measurements. This shows that the drift model can properly describe the drift of the measurement device. Performing a drift correction simultaneously for all datasets resulted in a RMSE $<1.2 \text{ mSm}^{-1}$, which is even significantly better than the RMSE values of up to 4.5 mSm^{-1} obtained when using only a single LPF in this scenario to perform drift corrections.

The results show that modeling the dynamic thermal characteristics of the drift helps to improve the accuracy in comparison to a purely static characterization. It is concluded that the modeling of the dynamic thermal characteristics of EMI systems is relevant and effective for mitigating temperature drift effects.

Keywords: electromagnetic induction (EMI); temperature drift correction; low-pass filter (LPF); geoscience; apparent electrical conductivity (ECa); root mean square error (RMSE); geophysics.

Zusammenfassung

Elektromagnetische Induktionssysteme (EMI) werden für die Erfassung der elektrischen Leitfähigkeit des Bodens bei bodennahen Anwendungen eingesetzt. Es ist bekannt, dass die mit EMI-Systemen gemessenen Daten anfällig für Messeinflüsse sind, die mit zeitlich variierenden externen Umgebungsfaktoren zusammenhängen. Temperaturschwankungen sind einer der wichtigsten Faktoren, die eine Drift in den EMI-Daten verursachen, was es schwierig macht, stabile und zuverlässige Daten aus EMI-Messungen zu erhalten.

Um diese Temperaturdrifteffekte abzuschwächen, ist es üblich, eine Temperaturdriftkalibrierung des Geräts in einer temperaturgeregelten Umgebung durchzuführen. Dabei werden die Werte der scheinbaren elektrischen Leitfähigkeit (ECa) bei bestimmten Temperaturen aufgezeichnet, und die auftretende Drift wird durch eine statische thermische ECa-Driftkorrektur bestimmt. Die statische Driftkorrektur berücksichtigt jedoch nicht die verzögerten thermischen Schwankungen der Systemkomponenten.

In dieser Arbeit wird eine neuartige Korrekturmethode vorgestellt, die verzögerte thermische Schwankungen der Komponenten von EMI-Systemen berücksichtigt, indem die dynamischen Eigenschaften von Driften mit Hilfe von Tiefpassfiltern (TPF) modelliert und zur Korrektur verwendet werden. Die Methode wurde unter Verwendung eines benutzerdefinierten EMI-Geräts mit einem Spulenabstand von 1,2 m entwickelt und getestet, das für eine geringe Drift optimiert wurde und mit Temperatursensoren ausgestattet ist, die während der Messungen gleichzeitig die lokale Innentemperatur im Gerät messen. Das Gerät wurde für mehrtägige Kalibrierungsmessungen im Freien bei einer breiten Spanne von Temperaturen zwischen 10 – 50 °C eingesetzt.

Es werden sowohl Szenarien mit gleichmäßigen als auch mit ungleichmäßigen Temperaturverteilungen im Messgerät betrachtet. Zur Parametrisierung der vorgeschlagenen Korrekturansätze wurden zwei Optimierungsalgorithmen, insbesondere die Nelder-Mead-Simplex-Methode und die Shuffled Complex Evolution (SCE-UA), für eine effiziente Schätzung der Kalibrierungsparameter verwendet. Das Driftmodell mit einem TPF wird in einem ersten Szenario auf 16 Datensätze angewendet. Während der Messungen war die Temperaturverteilung im Gerät gleichmäßig. Die Ergebnisse des ersten Szenarios zeigen, dass die gemessene temperaturabhängige ECa-Drift des Systems ohne Korrekturen etwa $2,27 \text{ mSm}^{-1}\text{K}^{-1}$ mit einer Standardabweichung (std) von nur $30 \text{ mSm}^{-1}\text{K}^{-1}$ bei einer Temperaturvariation von etwa 30 K beträgt. Die Verwendung der neuen Korrekturmethode reduziert den mittleren quadratischen Gesamtfehler (RMSE) für alle Datensätze von $15,7 \text{ mSm}^{-1}$ auf einen Wert von nur $0,48 \text{ mSm}^{-1}$.

Im Vergleich dazu könnte eine Methode, die eine rein statische Charakterisierung der Drift verwendet, den Fehler nur auf einen RMSE von $1,97 \text{ mSm}^{-1}$ reduzieren.

Im zweiten Szenario wird das Driftmodell auf zwei TPFs erweitert und auf 15 Datensätze angewendet. Die daraus resultierenden Drifteffekte waren komplexer und schwieriger zu korrigieren, da sie bei teilweise abgeschattetem Messgerät und ungleichmäßiger Temperaturverteilung im Gerät erfasst wurden. Aus den Ergebnissen geht hervor, dass die auftretenden Driften, die in dem früheren Szenario mit einem TPF nicht korrigiert werden konnten, nun mit der aktuellen Methode ausreichend korrigiert werden können. Die Korrekturen mit dem vorgestellten Driftmodell ergaben einen RMSE von $<1 \text{ mSm}^{-1}$ für alle 15 Messungen. Dies zeigt, dass das Driftmodell die Drift des Messgerätes sehr gut beschreiben kann. Die gleichzeitige Durchführung einer Driftkorrektur für alle Datensätze führte zu einem RMSE von $<1,2 \text{ mSm}^{-1}$, was deutlich besser ist als die RMSE-Werte von bis zu $4,5 \text{ mSm}^{-1}$, die bei der Durchführung von Driftkorrekturen in diesem Szenario mit nur einer einzigen TPF erzielt wurden.

Die Ergebnisse zeigen, dass die Modellierung der dynamischen thermischen Eigenschaften der Driften zu einer Verbesserung der Genauigkeit im Vergleich zu einer rein statischen Charakterisierung beiträgt. Daraus wird geschlossen, dass die Modellierung der dynamischen thermischen Eigenschaften von EMI-Systemen für die Minimierung von Temperaturdrifteffekten relevant und wirksam ist.

Schlüsselwörter: Elektromagnetische Induktion (EMI); Temperaturdriftkorrektur; Tiefpassfilter (TPF); Geowissenschaften; scheinbare elektrische Leitfähigkeit (ECa); mittlerer quadratischer Fehler (RMSE); Geophysik.

List of Publications

Parts of this doctoral thesis have been published, or will be used for future publications. The following list gives an overview of current publications in which parts of this dissertation have been published or are planned for publication.

Journals

M. Tazifor, E. Zimmermann, J. A. Huisman, M. Dick, A. Mester and S. van Waasen: Model-Based Correction of Temperature-Dependent Measurement Errors in Frequency Domain Electromagnetic Induction (FDEMI) Systems. In: *Sensors* 22 (2022), 05, S. 3882

M. Tazifor, E. Zimmermann, J. A. Huisman, M. Dick, A. Mester and S. van Waasen: Low-pass Filters for a Temperature Drift Correction Method for Electromagnetic Induction Systems. In: *Sensors* 23.17 (2023). issn: 1424-8220. doi: 10.3390/s23177322.

Conferences

M. Tazifor, E. Zimmermann, J. A. Huisman, M. Dick, A. Mester and S. van Waasen: Model-Based Correction Method for Temperature-dependent Measurement Errors in EMI Systems. In: *World Multidisciplinary Earth Sciences Symposium (WMESS 2020)*

M. Tazifor, E. Zimmermann, J. A. Huisman, M. Dick, A. Mester and S. van Waasen: Correction Method for Temperature-dependent Measurement Errors in EMI Systems. In: *Studiengruppe für Elektronische Instrumentierung der Helmholtz-Zentren (SEI-Tagung 2022)*

M. Tazifor, E. Zimmermann, J. A. Huisman, M. Dick, A. Mester and S. van Waasen: Dynamic drift correction method for temperature-dependent measurement deviations in electromagnetic induction systems. In: *Near Surface geoscience - EAGE (NSG-EAGE 2022)*

M. Tazifor, E. Zimmermann, J. A. Huisman, M. Dick, A. Mester and S. van Waasen: Drift Correction Method for Temperature-dependent Measurement Errors in Elec-

tromagnetic Induction Systems. In: Helmholtz Energy Young Scientists Workshop
Frankfurt

List of Figures

2.1.	Basic set-up of an electromagnetic induction (EMI) system.	12
2.2.	Vertical coplanar coil (VCP), horizontal coplanar coil (HCP) and perpendicular coil (PRP) configurations.	14
2.3.	(a) Plot of local-sensitivity curves. (b) Equivalent cumulative response curves vs. normalised depth h/x	15
2.4.	Representation of a three-layered soil model for EMI instrument calibration.	17
3.1.	Nelder–Mead approach with original simplex shown with a dashed line ($x_1-x_2-x_3$) (adaptation from Lagarias et al. [86]).	20
3.2.	A diagram outlining the steps of the SCE inversion algorithm used to process EMI data.	25
3.3.	Signal flow diagram of the first order IIR filter used to model the present and past temperature delay dynamics of the measurement instrument.	28
3.4.	The provided plot shows cubic spline interpolation using three reference points within a chosen temperature range.	30
4.1.	(a) Picture of the EMI instrument used to perform measurements. (b) simplified schematic diagram of the EMI measurement system.	34
4.2.	(a) The signal flow diagram depicts the EMI measurement system’s set-up for a single Tx – Rx arrangement. (b) Magnitude and phasor diagram for the primary, secondary and measured magnetic fields.	36
4.3.	The left axis shows the time series of the measured phase (black broken line). The right axis shows time series of the local internal (air) temperature (red solid line) from sensor 3.	38
4.4.	Schematic representation of the phase drift model with static modeling (red path) and dynamic modeling (blue path) options.	39
4.5.	Time series of measured temperature values, T_{ms} for calibration measurement #16.	43
4.6.	(a) Uncorrected ECa values for calibration measurement #16. (b) Corrected ECa values for measurement #16. ECa values were shifted to have a zero mean.	46
4.7.	Plot for calibration measurement #16 showing ECa as a function of temperature.	48

4.8. (a) Plot of static drift correction (without LPF) and (b) Plot of dynamic drift correction (utilizing LPF). ECa values were shifted to have a zero mean.	50
5.1. (a) Photo of the modified custom EMI instrument; (b) Simplified schematic representation of the measurement system.	54
5.2. Representation of the phase drift model for temperature drift correction.	56
5.3. Representation of root mean square error (RMSE) between modelled and measured temperatures.	60
5.4. Plot of the first eigenvalue for all datasets obtained from principal component analysis (PCA) on time series of temperature sensors 3 and 9.	61
5.5. Correlation between the calibration parameters G_1 and G_2 showing all parameter combinations for $RMSE$ values less than 1 mSm^{-1}	62
5.6. Time series of measured apparent electrical conductivity (ECa_{ms}) and modelled apparent electrical conductivity (ECa_{mod}) for 15 datasets. ECa values were shifted to have a zero mean.	65
5.7. Root mean square errors (RMSE) from fitting with temperature sensors 3 and 9 using calibration strategy types A-C.	66
5.8. Modelled apparent electrical conductivity and measured apparent electrical conductivity versus the mean of temperatures 3 and 9 for type A. ECa values were shifted to have a zero mean.	67
5.9. Modelled apparent electrical conductivity and measured apparent electrical conductivity versus the mean of temperatures 3 and 9 for type B. ECa values were shifted to have a zero mean.	69
5.10. Modelled apparent electrical conductivity and measured apparent electrical conductivity versus the mean of temperatures 3 and 9 for type C. ECa values were shifted to have a zero mean.	71
B.1. Plot of uncorrected ECa over time for 16 datasets.	92
B.2. Plot of corrected ECa over time for 16 datasets after static correction.	93
B.3. Plot of corrected ECa over time for 16 datasets after dynamic correction.	94
C.1. Plot of the residual eigenvalues ($1 - E_{val,1N}$) for all datasets obtained from principal component analysis (PCA).	95
C.2. Corrected ECa obtained through simplex fitting with 1 LPF.	96
C.3. Corrected ECa obtained through SCE fitting with 1 LPF.	96

List of Tables

1.1. Some commercial EMI devices used in soil prospecting [66, 67, 68, 69]	4
4.1. The calibration parameters: time constant (τ), gain (G which is converted to ECa), and non-linear term (NL) were determined from fitting the 16 datasets. The corresponding $RMSE_1$ (from correcting each individual dataset with its own fitted calibration parameter) and $RMSE_2$ (from the evaluated mean of all 16 calibration parameters which is applied for correction of each individual dataset) were also determined. The mean and standard deviation (std) of the calibrated parameters based on the 16 measurements were also calculated.	45
5.1. Boundary for the time constant (τ) and gain (G) calibration parameters before and after fitting	63
5.2. Calibration parameters obtained with calibration strategy B and C.	67

List of Symbols

Symbols with Latin letters

Symbol	Denomination	IS Unit	Definition
a_1	Filter coefficient	-	Eq. (3.15)
b_0, b_1	Filter coefficients	-	Eq. (3.15)
C	Covariance matrix	K	Eq. (3.21)
CRF	Cumulative response function	mSm^{-1}	Eq. (2.6)
ECa	Apparent electrical conductivity	mSm^{-1}	Eq. (2.5)
H_a	Analog LPF transfer function	-	Eq. (3.12)
H_d	Digital LPF transfer function	-	Eq. (3.14)
$RMSE$	Root mean square error	$rad(mSm^{-1})$	Eq. (5.2)
s	Laplace operator	-	Eq. (3.13)
T_{mod}	Modelled temperature	K	Eq. (3.17)

Symbols with Greek letter

Symbol	Denomination	IS Unit	Definition
Φ_{ms}	Measured phase	rad	Eq. (4.2)
τ	Time constant	s	Eq. (3.12)
Φ_c	Corrected phase	rad	Eq. (5.1)

Abbreviations

Abbreviation Denomination

<i>ADC</i>	Analog to digital converter
<i>CCE</i>	Competitive complex evolution
<i>CRF</i>	Cumulative response function
<i>DAQ</i>	Data acquisition
<i>DOI</i>	Depth of investigation
<i>ECa</i>	Apparent electrical conductivity
<i>EMI</i>	Electromagnetic induction
<i>HCP</i>	Horizontal co-planar
<i>LIN</i>	Low-Induction Number
<i>LPF</i>	Low pass filter
<i>LuT</i>	Look-up table
<i>NUTV</i>	Non-uniform temperature variation
<i>PCA</i>	Principal component analysis
<i>PCB</i>	Printed circuit board
<i>RMSE</i>	Root mean square error
<i>Rx</i>	Receiver coil
<i>SCE</i>	Shuffled complex evolution
<i>Tx</i>	Transmitter coil
<i>UTV</i>	uniform temperature variation
<i>VCP</i>	Vertical co-planar

Contents

Acknowledgments	i
Abstract	iii
Zusammenfassung	v
List of publications	vii
List of Figures	xii
List of Tables	xv
List of Symbols	xvii
1. Introduction	1
1.1. Background and Motivation	1
1.2. Brief Overview of Commercial EMI Devices	3
1.3. Static Drift Correction of EMI Data	4
1.4. Objectives and Outline	7
2. Fundamentals	11
2.1. Principle of EMI	11
2.2. Sensitivity of Common Coil Configurations	13
2.3. Local-Sensitivity Model	15
2.4. ECa Calculation	18
3. Theory on Modelling and Optimization of EMI Data	19
3.1. The Nelder-Mead Algorithm	19
3.2. Shuffled Complex Evolution (SCE) Algorithm	22
3.3. Infinite Impulse Response Filter	26
3.4. Phase Value Calculation and Correction	28
3.5. Principal Component Analysis	30
4. Uniform Temperature Drift Correction	33
4.1. Materials and Method	33
4.1.1. EMI Measurement System with Temperature Sensors	33
4.1.2. Temperature Drift	37
4.1.3. Phase Drift Model	39

4.1.4.	Effective Temperature Variation	40
4.1.5.	Drift Calibration Measurements	40
4.1.6.	Effect of Soil Conductivity Changes on the Calibration	42
4.2.	Results and Discussions	43
4.2.1.	Measured Temperature Distribution	43
4.2.2.	Performance of Calibration	44
4.2.3.	Advantage of Implementing the LPF in the Drift Correction Model	47
4.2.4.	Effect of Soil Conductivity Changes on the Calibration	51
5.	Non-uniform Temperature Drift Correction	53
5.1.	Materials and Method	53
5.1.1.	Measurement System	53
5.1.2.	Drift Correction Model	55
5.1.3.	Selection of Temperature Sensors	56
5.1.4.	Assessment of Spatial Temperature Variation	57
5.1.5.	Determination of the Representative Calibration Parameters	58
5.2.	Results and Discussion	60
5.2.1.	Selection of Temperature Sensors	60
5.2.2.	Assessment of Spatial Temperature Variation	61
5.2.3.	Estimation of Calibration Parameter Boundaries	62
5.2.4.	Determination of the Representative Calibration Parameters	63
6.	Conclusions and Outlook	73
6.1.	Uniform Temperature Distributions	73
6.2.	Non-uniform Temperature Distributions	74
6.3.	Outlook	75
	Bibliography	77
	A. Overview of the Maxwell's Equations	89
	B. Static and Dynamic Drift Correction	91
	C. Data Optimisation and Parameter Calculation	95
	Curriculum Vitae	99

1. Introduction

1.1. Background and Motivation

The work presented in this thesis report is focused on the application of research in the field of agriculture. Specifically, the research targets the development and improvement of measurement instruments and methods for investigating the near-surface soil layer, which is also known as the vadose zone. This layer is the outermost cultivated layer of the subsurface that is located above the groundwater table, where the primary activities of plant roots occur [1]. The near-surface soil layer is of critical importance because it is the site of most human activities and the exchange of mass and energy through chemical, biological, and physical processes [2]. Many of these processes depend on soil water dynamics which also has a direct impact on other geophysical applications such as environmental protection [3, 4], soil prospecting applications for various depths of exploration [5, 6] and mineral prospecting [7].

The geophysical methods used to perform these hydrological investigations often use methods to characterise soil properties that influence the soil electrical conductivity. Large geographically related datasets that can be associated with the soil characteristics that either directly or indirectly affect the electrical conductivity of the soil can be easily collected thanks to geophysical techniques [8], mainly categorised into contact-based and contact-free measurement methods. These measurement methods and the accuracy of the electrical conductivity values obtained are influenced by a variety of factors, including soil type, salt content, temperature variability, and soil texture [9]. To better understand the effects of these factors on the measurement devices, it is essential to study them in detail.

The contact-based methods comprise elaborate monitoring set-ups employed in earlier geophysical prospecting and requiring calibration with soil samples. The process of conducting such surveys was laborious, and it was crucial to carefully select representative measurement points in order to accurately extrapolate observation data from a small-scale to larger scales [10]. Furthermore, minimizing soil disturbance is generally preferred in geophysical applications. In addition to direct soil sampling [11, 12], electrical resistivity methods are common, where the subsurface electric field produced by external application of electrical current into the soil through an electrode or soil probe that is galvanically in contact with the soil is measured [13]. Some examples of contact-based methods include vertical electrical sounding, VES [14, 15, 16], time domain reflectometry, TDR [17, 18, 19], electrical resistivity tomography, ERT

[20, 21, 22], capacitance probes [23, 24], spectral induced polarisation, SIP [25, 26], direct current voltage gradient (DCVG) and close interval potential survey (CIPS) [27]. These methods can provide accurate data at specific locations but are limited in terms of sampling volume and mapping speed [28], and are often resource-intensive and may be invasive for repetitive measurements at the same location [11].

The contact-free methods utilise so-called ground conductivity meters to measure the electrical conductivity of a bulk soil volume using electromagnetic fields. They offer the advantage of non-invasive sensing, ease of operation, high mobility and increased speed of soil mapping thanks to the recent inclusion of georeferencing techniques (e.g. global positioning systems, GPS). Typical electromagnetic methods include active microwave, AM [29, 30], passive microwave, PM [31, 32], neutron thermalisation, NT [33, 34], nuclear magnetic resonance, NMR [35], ground-penetrating radar, GPR [36, 37, 38, 39], time-domain transient electromagnetic induction, TEM [40] and frequency-domain electromagnetic induction (EMI) [41]. Whilst TEM methods have been used in geophysical applications with several hundreds of meter depths of investigation [42], EMI methods are more suitable for investigating the upper meters of the soil.

It is in this regard that geophysicists have extensively utilised non-contact frequency domain EMI systems with small coil separations to map the distribution of soil electrical conductivity. Examples including the use of this technique for research are found in the work presented by Heil and Schmidhalter [8], Wait [43] and Robinson et al. [44]. EMI measurements provide a quick and contactless way to measure the soil apparent electrical conductivity (ECa), which is closely linked to the bulk soil electrical conductivity and thus to many soil properties like clay content, salinity, and water content. In this regard, significant advancements have been made in the development of EMI systems and the interpretation of data, and many researchers have applied this technique to investigate various applications. Allred et al. [13] has summarised some of the typical applications of EMI, and Corwin [15], Samouélian et al. [14], and Corwin and Lesch [45] have presented an extensive review on this topic. For instance, in the field of agriculture, Schmäck et al. [46] utilised EMI methods to examine soil bulk density, volumetric soil water content, soil texture, and predict areas of harmful soil compaction.

Additionally, Gebbers et al. [47] studied the effects of seasonal variations and soil physicochemical properties on soil electrical conductivity and its relation to agricultural processes. Many studies have also used EMI measurements for soil mapping in precision agriculture [48, 49, 8, 50]. For instance, Cameron et al. [51], Visconti and De Paz [52], Corwin and Rhoades [53] found that EMI allows for rapid mapping of soil to obtain clear delineations of field-scale salinity profiles. Other EMI studies have aimed to relate EMI measurements to soil water content and groundwater dynamics and to explore their influence on the electrical conductivity data obtained from measurements [54, 55, 56]. For example, Kachanoski et al. [19] used EMI measurements to demonstrate that bulk soil electrical conductivity accounts for up to 96% of

the spatial variation of soil water content. Furthermore, Van't Veen et al. [57] and Altdorff et al. [56] conducted studies to correlate EMI measurements with soil water content and water movement in the vadose zone. Additionally, some studies have used EMI measurements to investigate the impact of soil clay content on the soil electrical conductivity. For instance, EMI measurements were utilised to characterise soil clay content in order to examine soil textural heterogeneity [58], as well as to investigate the vertical variations of magnetic and electrical properties of the subsurface [59].

1.2. Brief Overview of Commercial EMI Devices

In recent years, there has been a significant increase in the number of commercially available EMI devices used in agriculture and soil prospecting. EMI devices were first used in agriculture for salinity studies of the soil, [60]. Initially, single-coil, single-frequency EMI devices like the EM31-MK2 from Geonics and the CMD-1 from GF instruments (shown in Table 1.1) were used in agricultural applications. However, these devices were limited in terms of the depth resolution, which led to the development of multi-coil devices that operate at a fixed frequency.

Examples of such devices include the EM38-MK2 from Geonics, the CMD-MiniExplorer and the CMD-Explorer from GF instruments. It was discovered that there are further benefits to be gained with these multi-coil EMI instruments, [61, 62, 63]. These multi-coil EMI instruments enables sensing over different depth ranges. Additionally, devices were developed that could operate at multiple frequencies with fixed intercoil spacings. For instance, the GEM-2 from Geophex and the profiler EMP-400 from Geophysical Survey System, Inc (GSSI) are examples of such devices. These multi-frequency devices have also become popular in various applications because these also offer the advantage of sensing over different depth ranges [62, 64, 65].

The next generation of EMI instruments combines multi-coil and multi-frequency methods for use in further applications [61, 62, 63]. A popular example of these devices is the EM34-3 from Geonics. The up-till-now discussed devices have a coplanar arrangement between transmitter and receiver coils. Therefore they can only acquire data in a single dipole orientation at a time, i.e. either the vertical coplanar coil (VCP), the horizontal coplanar coil (HCP) or the perpendicular coil (PRP) configuration. There are also systems that combine various coil orientations. Examples of these are dual-dipole devices such as the Dualem-21S and the Dualem-421S. These devices have coils placed in different dipole configurations (notably the HCP and the PRP configurations) and operate at a fixed frequency. The combination of various coil orientation also helps to improve the depth resolution.

The development of these advanced EMI devices allow for non-invasive and efficient investigations of the subsurface properties of the soil, providing valuable insights for agricultural applications such as precision farming and crop yield optimisation.

Table 1.1.: Some commercial EMI devices used in soil prospecting [66, 67, 68, 69]

Device	# of Coils	Frequency	Tx-Rx
	(Tx/Rx)	(kHz)	(m)
EM31-MK2	1/1	9.80	3.66
CMD-1	1/1	10	0.98
EM38-MK2	1/2	14.5	0.5,1
CMD-MiniExplorer	1/3	30	0.32,0.71,1.18
CMD-Explorer	1/3	10	1.48,2.82,4.49
GEM-2	1/1	0.03-93	1.66
Profiler EMP-400	1/1	1-16	1.2
EM34-3	1/3	0.4,1.6,6.4	10,20,40
DUALEM 21s	1/4	9	1,1.1,2,2.1
DUALEM 421s	1/6	9	1,1.1,2,2.1,4,4.1

Additionally, they have proved useful in soil prospecting applications, such as mineral exploration and geological mapping. Despite all the available commercial devices and their respective characteristics, more special devices are required for the constantly developing smart farming applications, with new requirements on the measurement accuracy.

1.3. Static Drift Correction of EMI Data

To ensure a reliable inversion in EMI imaging, it is crucial to obtain accurate and quantitative EMI data without any errors or shifts. However, obtaining true absolute quantitative values of the apparent electrical conductivity is challenging and requires additional measurements or data processing. Consequently, most EMI systems are currently used for qualitative analyses such as subsurface pattern imaging [70] and time-lapse investigations [71]. For EMI systems with coil separations smaller than 2 meters, significant errors of several to dozens of mSm^{-1} have been observed when compared with reference data obtained from soil samples or Electrical Resistivity Tomography (ERT) measurements [72]. This is mainly due to the fact that the magnitude of the electromagnetic response coming from the soil is relatively small for small coil separations (seen later in Equation 2.3). Therefore, any disturbance or error can significantly influence the EMI data and lead to inaccuracies in the inversion process.

Overall for both large and small coil separations and irrespective of the application for

which EMI instruments are utilised, the accuracy of measurements obtained through them has been a topic of concern in numerous studies, as these measurements are vulnerable to systematic errors due to changes in external environmental conditions. For instance, Minsley et al. [73] and Sudduth et al. [74] have pointed out that the drift detected in EMI instruments can be attributed to inaccurate calibration and improper instrument levelling. Nüsch et al. [75] has identified the presence of the operator and cables situated near the measurement system as other sources of systematic error. In addition, EMI devices are prone to deviations, commonly referred to as drifts, which are affected by environmental factors and exhibit unpredictable variations during measurements over time, as noted by Robinson et al. [76] and Delefortrie et al. [77].

One of the most significant factors affecting the accuracy of EMI instruments is temperature. Studies have found that the drift of EMI instruments is largely dependent on temperature, and that even slight temperature changes can significantly affect the accuracy of the measurements obtained [78]. For instance, Huang et al. [78] and Abdu et al. [79] conducted experiments to examine the impact of different temperatures on the drifts detected by EMI instruments. Hanssens et al. [80] employed temperature logging to analyse the drift patterns of various electromagnetic instruments during static ground measurements. Mester et al. [81] identified various factors that could affect the properties of the system hardware, including the thermal drift of coils resulting from local internal temperature variations. Gebbers et al. [47] exposed the EM38 device to varying temperatures during measurements at a fixed position and suggested that the drift effects observed were partly caused by changes in air temperature.

Sudduth et al. [74] investigated the effects of varying external ambient temperatures on the accuracy of measurements obtained using the EM38 instrument. The study found that as the temperature increased from 23°C to 35°C over an 8-hour period, the measured ECa increased from 32.2 mSm⁻¹ to 42.3 mSm⁻¹. This result highlights the need for careful consideration of temperature conditions when conducting EMI measurements. Similarly, Huang et al. [78] further demonstrated that the accuracy of EMI measurements obtained using the DUALEM-41S and DUALEM-21S instruments can also be affected by changes in external ambient temperature. The study found that temperature changes can result in significant variations in the measured ECa, further emphasizing the importance of controlling the environmental conditions when conducting EMI measurements.

The general consensus from all these studies was that it is necessary to find measures to mitigate temperature drifts in EMI data. Several suggestions have been made to reduce the effects of temperature drifts on EMI devices. For instance, Abdu et al. [79] have recommended mapping on cloudy days and that the EMI instruments be protected from direct sunlight. Furthermore, Huang et al. [78] suggested that the instrument should be shaded with a non-conductive thermal insulation. Robinson et

al. [76] attributed the drift effects observed to the differential heating of EMI devices, which results in a non-uniform temperature distribution, making it problematic to correct the resulting drifts. They recommended in addition to shading, that the device should be warmed up for 2 hours prior to data acquisition.

Further attempts to mitigate temperature dependent drifts have utilized local internal temperature compensation circuits of commercial EMI instruments in combination with optimisation techniques [79, 74]. However, despite these efforts, the effect of temperature on measured EMI data has typically not been satisfactorily mitigated. For example, Robinson et al. [76] found that the internal compensation circuit of the EM38 instrument was unable to fully compensate for instrument heating at temperatures above 40°C, suggesting that drifts are influenced by a combination of factors, including circuit design and component performance under heating.

In another study, Mester et al. [81] focused on the electronic components of a custom EMI instrument that has a rigid-boom design. Specifically, they analysed the impact of temperature drift on the performance of the instrument, by conducting laboratory analysis, focusing specifically on a frequency of 8 kHz, and discovered that 88 % of the observed drift in the measured data could be attributed to changes in the impedance of the electrical Tx coil. The remaining 12 % of the drift was caused by fluctuations in the inductance and capacitance of the Tx coil, the impedance of the Rx coil, and drifts in the amplification circuit. They were able to correct for significant drifts in the Rx coils by using measured temperature dependent coil impedances. However, they did not carry out a comprehensive correction for all the drifts that may arise from various system components. Their results suggested that there may be additional sources of drift that were not accounted for in the analysis.

Overall, the findings of their study highlighted the importance of understanding and controlling for temperature drift in EMI instruments, particularly in cases where high accuracy measurements are required. While their study focused on a custom EMI instrument and a specific set of components, the results have implications for EMI instruments more broadly and suggest the need for further research in this area. All of the above-stated studies highlight the complexity of the problem of temperature related drifts in EMI systems and suggest that a more thorough approach may be needed to fully address the issue. To improve the accuracy of EMI systems, one effective method is static drift calibration using a look-up table for the entire EMI instrument. This involves heating the measurement system in a temperature-controlled environment and waiting for it to reach a stable state before taking measurements.

Robinson et al. [76], Abdu et al. [79] and Hanssens et al. [80] performed such measurements and showed that by establishing a look-up table that relates temperature and drift, it is possible to determine the relationship between signal drift and external ambient temperature and obtain corrected EMI measurements. However, this process has some drawbacks. One significant drawback is that deriving such

look-up tables is a time-consuming and cumbersome task, as it requires not only a suitable temperature-controlled room but also careful observation of delay times for attaining steady-state temperatures for each calibration step. Moreover, standard laboratory rooms are unsuitable for this purpose, as they can be influenced by metals and electromagnetic interference, which can interfere with the accuracy of the EMI measurements.

In further attempts to mitigate temperature drift effects, Tan [82] developed a transfer function method that measures the phase response of all circuit components of a custom EMI instrument and identified two types of temperature drifts notably, drifts due to slow uniform temperature variations and drifts resulting from fast temperature variations. The latter type results in different temperature gradients for different system components, which can be problematic when components react with delayed response to fast temperature changes. As a solution for drifts due to fast but uniform temperature variations, they proposed to measure the temperature dependent electrical properties of the coils to compensate for drifts due to slow reactions of the properties to fast temperature changes.

According to Tan [82], a further solution to minimise such drifts during calibration measurements is to use thermal isolation boxes and cooling systems such as a fan in outdoor settings. However, achieving a homogeneous temperature with a high level of accuracy (better than 1 K) in such environments is very challenging. Furthermore, static correcting measurement errors using look-up tables is only effective when the temperature distribution is stable or changes slowly. When the external ambient temperature changes rapidly, correcting for drifts is more challenging. They also demonstrated that there is a delay between instrument temperature and measured ECa, indicating that using look-up tables alone cannot efficiently correct for drifts caused by sudden changes in external ambient temperature. Huang et al. [78] also observed hysteresis effects in temperature dependent drifts, further suggesting that correcting for drifts caused by abrupt changes in external ambient temperature using look-up tables alone is not currently feasible. Therefore, it is important to consider other potential solutions to minimise interferences and improve the accuracy of temperature calibration measurements in outdoor environments.

1.4. Objectives and Outline

The primary objective of this thesis is to create a novel method for correcting temperature dependent drift errors that occur during EMI measurements. These errors are often caused by rapid changes in external ambient temperature, particularly on bright and cloud-free days with local internal temperatures reaching as high as 50°C. To address this issue, the proposed method involves utilising a phase drift model that uses information from temperature sensors to replicate the dynamic drift characteristics of EMI instruments and improve our understanding of how temperature variations

impact EMI measurements.

Furthermore, this new approach offers a straightforward technique for calibrating an EMI system through outdoor measurements. The proposed approach is intended to show that performing a dynamic thermal characterisation of the drift effects will offer much more improved correction accuracy compared to pure static characterisation. By implementing this method, it is expected that EMI measurements will become more accurate and reliable, ultimately improving the overall quality of EMI data.

The thesis is partitioned into five main sections, with the first chapter serving as an introduction. Here, the background and motivation of this thesis project is discussed. Next, an overview of some of the available commercial devices and their applications is provided. The measurement deviations experienced by such devices and the approaches by some researchers to mitigate them is highlighted.

In the second chapter, the fundamentals of EMI systems are explored and presented. Here the functional principles, sensitivity estimation and soil electrical conductivity calculation are discussed. The chapter serves as a foundation for providing a comprehensive understanding of the key principles involved.

In the third chapter of this thesis work, focus is placed on the theory behind EMI data optimisation techniques, unveiling a set of tools and methodologies to enhance the quality and accuracy of EMI measurements. This chapter provides the necessary knowledge to extract meaningful information from EMI data and addresses potential issues such as drift. The chapter also presents the utilization of digital infinite response filters as valuable tools for drift modeling and correction.

In the fourth chapter, the author presents a calibration measurement set-up that is based on a custom-made multi-coil EMI instrument. This chapter details a model-based numerical solution that employs one low pass filter (LPF) to model and quantify the dynamic thermal response of the system components of the EMI instrument to external ambient temperature variations. Its design is intended for use in rigid-boom EMI systems with the transmitter and receiver in one enclosure but eventually also for a modular EMI system in parallel under development, where the transmitter and receiver are in different enclosures. Additionally, the chapter describes the method that was utilised to determine the model calibration parameters that are later employed to correct the EMI data for temperature dependent drifts. This chapter also explains that, in order to gather the temperature information required for drift correction, the EMI instrument is equipped with 10 temperature sensors that simultaneously measure the local internal temperature across the device. As a preliminary analysis, the investigation initially focuses on temperature drift effects resulting from uniform temperature variations (UTV) in the EMI instrument. The effectiveness of drift correction with the dynamic model developed is verified by comparing it with drift correction

using a standard static model based on a look-up table alone. Finally, the main results are presented and discussed, and conclusions are drawn based on the findings of the study. Overall, this chapter serves as a comprehensive guide to the EMI instrument and its calibration process, providing valuable insights into the techniques and tools used to accurately measure and correct for temperature dependent drifts in EMI data.

Chapter 5 of the thesis report details a modified custom-built EMI instrument with eight integrated temperature sensors installed. The purpose of this chapter is to improve upon the drift correction method described in chapter 4, which suffered from inaccuracies resulting from non-uniform temperature variations (NUTV) within the EMI instrument caused by partial shading of the measurement device. To combat this issue, the drift model in chapter 5 utilises two low pass filters to effectively model temperature drift effects. Specifically, these filters account for the impact of NUTV on the EMI instrument's temperature and help to calibrate the drift correction model for optimal performance. This is accomplished through the implementation of a global optimisation method known as the shuffled complex evolution, which allows for the identification and modeling of key parameters that are used to calibrate the drift model. The primary advantage of the improved drift correction method presented in the fifth chapter is its ability to account for NUTV, a factor that was previously unaddressed by the previous method outlined in chapter 4. To evaluate the efficiency of this improved method, it was applied to both datasets with and without uniform temperature variations. The results showed a significant improvement in drift correction accuracy when utilising the new method, further validating its effectiveness. Overall, chapter 5 highlights the significant advancements that have the potential to effectively improve the accuracy and reliability of EMI measurements.

In chapter 6 of this thesis, the main focus is on summarising the key findings and goals that have been achieved through the course of the research. Throughout the thesis, a lot of time and effort has been put into investigating and analysing the various aspects of temperature drift effects on EMI systems, and this chapter uses the chance to highlight the major outcomes of that work. In addition to summarising the key findings of the research, the sixth chapter also presents conclusions that have been drawn based on the series of analyses. These conclusions offer insights into the potential implications of the developed method for the broader field of near-surface geophysics. Furthermore, the chapter provides an outlook for future research and potential areas for improvement in EMI systems drift analysis.

2. Fundamentals

The current chapter aims to elaborate on the theory behind EMI systems and discusses the various coil configurations that are commonly used in EMI surveys, as well as the local sensitivity model which is used to examine how the sensitivity of EMI measurements changes in different areas of a subsurface region. In addition, this chapter will cover the utilization of optimisation tools to identify parameters for drift correction.

2.1. Principle of EMI

Figure 2.1 shows the principle of an EMI system arrangement. Such EMI systems that operate in the frequency domain generally have at least one transmitter coil (Tx) and one or more receiver coils (Rx). The Tx is powered by an sinusoidal current to create a periodic and time-varying (sinusoidal) primary electromagnetic field that diffuses into the ground (as shown in Figure 2.1) according to Faraday's law of induction,

$$\nabla \times E = -\mu \cdot \frac{\partial H_p}{\partial t}, \quad (2.1)$$

where H_p is the vector magnetic field strength (Am^{-1}) and t is time (s), E is the vector electric field strength (Vm^{-1}) and μ is the magnetic permeability (Hm^{-1}). This equation states that a time-varying magnetic field will produce an electric field whose curl is equal to the negative of the time derivative of the magnetic field. The electric field E will generate so-called eddy currents in the conductive subsurface that are proportional to the soil's electrical conductivity but are out of phase with the primary current from the Tx. These eddy currents create a secondary magnetic field (H_s). The Rx detects the superposition of the primary and secondary magnetic fields (H_p and H_s), which have an in-phase (real) and quadrature (imaginary) component, whereby the quadrature component is directly related to the electrical conductivity of the sensed soil subsurface.

The cumulative response of a certain volume of the underlying subsurface, commonly referred to as the homogeneous half-space, can be obtained as the average weighted electrical conductivity values (EC) over the sensed subsurface. This is converted into

apparent electrical conductivity (ECa) using the low induction number (LIN) approximation

$$\beta = \sqrt{\frac{\omega\mu_0 EC}{2}} x \ll 1 \quad (2.2)$$

proposed by McNeill [41], where ω is the angular frequency, μ_0 is the permeability of free space, and x is the intercoil spacing. This approximation is based on measurements performed on or above the soil surface, using small intercoil spacings between the Tx and Rx coils, low soil conductivities, and low frequencies.

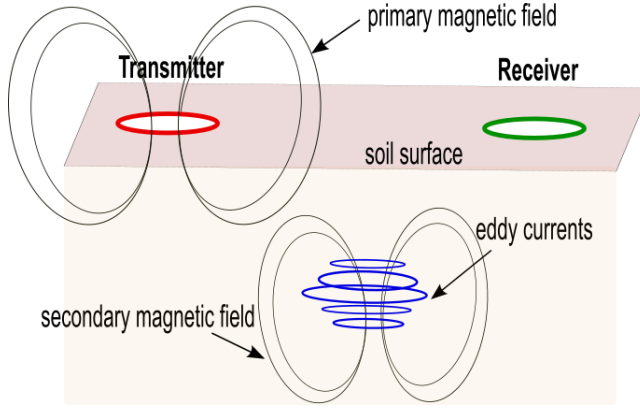


Figure 2.1.: Basic set-up of an electromagnetic induction (EMI) system.

The LIN approximation is valid when the soil is homogeneous and the eddy current penetration depth is small compared to the intercoil spacing [41]. Under the LIN approximation, the imaginary part of the ratio of the secondary to primary magnetic fields resulting from the homogeneous halfspace of electrical conductivity EC is [41]:

$$\text{Im}\left(\frac{H_s}{H_p}\right) \approx \frac{\omega\mu_0 EC x^2}{4}, \quad (2.3)$$

where the ratio of the magnitudes of H_s and H_p is the magnetic field response, x is the intercoil spacing, μ_0 is the permeability of free space and ω is the angular frequency.

Since the secondary magnetic field strength is out of phase by 90° from the primary magnetic field strength, the ratio of $Im(H_s/H_p)$, is significant here when it is relatively small. This corresponds to the phase difference Φ between the induced phase Φ_i of the magnetic field ($H_p + H_s$) at Rx and the phase Φ_p of the primary field H_p at Tx. In other words, the ratio can be approximated using the small phase angle approximation in Equation 2.3 as:

$$Im\left(\frac{H_s}{H_p}\right) = \tan(\Phi) \approx \Phi. \quad (2.4)$$

The equivalent response function obtained for a homogeneous half-space produces the apparent electrical conductivity (ECa) as per McNeill [41]:

$$ECa = \frac{4}{\omega\mu_0x^2} Im\left(\frac{H_s}{H_p}\right). \quad (2.5)$$

It should be noted that the factor $Im\left(\frac{H_s}{H_p}\right)$ can be very small and therefore difficult to measure and it's amplitude depends on various factors such as subsurface electrical conductivity, intercoil spacing and orientation, and operating frequency. For instance for a soil EC of 20 mSm^{-1} , intercoil spacing of 1 m, a measurement frequency of 10 kHz, the factor Φ is $390 \mu\text{rad}$ (Equation 2.4) and the induction number β is always less than 0.05.

This means that the method is only effective in relatively conductive environments (typically 10 mSm^{-1} - 100 mSm^{-1}) where the magnetic signals from the subsurface are not overshadowed by measurement errors. Thus, it is crucial to identify the conductivity of the target material and the surrounding environment before using this technique. In addition to conductivity, the distance x between the Tx and Rx has an effect on the measured $Im\left(\frac{H_s}{H_p}\right)$ factor. For smaller intercoil spacings x (e.g. less than 2 m), the $Im\left(\frac{H_s}{H_p}\right)$ factor decreases with the square of x , making it more difficult and uncertain to measure (see Equations 2.4 and 2.5).

2.2. Sensitivity of Common Coil Configurations

EMI measurements can be obtained using different coil configurations, which can result in variations in the induced eddy currents and the associated secondary magnetic field. These variations have different soil depth sensitivities. The three most popular coil configurations used for EMI measurements which can be applied to the EMI device in this work are the vertical coplanar (VCP), horizontal coplanar (HCP) and

perpendicular (PRP) configurations.

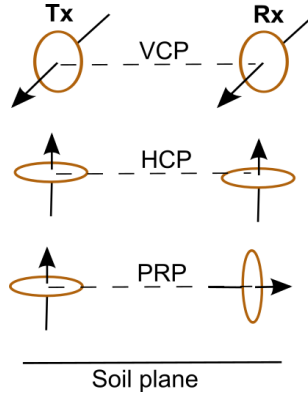


Figure 2.2.: Vertical coplanar coil (VCP), horizontal coplanar coil (HCP) and perpendicular coil (PRP) configurations.

The diagram in Figure 2.2 depicts the representation of transmitter (Tx) and receiver (Rx) coils in the vertical coplanar coil, horizontal coplanar coil and perpendicular coil configurations. The VCP configuration consists of a vertically oriented coil placed over a coplanar ground plane (the coils are orthogonal to the soil surface and the magnetic dipole arrow is parallel to the soil [83, 84]), while the HCP configuration consists of a horizontally oriented coil placed over a coplanar ground plane (the coils are oriented parallel to the soil with the magnetic dipole arrow in a vertical direction). The coils in PRP configuration have dipoles (arrows) both perpendicular and horizontal to the plane of the soil.

The diagrammatic representation in Figure 2.3a shows a plot of local-sensitivity curves as described by McNeill [41] for three coil orientations: HCP, VCP and PRP. Figure 2.3b shows the corresponding cumulative response curve. The depth (h) indicated in the curve is normalized based on the intercoil spacing (x) between the transmitter and receiver.

These sensitivity curves show the relative response to the secondary magnetic field sensed at the receiver from a soil beneath a certain depth (normalised). The curves indicate that the VCP and PRP configurations are better suited to sensing the shallow part of the subsurface, while the HCP configuration is more effective in sensing the deeper part of the subsurface. This is because the HCP configuration has twice the exploration depth of the VCP configuration. This can be seen on the curves as the relative response to the secondary magnetic field of the VCP and PRP configuration is highest at the surface (i.e. smaller normalised depths between 0 and 0.3) and decreases monotonically as the normalised depth increases (0.5 - 2), whereas the

sensitivity of the HCP configuration peaks at a depth of 0.4 times the intercoil separation [41, 46]. Integrating the local sensitivities results in the cumulative response curves shown in Figure 2.3. It can be seen here that the soil below 0.5 intercoil spacings (normalised depth h/x) contributes 0.3 (30 %), 0.6 (60 %) and 0.7 (70 %) to the secondary magnetic field sensed at the receiver for the HCP, VCP and PRP modes respectively.

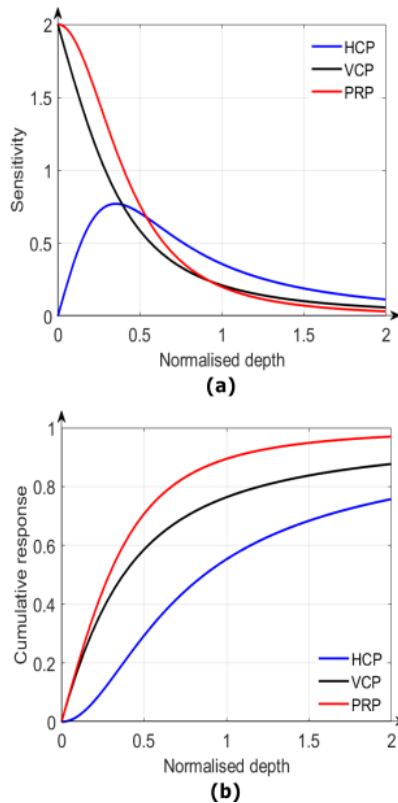


Figure 2.3.: (a) Plot of local-sensitivity curves. (b) Equivalent cumulative response curves vs. normalised depth h/x .

2.3. Local-Sensitivity Model

The local-sensitivity model (LS model) or cumulative response model is the most commonly used forward model in EMI surveys. This model was introduced by McNeill [41]. The LS model is a simple and efficient model that assumes that the subsurface is made up of layers of homogeneous material, having their respective electrical conductivities $EC(h)$, with h being the depth of the soil layer. Figure 2.4 shows an example

for the calibration of an EMI instrument with intercoil spacing x , over a three-layered soil with electrical conductivities EC_1 , EC_2 and EC_3 , with corresponding depths h_1 , h_2 and h_3 respectively.

The LS model calculates the response of the instrument to each layer and then sums up the responses to obtain the total response. This is done using cumulative response functions

$$CRF^{VCP}(h, x) = \sqrt{4\left(\frac{h}{x}\right)^2 + 1} - 2\left(\frac{h}{x}\right) \quad (2.6)$$

$$CRF^{HCP}(h, x) = \frac{1}{\sqrt{4\left(\frac{h}{x}\right)^2 + 1}} \quad (2.7)$$

proposed by McNeill [41], which provide a mathematical framework to determine the contribution for a Tx – Rx separation of x , of each depth h below the sensor and for the VCP and HCP orientations. These functions take into account the geometry of the target, the coil, and the receiver, and provide a way to accurately interpret the measurements obtained from the Rx. The overall ECa is given by

$$ECa = EC_1 \cdot [1 - CRF(\frac{h_1}{x})] + EC_2 \cdot [CRF(\frac{h_1}{x}) - CRF(\frac{h_2}{x})] + EC_3 \cdot [CRF(\frac{h_2}{x})] \quad (2.8)$$

for the three-layered model in Figure 2.4, where h_1 is the thickness of the first layer with electrical conductivity EC_1 , $h_2 - h_1$ is the thickness of the second layer with conductivity EC_2 and EC_3 is the conductivity of the third layer. Equation 2.8 gives a simple method to calculate the an EMI instrument reading on an arbitrary layered earth by summing the contribution from each layer.

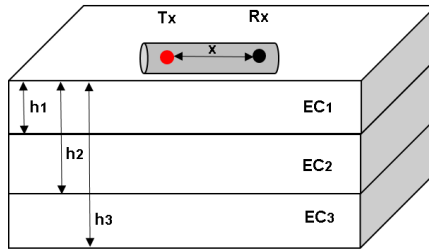


Figure 2.4.: Representation of a three-layered soil model for EMI instrument calibration.

In addition to the depth h and conductivity EC (Equations 2.6 and 2.7), the orientation of the measurement coils relative to the soil surface is a factor in the relative cumulative response of the electrical conductivity of the soil from various depths [60]. It is important to note that the local sensitivity curves referred to in this context are only applicable when the instrument is placed on the soil's surface at zero elevation. Otherwise an additional air layer with $EC = 0$ has to be inserted above.

The LS model is widely used because of its simplicity in determining soil depth sensitivity and its accuracy in reconstructing the conductivity of the soil and in predicting the response of the instrument to the subsurface layers. The model does this by inverting the measured ECa values into depth-dependent electrical conductivities. The most common approach to achieving this is by using an optimisation method that minimizes the cost function

$$\Delta ECa(h) = \frac{1}{N} \sqrt{\sum_{i=1}^N \frac{(ECa_{ms} - ECa_{mod})^2}{(ECa_{ms})^2}} \quad (2.9)$$

of both the measured ECa data (ECa_{ms}) and the modelled data (ECa_{mod}). This LS model can now be used to estimate the parameters h_1 , h_2 , EC_1 , EC_2 and EC_3 , using an optimisation method where the cost function in Equation 2.9 is minimized. By reconstructing the soil conductivity in this way, researchers and practitioners can obtain accurate and reliable information about the properties of soil at different depths, which is important for a range of applications.

In order to determine the depth sensitivity using the above equations, it is necessary to measure with different coil orientations, device elevations and/or Tx – Rx distances. The more measurements with different parameters (x , h , VCP, HCP as in Equations 2.6 and 2.7), the better the depth resolution in theory, assuming that the measurements are error-free. For example as demonstrated by McNeill [41], in the case of the HCP configuration, approximately 68% of the soil response is influenced

by the electrical conductivity of the uppermost $1.50 \cdot x$ meters of the soil. For the VCP configuration, the soil response is dependent on the electrical conductivity of the uppermost $0.75 \cdot x$ meters, while for the PRP configuration, the soil response is influenced by the electrical conductivity of the uppermost $0.50 \cdot x$ meters of the soil. Hence, changing the coil orientation of the EMI device makes it possible to evaluate soil ECa with depth.

2.4. ECa Calculation

The relationship shown in Equation 2.4 leads to a simplification of Equation 2.5 as:

$$ECa = \frac{4}{\omega \mu_0 x^2} \Phi. \quad (2.10)$$

where x is the intercoil spacing, μ_0 is the permeability of free space, ω is the angular frequency and Φ is the approximated small phase angle. To estimate the necessary phase measurement accuracy for the LIN approximation, Equation 2.10 is used. This equation provides an estimate of the phase shift induced by the soil as a function of the intercoil spacing and the soil electrical conductivity.

The approximated phase (Φ) increases monotonically as the square of the separation between the Tx and Rx coils. For instance, in the system illustrated in Figure 4.2, an intercoil spacing of 1.2 m and an ECa of 1 mSm^{-1} results in very small phase values of approximately $28 \mu\text{rad}$. Achieving such accuracy requires a very precise measurement which need to include additional drift correction as this is necessary to compensate for any changes in the EMI instrument's response over time, such as temperature variations or instrument drift. Hence by applying drift correction, the accuracy of the phase measurement can be significantly improved.

3. Theory on Modelling and Optimization of EMI Data

3.1. The Nelder-Mead Algorithm

The simplex algorithm by Nelder and Mead [85] (Nelder-Mead approach) is frequently employed to solve the unconstrained optimisation problem $\min f(p)$ where $f(p)$ is called the cost function and p are the parameters of dimension n . It is an optimisation approach that does not require knowledge of the function's derivative or other properties, making it suitable for functions with complicated or unknown properties. The algorithm works by iteratively transforming a set of points (called the simplex) in the n -dimensional space to search for the minimum value of the cost function. At each iteration, the simplex is transformed using one of the four operations (Figure 3.1): reflection, expansion, contraction, or shrinkage, depending on the value of the objective function at the simplex vertices.

The algorithm uses a simplex which is a geometric shape that constitutes the convex envelope of $n + 1$ vertices. The simplex with vertices x_1, x_2, \dots, x_{n+1} is represented by the symbol Δ . The Nelder-Mead approach produces a series of simplices in an iterative manner to estimate an optimal point for the function f . In every iteration, the vertices $x_{j=1}^{n+1}$ of the simplex are arranged based on their objective function values as

$$f(x_1) \leq f(x_2) \leq \dots \leq f(x_{n+1}). \tag{3.1}$$

The representation in Figure 3.1 is that of Nelder-Mead simplices after a reflection, an expansion, an outside contraction, an inside contraction, and a shrink step. The original simplex is shown with a dashed line (x_1 - x_2 - x_3). The vertex with the best objective function value is referred to as x_1 , while the vertex with the worst objective function value is referred to as x_{n+1} . If multiple vertices have identical objective values, the Nelder-Mead approach necessitates consistent tie-breaking regulations, such as those described in Lagarias et al. [86], to ensure the method's proper definition. If the centroid of the n best vertices is denoted by \bar{x} [87], then

$$\bar{x} = \frac{1}{n} \sum_{i=1}^n x_i. \quad (3.2)$$

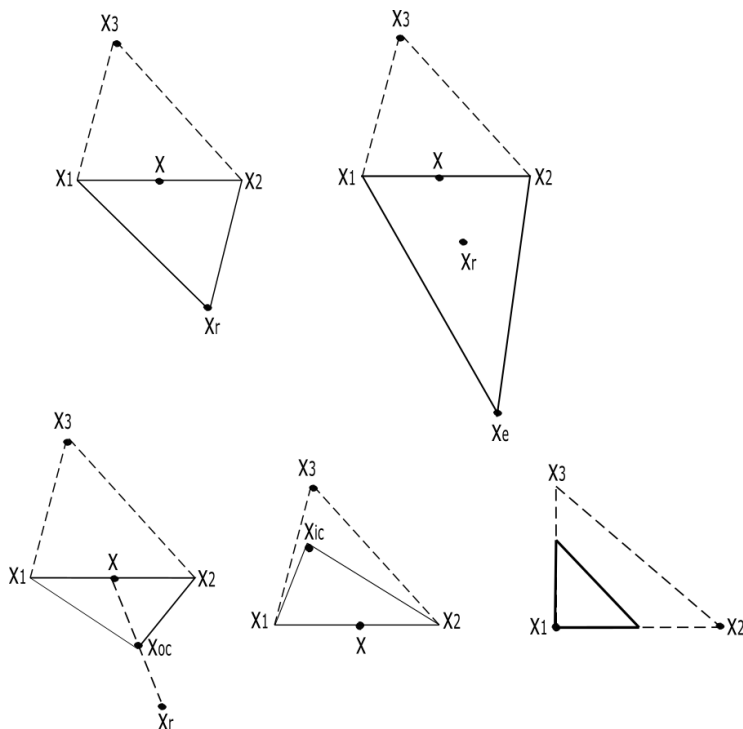


Figure 3.1.: Nelder–Mead approach with original simplex shown with a dashed line $(x_1-x_2-x_3)$ (adaptation from Lagarias et al. [86]).

The algorithm can be described using the following iterative steps (also described by Gao and Han [87], Lagarias et al. [86]):

1. Sorting - Compute the function values of f for the $n + 1$ vertices of the simplex Δ and sort the vertices so that Equation 3.1 is satisfied.
2. Reflection - Determine the reflection point x_r using the following calculation:

$$x_r = \bar{x} + \rho(\bar{x} - x_{n+1}). \quad (3.3)$$

ρ is the reflection coefficient. If $f(x_1) \leq f(x_r) \leq f(x_n)$, accept the reflection point by replacing x_{n+1} with x_r and terminate the iteration.

3. Expansion - If $f(x_r) \leq f(x_1)$, estimate the expansion point x_e

$$x_e = \bar{x} + \chi(x_r - \bar{x}) \quad (3.4)$$

and evaluate $f(x_e)$, with χ being the expansion coefficient. If $f(x_e) \leq f(x_r)$, accept the expansion point by replacing x_{n+1} with x_e and terminate the iteration. Otherwise replace x_{n+1} with x_r and terminate the iteration.

4. Outside contraction - If $f(x_n) \leq f(x_r) \leq f(x_{n+1})$, evaluate the outside contraction point

$$x_{oc} = \bar{x} + \gamma(x_r - \bar{x}) \quad (3.5)$$

and estimate $f(x_{oc})$. γ is the contraction coefficient. If $f(x_{oc}) \leq f(x_r)$, accept the expansion point by replacing x_{n+1} with x_{oc} and terminate the iteration. Otherwise go to step 6.

5. Inside contraction - If $f(x_r) \geq f(x_{n+1})$, determine the inside contraction point

$$x_{ic} = \bar{x} - \gamma(\bar{x} - x_{n+1}) \quad (3.6)$$

and evaluate $f(x_{ic})$. If $f(x_{ic}) \leq f(x_{n+1})$, accept the expansion point by replacing x_{n+1} with x_{ic} and terminate the iteration. Otherwise go to step 6.

6. Shrinkage - Estimate f at the n points $x'_i = x_1 + \sigma \cdot (x_i - x_1)$, $i = 2, \dots, n + 1$. σ is the shrinkage coefficient. The unsorted vertices of the simplex at the next iteration are $x_1, x'_1, \dots, x'_{n+1}$.

The four parameters of the Nelder-Mead approach determine the size and direction of the simplex transformation at each iteration. The coefficient of reflection (ρ) controls the magnitude of the reflection operation, which involves reflecting the worst vertex of the simplex across the centroid of the remaining vertices. The expansion coefficient (χ) determines the size of the expansion operation, which involves moving the reflected vertex even further away from the centroid. The contraction coefficient (γ) determines the size of the contraction operation, which involves moving the

worst vertex towards the centroid. Finally, the shrinkage coefficient (σ) controls the magnitude of the shrinkage operation, which involves reducing the size of the simplex.

To ensure the convergence and stability of the algorithm, the four coefficients must satisfy certain conditions. In particular, the reflection coefficient must be greater than zero, but less than or equal to one, and the shrinkage coefficient must be less than one. The expansion and contraction coefficients have more flexible conditions, but they should be carefully chosen to balance the exploration and exploitation of the search space. Although the original publication does not explicitly state the relationship between the parameters χ and ρ , the connection can be inferred from the algorithm's terminology and explanation. In practice, the standard Nelder-Mead approach typically uses the following values for these parameters [86]:

$$\rho = 1, \quad \chi = 2, \quad \gamma = \frac{1}{2} \quad \text{and} \quad \sigma = \frac{1}{2} \quad (3.7)$$

Despite the absence of a satisfactory theory of convergence, the Nelder-Mead approach is known to effectively solve small-dimensional problems and has consistently remained as one of the most commonly used direct search methods [87]. It has however been noted that the Nelder-Mead approach can become highly inefficient when used to solve problems with a large number of dimensions [86]. This leads to the adaptation of the Nelder-Mead approach by some researchers to minimise more complex problems. Other researchers simply turn towards more global optimisation methods.

3.2. Shuffled Complex Evolution (SCE) Algorithm

Shuffled complex evolution (SCE) is a global optimisation technique (in contrast to the Nelder-Mead simplex algorithm) that integrates deterministic approaches to direct the search with the addition of random elements, which enhance the algorithm's flexibility and resilience [88]. The SCE algorithm has demonstrated its efficacy in the inversion of EMI data according to von Hebel et al. [89]. In addition, it has been utilised in the inversion of ground penetrating radar data for various purposes, including the resolution of water content profiles [90], estimation of subsurface object radius [91], and acquisition of hydrologic parameters [92].

In the SCE algorithm, a population is dispersed throughout the feasible parameter space and subdivided into complexes. Each complex provides valuable information on the number, location, and size of the primary areas of attraction. Additionally, an implicit clustering strategy concentrates the search in the most promising regions, enhancing the SCE algorithm's efficiency and effectiveness [88]. This process ensures that the algorithm searches the parameter space thoroughly and efficiently, allowing for a more comprehensive exploration of the parameter space.

Figure 3.2 illustrates the various steps involved in the SCE algorithm. The first step involves randomly sampling S points from the parameter space Ω to generate a set of potential solutions. The number of points sampled is determined by the number of complexes (c) and the number of parameter sets per complex (p). For instance, if there are n layers, the number of complexes is determined by

$$c = 2 \times n - 1 \tag{3.8}$$

and the number of parameter sets per complex should be

$$p = 2 \times c + 1. \tag{3.9}$$

To find the best possible solution, the algorithm repeats a series of operations on the generated points, which include sorting them based on their fitness, selecting the best individuals for reproduction, and performing genetic operations to create new individuals. The process is then repeated until convergence to the best global minimum is achieved. Extensive tests have shown that when the number of complexes is equal to the dimensionality of the problem, as is the case with n -layers, the fitting time is shorter and convergence to the best global minimum is achieved faster. This demonstrates that the SCE algorithm is a reliable method for exploring the parameter space and identifying optimal solutions in a variety of applications.

The algorithm operates by first calculating the objective function for each set of parameters and arranging these sets in ascending order of misfit $\Delta Error$ in a matrix called M . This matrix is then divided into several complexes, A^k , where k ranges from 1 to c . Each complex is treated independently using a systematic approach based on the competitive complex evolution (CCE) algorithm. The CCE algorithm employs a triangular probability distribution to ensure that the different populations of parameters within each complex compete against each other during the search process [93]. This means that the CCE algorithm explores the parameter space in various directions, continually sampling new parameter combinations and evolving the population. In this way, the algorithm is able to efficiently search the parameter space and converge towards optimal parameter values that minimise the misfit between the observed data and the model predictions.

After the initial partitioning of the parameter sets into complexes, the program proceeds to shuffle and reassign them to the matrix M . This new matrix is then once again sorted based on the increasing misfit of each parameter set, after which the complexes are partitioned again. This shuffling and partitioning process is repeated until one of two general convergence criteria is met. The first criterion is met when the number of function evaluations reaches the maximum limit of 1000 times n -squared,

where n is the number of parameters being optimised. The second criterion is met when the improvement in the misfit between the observed data and model predictions becomes smaller than a set percentage within a pre-specified number of rounds of the CCE loop. The use of competitive complex evolution and shuffling in the SCE algorithm allows for the exploration of a wide range of parameter combinations and enhances survivability by promoting the survival of better parameter sets over worse ones. This results in improved global convergence efficiency, as described in previous studies by Duan and Gupta [93].

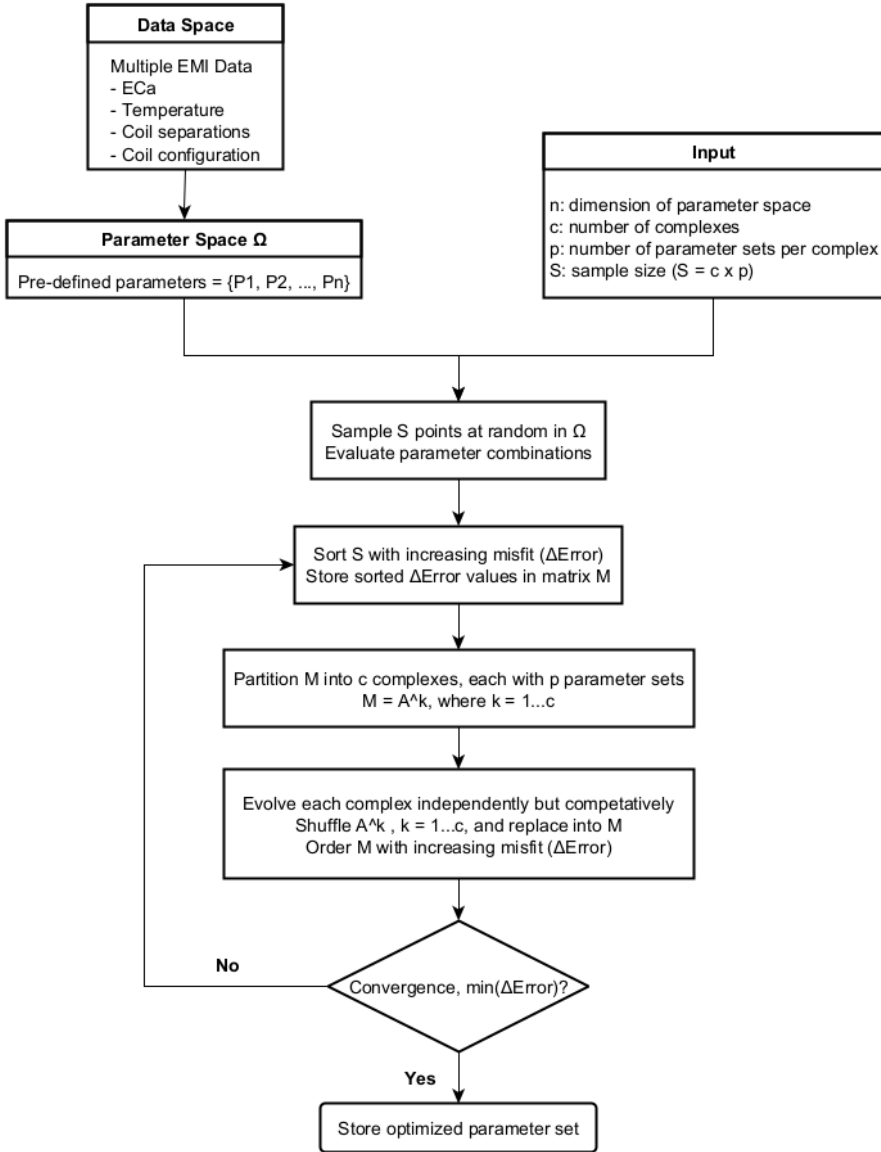


Figure 3.2.: A diagram outlining the steps of the SCE inversion algorithm used to process EMI data.

3.3. Infinite Impulse Response Filter

The objective of the study was to investigate the impact of abrupt variations in external ambient temperatures on the internal temperatures of the EMI measurement system and its components. In order to accomplish this, a digital low-pass filter (LPF) was utilised in the time domain to filter input and output signals which in this case are both temperature signals. The low pass filter of interest for drift analysis in this work is an infinite impulse response (IIR) filter with a general input and output relationship where the discrete time index n can be expressed as a difference equation (e.g. [94], [95], [96]):

$$y(n) = \sum_{i=0}^M b_i x(n-i) - \sum_{i=1}^N a_i y(n-i), \quad (3.10)$$

where a_i and b_i are the filter coefficients. These coefficients determine the behavior of the system. The present and past M input signals are represented by $x(n)$. These input signals are what drive the system and cause it to produce the output signals. The past N output signals are represented by $y(n)$ and are the result of the system's previous response to the input signals. By using the Z-transform to represent the input-output relationship of a dynamic system such as given by Equation 3.11, the system's behavior in the frequency domain can be analysed. This can provide valuable insight into the system's stability, response to different input signals, and other important characteristics. Here the Z-transform is:

$$G(z) = \frac{Y(z)}{X(z)} = \frac{\sum_{i=0}^M b_i \cdot z^{-i}}{\sum_{i=0}^N a_i \cdot z^{-i}} = \frac{b_0 + b_1 \cdot z^{-1} + \dots + b_M \cdot z^{-M}}{a_0 + a_1 \cdot z^{-1} + \dots + a_N \cdot z^{-N}} \quad (3.11)$$

where z is the complex Z-transformed variable. In this case, the transfer function of the filter can be represented by Equation 3.12, whereby, to actually design the filter, it is customary to use an analog equivalent simple first-order LPF ($M = 1$ and $N = 1$) with a transfer function H_a . This transfer function can be expressed as a function of the frequency variable s . The transfer function H_a of the analog LPF is given by:

$$H_a(s) = \frac{\omega_c}{s + \omega_c} \quad \text{and} \quad \omega_c = \frac{1}{\tau} \quad (3.12)$$

where ω_c is the cut-off frequency of the LPF, the subscript a stands for analog, s

is the Laplace operator, and τ is the time constant of the LPF. The frequency variable s can be related to z by the bilinear transformation [95]. This technique is used to convert a continuous-time analog filter into a discrete-time digital filter while maintaining the frequency characteristics of the filter. Therefore by using this transformation, we can design a stable digital filter that mimics the response of an analog filter. This is done by replacing the Laplace operator s by the term

$$s = \frac{2}{T_s} \frac{z - 1}{z + 1} \quad (3.13)$$

where T_s is the sampling period (as per the Nyquist theorem). The first order Z-transform of the transfer function $G(z)$ for the digital IIR filter is given as

$$H_d(z) = \frac{b_0 + b_1 \cdot z^{-1}}{1 + a_1 \cdot z^{-1}} \quad (3.14)$$

where the subscript d is used to denote that it pertains to digital values. By plugging in the value of s from Equation 3.13 into Equation 3.12 and then comparing the resulting equation with Equation 3.14, it becomes possible to calculate the filter coefficients for the first-order digital filter as:

$$a_1 = \frac{1 - \frac{T_s}{2\tau}}{1 + \frac{T_s}{2\tau}} \quad \text{and} \quad (3.15)$$

$$b_0 = b_1 = \frac{\frac{T_s}{2\tau}}{1 + \frac{T_s}{2\tau}}. \quad (3.16)$$

where the values of the filter coefficients a_1 , b_0 , and b_1 are obtained by taking into account the cut-off frequency ω_c and the sampling period T_s .

The representation in Figure 3.3 shows a signal flow diagram of the first order IIR filter implemented in MATLAB and used to model the present and past system temperature delay dynamics of the measurement instrument. The inputs are the present and past values of the effective value of the measured temperature ($T_{eff}(n)$ and $T_{eff}(n - 1)$) respectively. The outputs are the present and past values of the modelled temperature ($T_{mod}(n)$ and $T_{mod}(n - 1)$) respectively. a_1 , b_0 , and b_1 are the filter coefficients.

Using the filter coefficients, it was possible to derive a filter function from Equation 3.10 (also shown in Figure 3.3), where z^{-1} represents a unit delay block, which implies that the output of the delay block is equal to the input signal delayed by one time step. On the input side of the IIR LPF, the product of the effective temperature's current value $T_{eff}(n)$ and the filter coefficient b_0 are added to the product of the past value of the effective temperature $T_{eff}(n-1)$ and the filter coefficient b_1 . This is then added to the output values consisting of the product of the past modelled temperature value $T_{mod}(n-1)$, which ultimately gives the overall modelled temperature $T_{mod}(n)$. Hence, the modelled temperature T_{mod} at the discrete time index n using the effective input temperature T_{eff} can now be defined as:

$$T_{mod}(n) = b_0 \cdot T_{eff}(n) + b_1 \cdot T_{eff}(n-1) + a_1 \cdot T_{mod}(n-1). \quad (3.17)$$

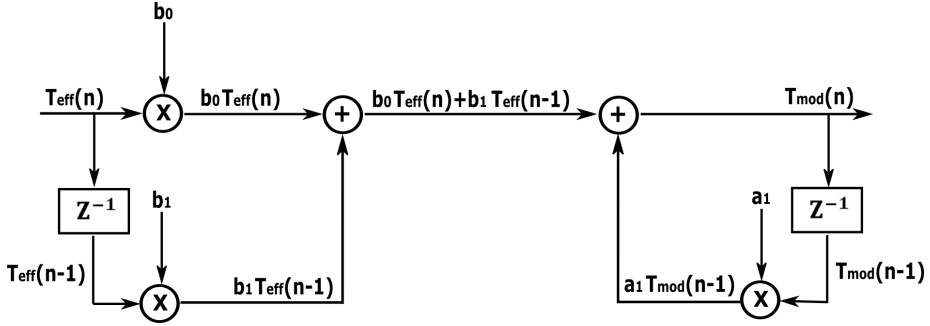


Figure 3.3.: Signal flow diagram of the first order IIR filter used to model the present and past temperature delay dynamics of the measurement instrument.

3.4. Phase Value Calculation and Correction

The process of converting a measured temperature into a phase value can be challenging, particularly when non-linear relationships exist between temperature and phase. To address this challenge, a cubic spline interpolation method was used, which involves utilizing three reference temperature points and their corresponding reference phases to determine the modeled phase value for a given modeled temperature T_{mod} . The reference temperature points used in this approach are selected based on the temperature range observed during EMI measurements.

Here, the reference temperature points are $T_{ref_{min}} = 0.0^\circ\text{C}$, $T_{ref_{mid}} = 25.0^\circ\text{C}$, and $T_{ref_{max}} = 50.0^\circ\text{C}$. For each of the reference temperature points, there is a corresponding reference phase value. These values, denoted as $\phi_{ref_{min}}$, $\Phi_{ref_{mid}}$, and $\Phi_{ref_{max}}$, respectively, are determined through theoretical means. The cubic spline interpolation method involves fitting a cubic polynomial to the reference temperature and

phase data points. Then the resulting polynomial can be used to estimate the phase value for any modeled temperature within the temperature range. The goal is to establish a clear relationship between temperature and phase at each reference temperature point. The accuracy of the method depends on the number and spacing of the reference temperature points, as well as the quality of the reference phase values.

In practice, the modeled temperature T_{mod} is first determined through a temperature measurement and a simulation. The T_{mod} is then used as an input to the cubic spline interpolation method, which returns the corresponding modeled phase value. This modeled phase value can then be used to correct the measured phase value, accounting for any non-linearity in the temperature-phase relationship. The three phase points are determined based on Φ_{off} , G , and NL . The first calibration point, which represents the phase offset, is calculated as the phase at 0.0°C :

$$\phi_{ref_{min}} = \Phi_{off} \quad (3.18)$$

The third point of calibration is determined based on the gain value, taking into account the phase offset:

$$\phi_{ref_{max}} = \Phi_{off} + G(T_{ref_{max}} - T_{ref_{min}}) \quad (3.19)$$

The middle calibration point is determined from the non-linear term NL :

$$\phi_{ref_{mid}} = \Phi_{off} + NLG(T_{ref_{mid}} - T_{ref_{min}}) \quad (3.20)$$

The plot depicted in Figure 3.4 shows cubic spline interpolation using three reference calibration points across a chosen temperature range spanning from $T_{ref_{min}} = 0^{\circ}\text{C}$ to $T_{ref_{max}} = 50.0^{\circ}\text{C}$. The illustration showcases three distinct scenarios, each represented by a different colored line. If NL equals 1, it signifies that the behavior is entirely linear, where the output changes proportionally to changes in the input, as denoted by the black line. However, when a NL value other than 1 is chosen, it will produce a non-linear correlation between temperature and phase after spline interpolation, which will shift the curve upwards or downwards, depending on the specific values of the NL parameter.

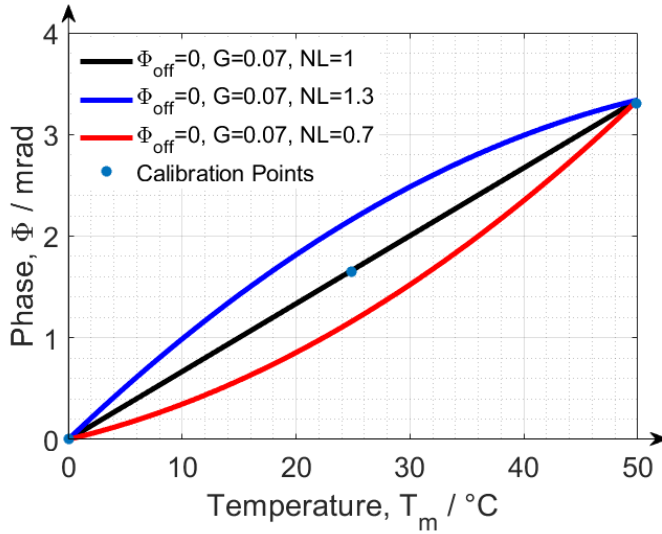


Figure 3.4.: The provided plot shows cubic spline interpolation using three reference points within a chosen temperature range.

3.5. Principal Component Analysis

Temperature sensors play a critical role in gathering information on the temperature distribution within a measurement device while acquiring EMI data. This is because temperature changes can have a significant impact on the measurement instrument, which can lead to errors or inconsistencies in the collected data. Therefore, monitoring and analyzing the local internal temperature is critical to ensure the accuracy and reliability of the measurement results. After obtaining the sensor data, it is possible to analyse the local internal temperature of the measurement instrument. This analysis can help in simplifying the correction of drift effects on the measured ECA.

To make the correction of drift effects easier, it is initially assumed that the variation in external ambient temperature within the device is uniform across all components. This assumption is especially helpful when there is high covariance between temperature sensors. By relying on just a few temperature components, most drifts caused by temperature changes can be corrected. This approach is preferred over using multiple redundant components that carry the same information, as it minimizes the resources required for correction while maintaining accuracy.

The method of principal component analysis (PCA) is an effective way to address the issue of multicollinearity in measured data [97, 98]. The PCA method can be used to identify the underlying relationships among the temperature sensor readings

and determine which factors contribute most to the observed variance. By doing so, it is possible to reduce the dimensionality of the data while retaining the most relevant information. The method essentially transforms the data into a new coordinate system where the new axes, or principal components, represent linear combinations of the original temperature measurements.

The principal components are then ranked according to their respective contribution to the variance observed in the data. The first few principal components with the highest contribution are retained for further analysis, while the remaining components can be disregarded as they contain little information. By focusing only on the most significant principal components, the effects of multicollinearity can be mitigated, allowing for more accurate and reliable analysis of the data.

Mathematically, the PCA method, as explained by Jolliffe [99], involves the determination of the covariance matrix

$$C = T_{ms}^T \cdot T_{ms} \quad (3.21)$$

of the normalised (by \sqrt{n}) and mean-centered measured temperature time series T_{ms} , where n is the number of temperature time series [99]. An eigen decomposition of this covariance matrix

$$[E_{vec}, E_{val}] = eigen(C) \quad (3.22)$$

transforms the temperature data into eigenvalues E_{val} with their corresponding linear independent (orthogonal) eigenvectors E_{vec} [100]. The eigenvalues are an indication of the magnitude of the respective eigenvectors and a measure of their importance in explaining variation within the dataset [99]. The principle components

$$PC = T_{ms} \cdot E_{vec} \quad (3.23)$$

are estimated as a product of the original temperature data and the eigenvectors. The mean subtracted from the temperature data at the start of the PCA analysis is again added to the principal components. The generated principal components

$$PC = PC + mean(T_{ms}) \quad (3.24)$$

are uncorrelated with each other but correlated with the measured data.

4. Uniform Temperature Drift Correction

Chapter 2 of this thesis report introduces an important issue related to EMI measurements, whereby it is stated that variations in external ambient temperature causes drifts on the EMI measured data. In order to address this problem, a novel correction method is proposed in the current chapter. The method involves using a low-pass filter (LPF) to model the dynamic characteristics of the drifts and then using this model for correction purposes. The correction method is developed and tested using a customised EMI device with an intercoil spacing of 1.2 meters.

The device is optimised for low drift and equipped with 10 temperature sensors that measure the local internal temperature simultaneously across the device. Outdoor calibration measurements are conducted over several days, covering a wide range of temperatures. At the start of the chapter, the internal electronic components of the EMI circuit are analysed in a signal flow diagram. The argument is made that each component of the measurement system can be a source of drifts.

Following this, the methodology of the dynamic drift correction model is introduced. This model takes into account the transient delays of the system components in response to external ambient temperature changes. The next step involves the presentation of the temperature correction method, which includes the LPF and a look-up table (LuT). The LuT converts temperature information into phase. Overall, the proposed correction method is expected to provide more accurate and reliable EMI measurements by mitigating the impact of external ambient temperature on the output data.

4.1. Materials and Method

4.1.1. EMI Measurement System with Temperature Sensors

The EMI measurement set-up utilised in this study is a modified version of the set-up originally developed by Mester et al. [65] and described in detail by Tan [82]. The system is composed of several components, including a transmitting (Tx) coil and three receiving (Rx) coils, as well as a generator unit (Gen) to power the Tx coil, a microcontroller (μC) to measure temperatures and for hardware configuration, an integrated computer (IC) and an analog-to-digital converter (ADC) (Figure 4.1).

4. Uniform Temperature Drift Correction

These components work together to accurately measure EMI data at a frequency of 10 kHz. Intercoil spacings for this system are 0.4 m, 0.8 m, and 1.2 m, with a focus on the intercoil spacing of 1.2 m for this particular study.



(a)

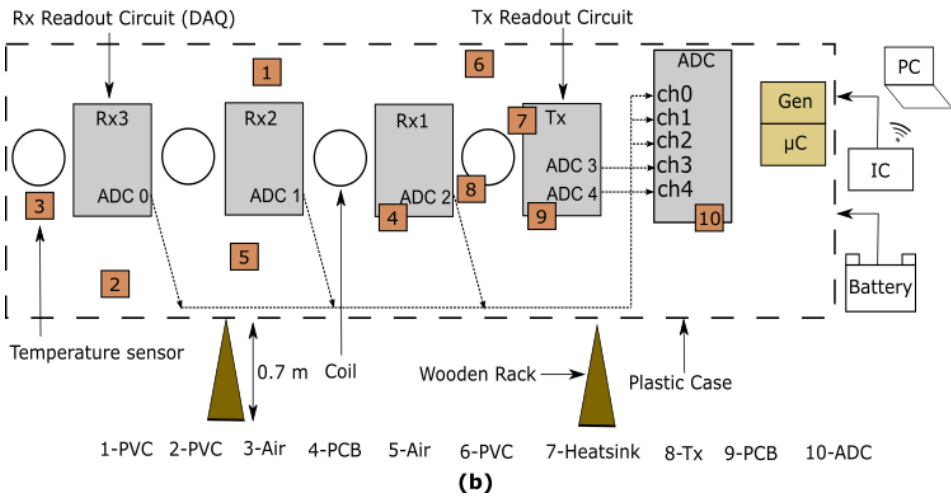


Figure 4.1.: (a) Picture of the EMI instrument used to perform measurements. (b) simplified schematic diagram of the EMI measurement system.

The diagrammatic representation in Figure 4.1a depicts a photograph of the instrument used for EMI measurements and in Figure 4.1b it shows a simplified diagram of the EMI measurement set-up. The set-up consists of a polyvinyl chloride (PVC) pipe that holds the transmitter (Tx) coil and three receiver (Rx) coils along with their respective readout circuits. The data acquisition unit (DAQ) includes the analog-to-digital converter (ADC), a generator unit (Gen), a microcontroller (μC), and an integrated computer (IC). The system is powered by an external battery and can be controlled remotely via WLAN and a personal computer (PC). The set-up includes 10 temperature sensors: sensor 9 measures the temperature of the printed circuit board (PCB), sensors 3, 4, and 5 monitor the air temperature inside the PVC tube, sensors 1, 2, and 6 measure the PVC temperature, sensor 8 measures the temperature at the

Tx coil, sensor 7 measures the temperature of the heat sink, and sensor 10 measures the temperature of the ADC casing.

To power the measurement instrument, an external 12 V DC power source (battery) is used. The ADC used in the system is a 24-bit sigma-delta ADC (National Instruments USB-4432), which provides a rated input voltage range of ± 10 V and a high resolution of $0.1 \mu\text{V}/\sqrt{Hz}$. This ensures that precise and accurate measurements of the electromagnetic signals are detected by the Rx coils. Each Rx coil is equipped with a readout circuit that amplifies and transfers the measured signal to the ADC for processing. The measurement system is controlled by a customised MATLAB software, which is running on the IC. The software allows to remotely regulate the measurement program via WLAN from an external notebook (PC). This provides the flexibility to make adjustments to the measurement program as needed, without the need of direct physical access to the measurement instrument.

The temperature sensors used for this task were digital thermometers, specifically the Dallas Semiconductor DS18S20 model [101]. These thermometers are capable of measuring temperatures within a range of -55°C to 125°C with an accuracy of $\pm 0.5^\circ\text{C}$ and a 9-bit resolution, making it possible to obtain accurate and comprehensive temperature data throughout the EMI device. Details on the custom EMI measurement system are shown on the signal flow diagram in Figure 4.2a, which comprises a single Tx – Rx arrangement and operates based on a series of processes described subsequently.

The generator, denoted as Gen, supplies a sinusoidally varying voltage U_G at a specific frequency to the Tx coil. This voltage input results in a sinusoidal primary current, I_p , flowing through the Tx coil, producing a primary magnetic field, H_p . The current flowing through the Tx coil is determined through a current measurement circuit, I_{ms} , which measures the voltage drop, U_p , over a resistor that is connected serially to the Tx coil. Ideally, the phase of H_p and U_p is identical (shown in Figure 4.2b) and is denoted with Φ_p subsequently.

Once the primary magnetic field, H_p , is produced, it diffuses into the soil and induces eddy currents in the conductive subsurface. These eddy currents generate a secondary magnetic field, H_s , that is shifted in phase by 90° with respect to H_p at the position of the Rx coil as stated by the Maxwell equations [102] (section A). Figure 4.2b shows the relationship between the primary, secondary and measured magnetic fields in a magnitude and phasor diagram. The superposition of the primary and secondary magnetic fields

$$H_{ms} = H_p + H_s \quad (4.1)$$

which is observed at the Rx coil induces a voltage, U_i , with a corresponding phase, Φ_i .

The induced voltage signal U_i , together with U_p , is then fed to the data acquisition (DAQ) unit after passing through an amplification circuit (AMP).

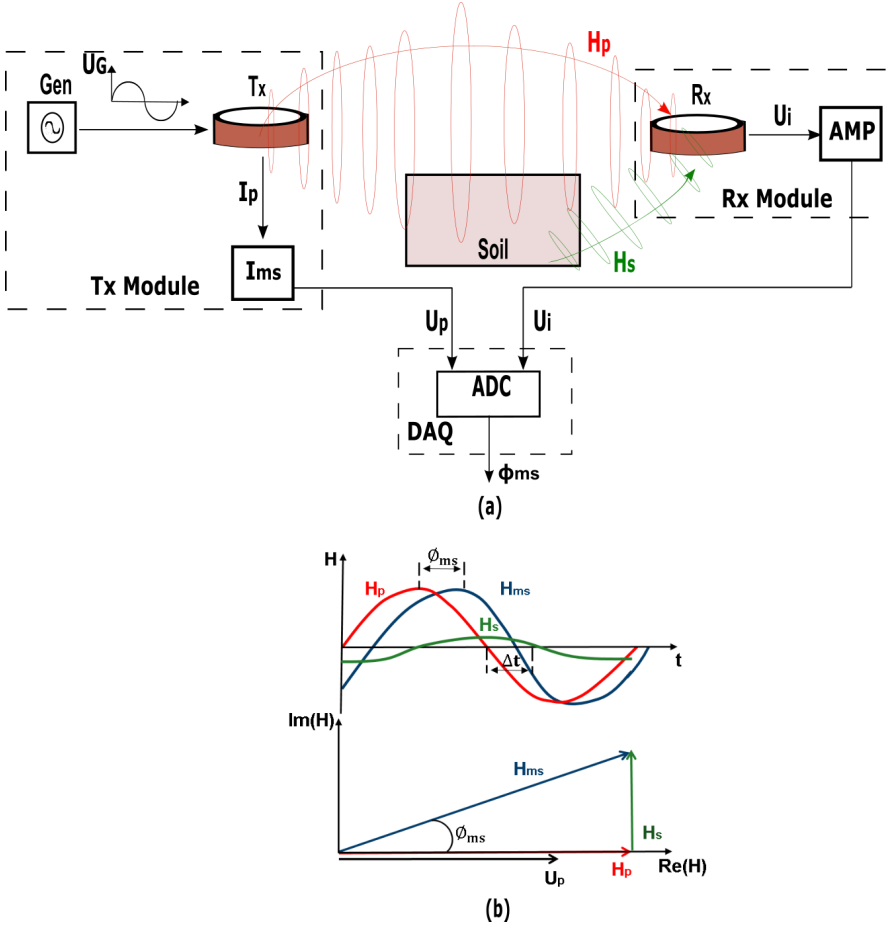


Figure 4.2.: (a) The signal flow diagram depicts the EMI measurement system’s setup for a single Tx – Rx arrangement. (b) Magnitude and phasor diagram for the primary, secondary and measured magnetic fields.

It should be noted that each of the system components can cause parasitic phase drifts and phase offsets, which can affect the accuracy of the measured phase. All the provided variables in the figure are considered as complex variables. To obtain accurate and reliable measurements, both signals are digitalised by an analog-to-digital converter (ADC) and further computation is performed to obtain the measured phase, Φ_{ms} , which is the difference

$$\Phi_{ms} = \Phi_i - \Phi_p \quad (4.2)$$

between H_{ms} and H_p . This computation assumes that H_p and the reference signal, I_p , have the same phase, Φ_p .

To get the soil electrical response during an EMI measurement, it is often more realistic to determine the transfer impedance (Z) of the system than the Rx voltage U_i shown in Figure 4.2. This parameter is a measure of the effectiveness of the system in transferring electromagnetic energy from the transmitter to the receiver. The transfer impedance hereby represents the ratio of the voltage induced at the receiver (U_i) to the current at the transmitter (I_{ms}) as:

$$Z = \frac{U_i}{I_{ms}}. \quad (4.3)$$

It is also interesting to note that in the context of the system description depicted in Figure 4.2, the transmitter voltage U_p can be represented in terms of Z and I_{ms} as:

$$Im\left(\frac{H_s}{H_p}\right) = Im\left(\frac{U_i}{Z * I_{ms}}\right). \quad (4.4)$$

4.1.2. Temperature Drift

In order to investigate the impact of variations in external ambient temperature on the measured phase and the occurrence of temperature drifts, a series of measurements were conducted using the previously presented measurement system. Throughout the acquisition of electromagnetic interference (EMI) data, the temperature sensors (section 4.1.1) were utilised to record the local internal temperature within the device using temperature sensor 3 (Figure 4.1) which measures the air temperature. The results of these measurements are depicted in Figure 4.3, which indicates that over a 30-hour period, the local internal temperature varied from 10°C to 40°C.

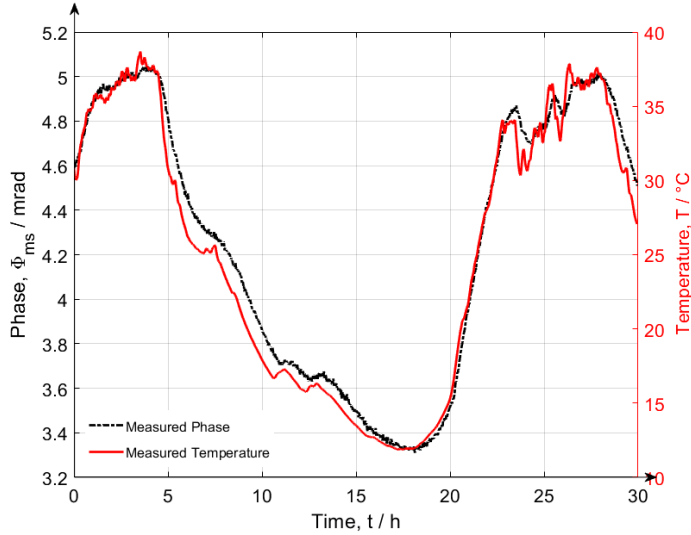


Figure 4.3.: The left axis shows the time series of the measured phase (black broken line). The right axis shows time series of the local internal (air) temperature (red solid line) from sensor 3.

This was accompanied by a corresponding change in the measured phase from 3 to 5.5 mrad. It should be noted that the device was placed at an elevation of 0.7 m to minimize the effects of soil properties on the measurement data. A correlated relation was observed between the phase drift and the external ambient temperature, despite the attempts to minimize soil influence. This is an indication that the thermal effect of the EMI system components cannot be neglected and thereby emphasizes the importance of correcting these drifts to achieve accurate and stable EMI data. This is particularly necessary in situations where no temperature stabilisation circuit is implemented in the measurement system hardware.

However, it should be noted that the drift of the phase signal is delayed in relation to the external ambient temperature due to the heat capacity of the system components. As a result, the components heat up is delayed compared to the air temperature sensor. The observed thermal drifts are complex and are influenced by both the instantaneous external ambient temperature and the thermal history of the EMI system components. This complexity arises from the fact that different electrical components possess varying thermal capacities, resulting in different thermal decay trends and a thermal legacy that cannot be monitored solely by measuring the instant (static) external ambient temperature [82]. A method is therefore required that can correct the temperature drifts by monitoring thermal dynamics of the EMI system.

4.1.3. Phase Drift Model

To model the temperature drift characteristics for EMI measurements, the phase drift model in Figure 4.4 is proposed. The diagram depicts an infinite impulse response (IIR) low pass filter, LPF (section 3.3) that takes the effective temperature (T_{eff}) of measured temperatures (T_{obs1} to T_{obsN}) as input. The LPF output is a modeled temperature (T_{mod}), which is used to determine a phase (Φ_{mod}) through spline interpolation with three reference points. The measured phase (Φ_{ms}) is then corrected by subtracting Φ_{mod} to obtain the corrected phase (Φ_{corr}), which is converted to ECa using the McNeill [41] approximation. The model also includes a parameter (Φ_{off}) to account for system offsets. The model consists of two paths: a dynamic phase drift model and a static phase drift model. The dynamic phase drift model, represented by the blue path in Figure 4.4, applies a low pass filter, (LPF) to the input, allowing the model to determine the delayed response of the local internal temperature of the system components to external ambient temperature changes. The LPF can be bypassed for static modeling (red path) where phase calibration is done using a look-up table alone.

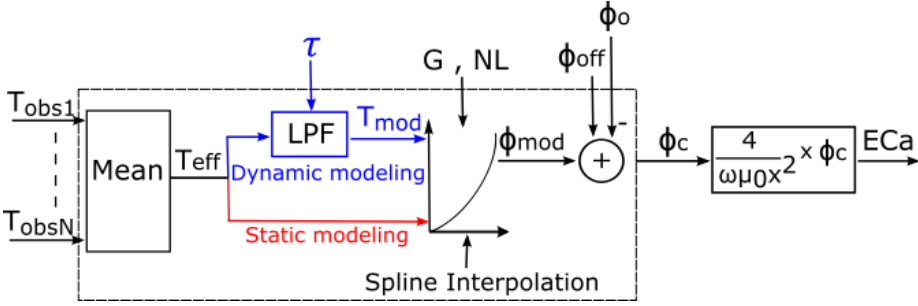


Figure 4.4.: Schematic representation of the phase drift model with static modeling (red path) and dynamic modeling (blue path) options.

This model also utilises a look-up table with cubic spline interpolation to facilitate the interpretation of temperature information in terms of phase values (section 3.4). In more detail, the dynamic phase drift model consists of two components: the LPF and the look-up table. The LPF is responsible for modeling the temperature response of the system's components to changes of the external ambient temperature.

The look-up table, on the other hand, is used to convert the temperature information into phase values. These two components work together to form a complete dynamic phase drift model. The static phase drift model, represented by the red path in Figure 4.4, bypasses the LPF and converts measured temperatures into modeled phase values using directly the look-up table. This model assumes that the temperature drift is constant over time and does not change with temperature fluctuations. Both models are controlled by calibration parameters, including the time constant τ of the LPF, the phase offset Φ_{off} of the system, the gain G , and a non-linear term NL .

These parameters are important for accurately modeling the temperature drift and predicting the system's phase response under different temperature conditions.

4.1.4. Effective Temperature Variation

The process of determining the effective temperature variation (T_{eff}) inside an EMI device involves careful evaluation and selection of temperature sensors to obtain a representative value of the local internal temperature. This is achieved by selecting sensors that have both fast response times to external ambient temperature changes and are distributed throughout the device's length. By doing so, a mean value of various temperatures across the instrument is obtained, which is representative of the local internal temperature.

However, it is important to note that local heating or cooling can result in deviating temperatures in certain sensors. Therefore, it is necessary to identify and exclude those sensors and only consider the ones that provide reliable readings. This ensures that the selected sensors are representative of the overall temperature inside the device. To obtain an effective time series of the temperature for the phase drift model, the average value over the selected sensors is used. This approach is more accurate than relying on individual sensor readings, as the mean value provides a more statistically reliable representation of the local internal temperature.

To ensure that the temperature uniformly changes throughout the device, the correlation coefficients of the selected temperature time series are calculated. This helps determine whether the selected sensors change identically with the external ambient temperature. If they do, then the condition for a representative temperature signal applies to the entire interior of the device. This is crucial information to be considered when building the drift model.

4.1.5. Drift Calibration Measurements

In order to determine the calibration parameters of the phase drift model, it is necessary to perform calibration measurements. However, it is important to minimise the influence of soil on the system's thermal drift, as this can affect the accuracy of the measurements. Additionally, the calibration method should be practical to carry out in the field. To meet these requirements, the EMI instrument was mounted on a wooden rack and raised to a height of 0.70 m in a garden near Niederzier, Germany, in July 2020. Great care was taken to ensure that there were no nearby power lines that could interfere with the measurements.

To investigate the impact of temperature on the measurement system, sixteen sets of ECa measurements were taken in VCP configuration over a period of 30 hours. This corresponded to 16 day and night cycles, allowing for a thorough examination of the effects of temperature on the instrument's performance. By conducting these mea-

measurements, it was aimed to determine the most accurate calibration parameters for the phase drift model. During the measurements using the custom EMI instrument, the temperatures recorded ranged from approximately 25°C to 58°C.

To ensure that the data collected were as accurate as possible, while minimizing the impact of soil conditions, a height of 0.70 m was chosen for the measurements. This height was deemed to be a reasonable compromise between experimental convenience and accuracy. To further ensure the accuracy of the measurements, calibration measurements were conducted using the VCP configuration (section 2.2). This configuration was found to be the least affected by changes in soil properties such as temperature and water content for the specified height, as reported by Robinson et al. [76].

After the measurements were conducted, model parameters were calculated for each of the 16 datasets. These parameters allow for a thorough analysis of the collected data and provide valuable insights into the underlying soil properties. The calibration parameters $m = (\Phi_{off}, \tau, G, NL)$ of the phase drift model, were determined by finding appropriate values that minimised the discrepancy between the measured phase Φ_{ms} and the modeled phase Φ_{mod} . To achieve this, an objective function was utilised, with the L2-norm [103] as the method for determining the misfit between the measured and modeled phase:

$$L_2(m) = \|\Phi_{ms} - \Phi_{mod}(m)\|_2 = \|\Phi_c(m)\|_2 \quad (4.5)$$

The L2-norm is a mathematical function that measures the distance between two vectors, in this case, Φ_{ms} and Φ_{mod} . The objective function was designed to minimise this distance by adjusting the calibration parameters until the discrepancy between the measured and modeled phases was as small as possible. In this process, the calibration parameters were optimised to accurately describe the behavior of the system being studied. This allowed for more accurate predictions and greater understanding of the system's behavior.

The objective function was minimised using the Nelder-Mead simplex algorithm [85] (section 3.1), which is a widely used optimisation algorithm for finding the optimal solution to a problem. This algorithm iteratively searches for the best set of calibration parameters that minimises the objective function. To initiate the optimisation process, starting values for the minimisation were calculated by fitting a linear model to the phase and temperature data. This provided initial values for Φ_{off} and G , which were used to begin the Nelder-Mead simplex algorithm.

The time constant τ was assigned an initial value of 1 s, which was deemed suit-

able for the system under consideration. The non-linear term NL was also assigned an initial value of 1, as it was assumed that it would not have a significant effect on the system's behavior. To evaluate the optimisation process, the root mean square error

$$RMSE = \sqrt{(\Phi_c - \text{mean}(\Phi_c))^2} \quad (4.6)$$

was calculated as a measure of the accuracy of the calibration parameters. A smaller $RMSE$ indicates a better fit between the measured and modeled values, and thus a more accurate set of calibration parameters.

4.1.6. Effect of Soil Conductivity Changes on the Calibration

The influence of the soil on instrument calibration is a topic of great importance in the field of geophysics and soil science. Soil properties can in general significantly affect the accuracy of measurements obtained by geophysical instruments as the electrical conductivity values measured will vary with changing soil properties like water content and salt concentration. As a result, it is essential to investigate and understand the impact of soil properties on instrument calibration and performance. A two layer synthetic soil model was used to investigate the influence of soil on instrument calibration. The first layer of the set-up represents air, which has a thickness equivalent to the height of the instrument ($h = 0.7\text{m}$) from the ground. Since the VCP configuration senses mostly the shallow part of the soil (section 2.2), elevating the instrument to a height of 0.7 m further decreases the device's sensitivity to soil influence. To check this the electrical conductivity of the first layer is set to a value EC_1 . The second layer represents a homogeneous soil volume with infinite thickness, and the electrical conductivity of this layer EC_2 was varied to model the effect of the system's sensitivity.

The choice of EC values for the two layers is critical for the success of the synthetic analysis and is selected based on the typical range of soil electrical conductivities found in the soil at the measurement location. The sensitivity of the measurement system is modelled using the cumulative response function in Equation 2.6. By varying the conductivity of the homogeneous half space and running the response function, the influence of the soil on the calibration is estimated. The EC_a is the sum of the product of the CRF for each layer and the electrical conductivity of the various layers which is calculated for the VCP coil configuration as

$$EC_a = EC_1 \cdot (1 - CRF^{VCP}) + EC_2 \cdot CRF^{VCP}. \quad (4.7)$$

4.2. Results and Discussions

4.2.1. Measured Temperature Distribution

The results of the exemplary calibration measurement #16 are presented in Figure 4.5, displaying the measured temperature values (T_{ms}) for all 10 sensors. The temperature values were obtained using 10 temperature sensors that were distributed throughout the EMI instrument to measure temperature variation within the device (section 4.1.1). The temperature variations across the sensors appear to be similar, with the exception of sensors 7, 9, and 10, which demonstrate higher overall temperature values. The elevated temperatures of these 3 sensors can be attributed to local self-heating of the modules (Heatsink, transmitter PCB and ADC respectively) to which they are attached.

As a result, these sensors are not considered representative of the uniform local internal temperature of the device and are therefore excluded from drift correction. Moreover, the temperature curves for sensors 1 and 3 indicate delayed reaction times, as evident from their temperature curves. This suggests that these sensors are also not suitable for the analysis and consequently were excluded from the study to ensure that the results obtained are accurate and representative of the local internal temperature of the device.

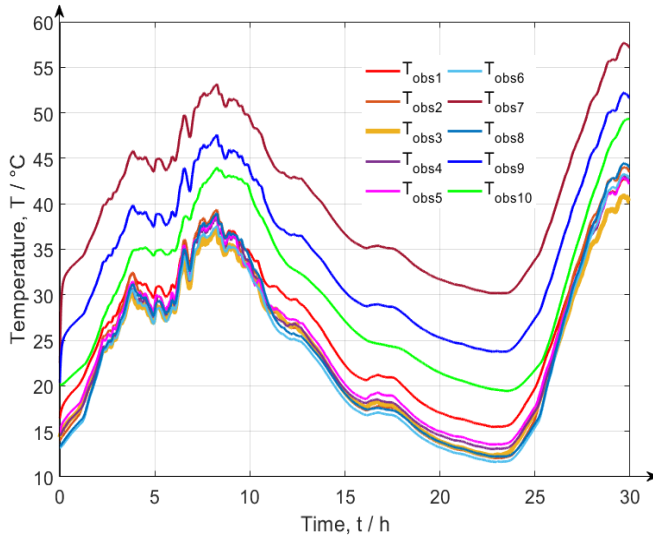


Figure 4.5.: Time series of measured temperature values, T_{ms} for calibration measurement #16.

Finally, the effective time series for the model was obtained using sensors 2, 4, 5, 6, and 8 for all measurements. In order to ensure that these sensors provide consistent readings, the correlation coefficients between the selected temperatures were calculated to determine if the temperature variations were uniform throughout the entire device. The results showed that the smallest correlation coefficient obtained among the selected temperature curves of all 16 measurements was never less than 0.994. This indicates that the temperature inside the system is uniform, as all the selected sensors consistently measured temperature variations that are highly correlated with each other. Therefore, it can be concluded that sensors 2, 4, 5, 6, and 8 are reliable for calculating the effective time series for the model and can be used with confidence in subsequent analyses.

4.2.2. Performance of Calibration

To assess the reliability and robustness of the calibration method, the 16 calibration measurements were analysed individually. The results of fitting each individual measurement are presented in Table 4.1, along with the corresponding root mean square error ($RMSE_1$) of the ECa values. The $RMSE_1$ values (obtained from correcting measured datasets with calibration parameters obtained from fitting the respective datasets) varied across the 16 datasets, ranging from $0.31 \text{ mSm}^{-1}\text{K}^{-1}$ to $0.56 \text{ mSm}^{-1}\text{K}^{-1}$, with a mean value of $0.42 \text{ mSm}^{-1}\text{K}^{-1}$ (equivalent phase of about $11.9 \mu\text{radK}^{-1}$). The results obtained suggest that the calibration method is relatively robust, as the variation in $RMSE_1$ values across the different datasets is relatively small.

Moreover, the mean $RMSE_1$ value of $0.42 \text{ mSm}^{-1}\text{K}^{-1}$ (equivalent phase of 0.012 mradK^{-1}) indicates that the calibration method is able to estimate ECa values with a high degree of accuracy, as this value is relatively small compared to the range of measured ECa values. The calibration measurements showed that the values of the calibration parameters, namely τ , G and NL , were consistent across all measurements. This suggests that the calibration method and approach were reliable. The parameter τ is an important measure of the response time of the various components of the measurement system to temperature changes.

A higher value of τ indicates that the components of the system take longer to respond to changes in temperature. In this case, the mean value of τ was approximately 1107 seconds, which translates to around 18 minutes. This means that it takes approximately 18 minutes for the components of the measurement system to respond to changes in internal measured temperature. This delay is most likely due to the coils of the system, which have a large thermal inertia as indicated by previous studies [13,15]. Thermal inertia here refers to resistance to temperature change, and in the context of the measurement system, it represents the time it takes for the coils to adjust to temperature changes.

The value of G , which represents the drift in ECa, was determined and found to vary slightly around a mean value of $2.27 \text{ mSm}^{-1}\text{K}^{-1}$ with a phase of approximately 64.5

Table 4.1.: The calibration parameters: time constant (τ), gain (G which is converted to ECa), and non-linear term (NL) were determined from fitting the 16 datasets. The corresponding $RMSE_1$ (from correcting each individual dataset with its own fitted calibration parameter) and $RMSE_2$ (from the evaluated mean of all 16 calibration parameters which is applied for correction of each individual dataset) were also determined. The mean and standard deviation (std) of the calibrated parameters based on the 16 measurements were also calculated.

Data	τ (s)	G ($mSm^{-1}K^{-1}$)	NL	$RMSE_1$ ($mSm^{-1}K^{-1}$)	$RMSE_2$ ($mSm^{-1}K^{-1}$)
1	1201.10	2.27	1.17	0.36	0.37
2	1176.82	2.36	1.05	0.39	0.42
3	1038.07	2.25	1.18	0.40	0.47
4	968.33	2.23	1.22	0.40	0.64
5	1198.90	2.25	1.18	0.41	0.46
6	1076.17	2.25	1.19	0.31	0.32
7	1121.04	2.25	1.08	0.31	0.42
8	1038.55	2.24	1.24	0.44	0.59
9	1147.57	2.28	1.25	0.39	0.48
10	1154.75	2.26	1.16	0.56	0.61
11	1122.22	2.26	1.21	0.39	0.39
12	1041.29	2.26	1.22	0.37	0.47
13	1152.85	2.25	1.18	0.55	0.57
14	1007.87	2.29	1.25	0.37	0.41
15	1177.05	2.32	1.29	0.53	0.63
16	1104.52	2.26	1.20	0.48	0.49
mean	1107.94	2.27	1.19		
std	71.78	0.03	0.06		

$\mu radK^{-1}$. The accurate determination of G was found to be crucial for correcting the drift. The standard deviation of the fitted ECa drift was only $0.03 mSm^{-1}K^{-1}$, indicating that it is relatively low compared to the mean value of G . The non-linearity factor (NL) varied around a mean value of 1.19, which means that the phase values were non-linearly related to temperature (as principally shown in Figure 3.4).

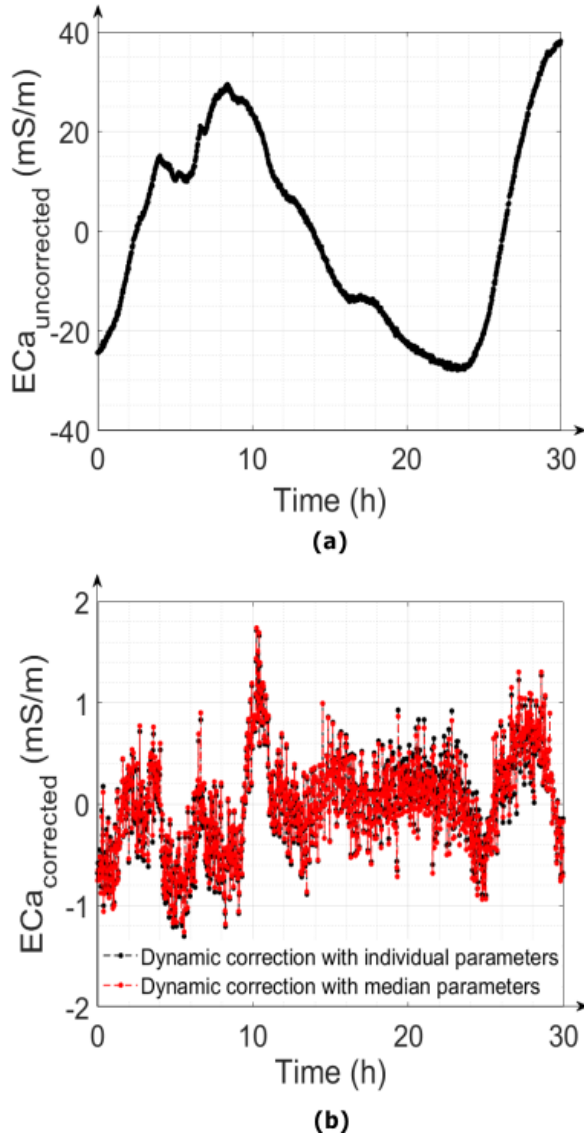


Figure 4.6.: (a) Uncorrected ECa values for calibration measurement #16. (b) Corrected ECa values for measurement #16. ECa values were shifted to have a zero mean.

This non-linear term was therefore deemed essential for correcting the drift effects. The study also investigated the effect of setting NL to 1.0 (i.e., a linear model).

The results showed that by doing so, the mean of the $RMSE_1$ increased from 0.42 $\text{mSm}^{-1}\text{K}^{-1}$ to 1.2 $\text{mSm}^{-1}\text{K}^{-1}$. The mean of all 16 calibration parameters τ , G and NL from Table 4.1 (i.e. 1107.94 s, 2.27 ($\text{mSm}^{-1}\text{K}^{-1}$), 1.19 respectively) were now applied for correction on each individual dataset 1 - 16. This process produced an additional 16 root mean square error ($RMSE_2$) values, which were slightly higher than the original $RMSE_1$ values. The mean $RMSE_2$ value, calculated using the single set of mean calibration parameters, was found to be 0.48 $\text{mSm}^{-1}\text{K}^{-1}$.

This value was only marginally higher than the mean value of the $RMSE_1$ values (0.42 $\text{mSm}^{-1}\text{K}^{-1}$) calculated using individual calibration parameters. Considering the fact that the results obtained using both individual and mean calibration parameters over the course of 16 days were similar suggests that the calibration parameters are reproducible and the system is capable of long-term calibration. Therefore, it was concluded that the calibration method is reliable and can be used for extended periods of time without significant degradation in accuracy.

To demonstrate the effectiveness of the drift correction and the calibratability of this process, the time series of ECa values were analysed. Specifically, by comparing the uncorrected and corrected ECa values of measurement #16 using both individual calibration parameters and mean calibration parameters, it was possible to determine the efficiency of the drift correction method. These values are presented in Figure 4.6a and Figure 4.6b, respectively. In Figure 4.6a, the uncorrected data shows a peak-to-peak ECa value of approximately 62 mSm^{-1} , while the corrected data (using the mean of all calibrated parameters) in Figure 4.6b displays an ECa value of around 3 mSm^{-1} . This strong contrast indicates that the drift correction process is highly effective in reducing temperature drifts.

Furthermore, Figure 4.6b shows that the ECa values for both individual and mean calibration parameters are similar, which suggests that the drift correction method is adjustable and can be applied to a variety of different calibration parameters without significantly affecting the results. In terms of quantifying the effectiveness of the correction method, the $RMSE$ of the corrected ECa values is 0.48 $\text{mSm}^{-1}\text{K}^{-1}$ for individually calibrated parameters and 0.49 $\text{mSm}^{-1}\text{K}^{-1}$ for the mean calibration parameters. These values indicate that the drift correction process is highly effective at reducing the error associated with ECa measurements. Note that in order to focus on the changes in ECa rather than absolute values, the ECa values shown in Figure 4.6a and Figure 4.6b were shifted to have a zero mean.

4.2.3. Advantage of Implementing the LPF in the Drift Correction Model

This section aims to demonstrate the advantages of using dynamic correction with a LPF in comparison to static correction of temperature drift without a LPF. The

figure presented in Figure 4.7 displays the measured ECa values (in pink), the ECa values generated through dynamic modeling (in black), and the ECa obtained through static modeling (in red) (all adjusted to have a mean of zero to indicate ECa differences rather than absolute values). These values are plotted as a function of effective temperature T_{eff} calculated from the mean of all measured temperature values. The figure reveals the emergence of temperature dependent hysteresis loops that result from the fluctuations in the local internal temperature of the measurement device. These hysteresis loops represent the accumulation of previous and current warming and cooling cycles, a phenomenon that has been previously reported by Huang et al. [78].

The static correction approach is not sufficient to accurately analyse the measurement device's drift properties over time since it fails to replicate the hysteresis loops observed in the data. However, the dynamic approach, which incorporates a LPF, can effectively reproduce these hysteresis effects. The dynamic approach uses a feedback loop that adjusts the correction based on the current and past measurements, providing a more accurate and reliable analysis of the measurement device's drift properties over time. Therefore, the results from Figure 4.7 highlight the importance of using dynamic correction with a LPF for a more accurate analysis and correction of temperature dependent drift effects.

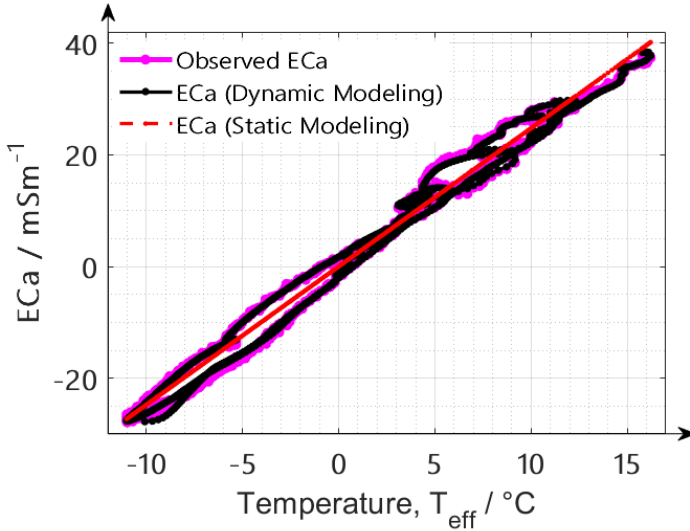


Figure 4.7.: Plot for calibration measurement #16 showing ECa as a function of temperature.

In order to demonstrate the importance of implementing a LPF, the effects of both static (Figure 4.8a) and dynamic (Figure 4.8b) correction approaches on the time series data of measurement #16 were analysed. Additionally, the *RMSE* for single

parameter correction in both cases were calculated (in both plots, the ECa values have been adjusted to a mean of zero to better focus on changes in ECa rather than their absolute values). The analysis has shown that when using static correction, the peak-to-peak range of ECa values is approximately 4 times higher than that obtained with dynamic correction. Furthermore, the $RMSE_1$ value increases significantly to $1.94 \text{ mSm}^{-1}\text{K}^{-1}$ when the LPF is not employed, compared to a significantly lower value of $0.42 \text{ mSm}^{-1}\text{K}^{-1}$ obtained with dynamic correction. This lower $RMSE_1$ value obtained with the LPF indicates that the predicted ECa values of the phase drift model (section 4.1.3) are closer to the actual ECa values measured.

This highlights the critical role played by the LPF in minimizing the impact of temperature drift on measurement accuracy. The results of this analysis underscore that without the LPF, the static correction method is insufficient for achieving the level of advanced accuracy necessary. On the other hand, the dynamic approach with LPF implementation can successfully capture and correct for temperature-induced hysteresis effects, providing significantly more precise measurements with minimal error.

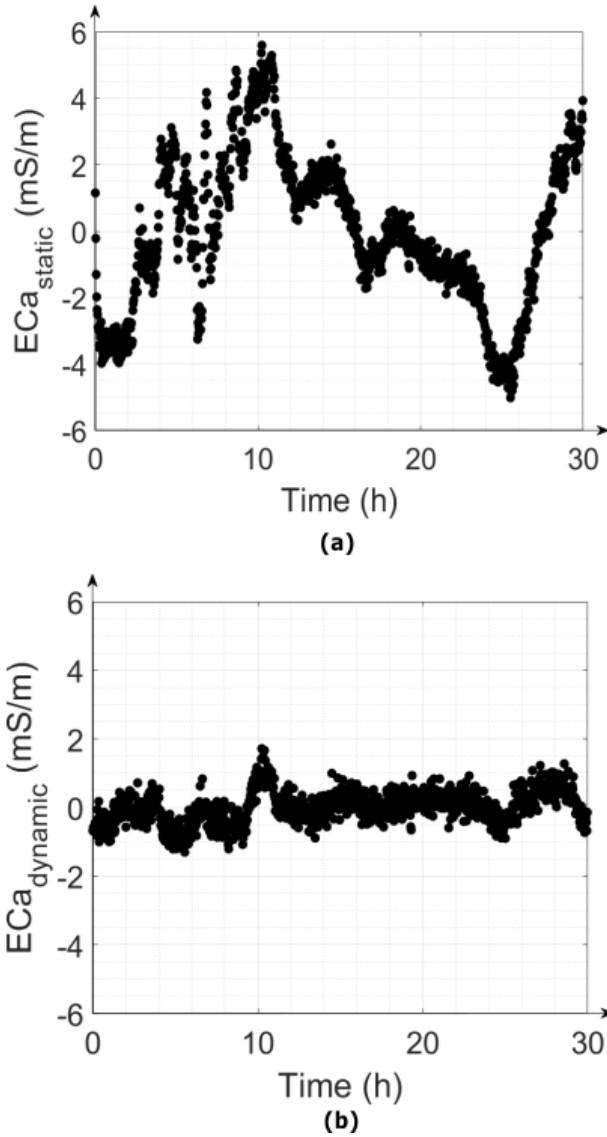


Figure 4.8.: (a) Plot of static drift correction (without LPF) and (b) Plot of dynamic drift correction (utilizing LPF). ECa values were shifted to have a zero mean.

4.2.4. Effect of Soil Conductivity Changes on the Calibration

To explore the potential impact of changes in soil properties due to temperature variations on the calibration of the measuring instrument, a two-layer model was utilised (shown in Figure 2.4). The first layer, which had a thickness of 0.70 m (section 4.1.6), was assumed to be composed of air and was assigned a conductivity of 0 mSm^{-1} . The second layer was considered to be a homogeneous soil layer of infinite thickness. To model the sensitivity of the measurement system, the cumulative response function (CRF) presented by McNeill [41] was used. Through this analysis, it was observed that a 1 mSm^{-1} increase in the electrical conductivity of the soil in the first few meters resulted in a 0.37 mSm^{-1} increase in the measured ECa for the VCP configuration with an intercoil spacing of 1.20 m at a height of 0.70 m.

Assuming now that the soil conductivity changes by approximately 2 % per K, as reported by Corwin and Lesch [48], it can be inferred that the expected drift in ECa due to changes in soil temperature is approximately 0.74 % per K. However, it is important to note that this value represents a worst-case scenario since the soil does not heat up immediately. Assuming that the soil has a typical electrical conductivity of 10 mSm^{-1} and taking into consideration that the relative change in ECa due to soil temperature is less than 0.74 % per K (i.e. $0.37 \text{ mSm}^{-1} \times 0.02 \text{ K}^{-1} \times 100$) of the soil EC, it can be concluded that the expected worst-case change in ECa due to soil temperature is around $0.07 \text{ mSm}^{-1}\text{K}^{-1}$. This value is much smaller than the system drift of $2.27 \text{ mSm}^{-1}\text{K}^{-1}$, indicating that changes in soil electrical conductivity during calibration measurements will have a negligible effect.

Therefore, for an intercoil spacing of 1.2 m, it can be concluded that the effect of changes in soil electrical conductivity due to temperature during calibration measurements will not significantly impact the accuracy of the calibration measurements, and thus, can be disregarded. As the intercoil spacing decreases, the impact of soil on the accuracy of the measurements also decreases. For instance, if the intercoil spacing is reduced to 0.4 m, it is estimated that the expected change in ECa due to soil temperature changes would be only around $0.003 \text{ mSm}^{-1}\text{K}^{-1}$, while the expected system drift would be approximately $20.4 \text{ mSm}^{-1}\text{K}^{-1}$, assuming that the measured phase values of the system drifts are independent of the intercoil spacing.

On the other hand, when the intercoil spacing is increased, the effect of soil on the accuracy of the measurements becomes more significant. For example, at an intercoil spacing of 6 m, the anticipated ECa change due to soil temperature variation would be approximately $0.015 \text{ mSm}^{-1}\text{K}^{-1}$, while the expected system drift would only be around $0.09 \text{ mSm}^{-1}\text{K}^{-1}$. This is because as the intercoil spacing is increased, the sensing depth also increases, making the system more sensitive to the electrical properties of the underlying soil. However, it should be noted that these estimates represent worst-case scenarios, as they assume that the temperature of the soil changes uniformly throughout the entire sensing volume. In reality, only the temperature of the

topsoil changes, which could lead to more localised and less significant changes in the electrical properties of the soil.

In summary for this part of the thesis report, a new technique has been introduced for correcting drifts in EMI measurements that are temperature dependent and takes into account the response of system components to varying external ambient temperatures. This technique involves using a low pass filter (LPF) model to replicate the dynamic characteristics of the measured drifts. The parameters that control the model are the time constant (τ) from the LPF, the gain (G), and the non-linear variable (NL) of the LuT, as well as the system phase offset (Φ_{offset}). To validate the effectiveness of the correction method, a customised EMI instrument was used to measure the apparent electrical conductivity (ECa) and local internal temperature at 10 locations simultaneously. The instrument was positioned at a height of 0.70 meters above the ground. The EMI measurement system used in the study was optimised for low drift, but did not have internal drift correction circuitry.

In this study, a total of 16 measurements was conducted, each lasting 30 hours, which were then evaluated. The results showed that the mean drift was approximately $2.27 \text{ mSm}^{-1}\text{K}^{-1}$, with a standard deviation of $30 \text{ }\mu\text{Sm}^{-1}\text{K}^{-1}$ across the different measurements. These drift values could significantly affect the accuracy of the measurements, especially when taken at varying outdoor temperatures. To mitigate this issue, commercial EMI systems typically include internal correction circuits or additional correction tables. Without such corrections, the measurements would be considered inaccurate and unreliable. The findings presented here suggest that despite some drifts in the data, they remain stable with only a $30 \text{ }\mu\text{Sm}^{-1}\text{K}^{-1}$ variation, and can be largely corrected using the proposed correction method. After applying the correction method to the 16 calibration datasets with the mean value of all calibration parameters, the mean root mean square error (RMSE) of all datasets is only $0.48 \text{ mSm}^{-1}\text{K}^{-1}$.

This correction method improves the observed ECa values by a factor of 30 when compared to raw observed data. The study also found that the dominant drift source exhibited a delayed response of approximately 18 minutes to internal temperature changes. Taking this delay into account proved to be crucial, as comparison with static modeling and correction resulted in a higher RMSE value, with a mean of $1.94 \text{ mSm}^{-1}\text{K}^{-1}$. These results demonstrate the effectiveness of the proposed dynamic correction method and emphasise the importance of considering time-delay effects when modeling and correcting ECa data.

5. Non-uniform Temperature Drift Correction

In the previous chapter, the impact of temperature drift on EMI measurements was explored, and a new correction method was proposed. However, this method was developed under the assumption that the temperature distribution in the measurement device is uniform. In real-world scenarios, the temperature distribution may not be uniform, especially if the instrument is partially shaded. Therefore, it is necessary to investigate further advanced approaches.

This chapter presents an improved temperature drift correction method that mitigates drift effects due to non-uniform temperature distributions. The chapter begins by introducing a modified EMI measurement instrument and providing a detailed description of its features. The new correction method is then presented, which utilises two low-pass filters (LPFs) to model the system delays caused by non-uniform temperatures. These delays are then applied for drift correction.

The proposed correction method is expected to be more effective in scenarios where the temperature distribution is not uniform. By using two LPFs to model the system delays, the method is able to correct for temperature drifts caused by both uniform and non-uniform temperature distributions. Overall, the new correction method is expected to provide more accurate and reliable EMI measurements under more complex conditions.

5.1. Materials and Method

5.1.1. Measurement System

The system depicted in Figure 5.1 uses a modified version of a measurement system that has been previously developed and explained by Mester et al. [65] and described in detail by Tan et al. [82] as well as Tazifor et al. [104] and Tazifor et al. [105]. The measurement system is comprised of a generator unit (Gen) that supplies the Tx with AC current at a frequency of 10 kHz, a transmitter coil (Tx), and three receiver coils (R_{x_1} , R_{x_2} and R_{x_3}), which are spaced at a distance (x) of 0.4 m between each coil. Additionally, the data acquisition unit (DAQ) contains various components including a 24-bit analog-to-digital converter (ADC), a microcontroller (μC) used to control the hardware, an integrated computer (IC) containing the measurement software based on

MATLAB and 9 temperature sensors distributed throughout the measurement device.

These parts are all enclosed within a polyvinyl chloride pipe (PVC). Specifically, temperature sensors 2 and 6 monitor the PVC temperature, while sensors 3, 4, and 5 measure the air temperature. Sensor 7 records the heat sink temperature, sensor 8 measures the temperature of the transmitter coil, and sensor 9 records the temperature of the printed circuit board (PCB) of the transmitter coil. Temperature sensor 1 was defective and therefore excluded from analysis. The system is powered by a 12 V battery and has a length of 243 cm and a width of 16 cm. In this study, the analysis is centered on Rx3, which is situated 1.2 m away from the Tx. An external personal computer operates the entire set-up using wireless local area network (WLAN).

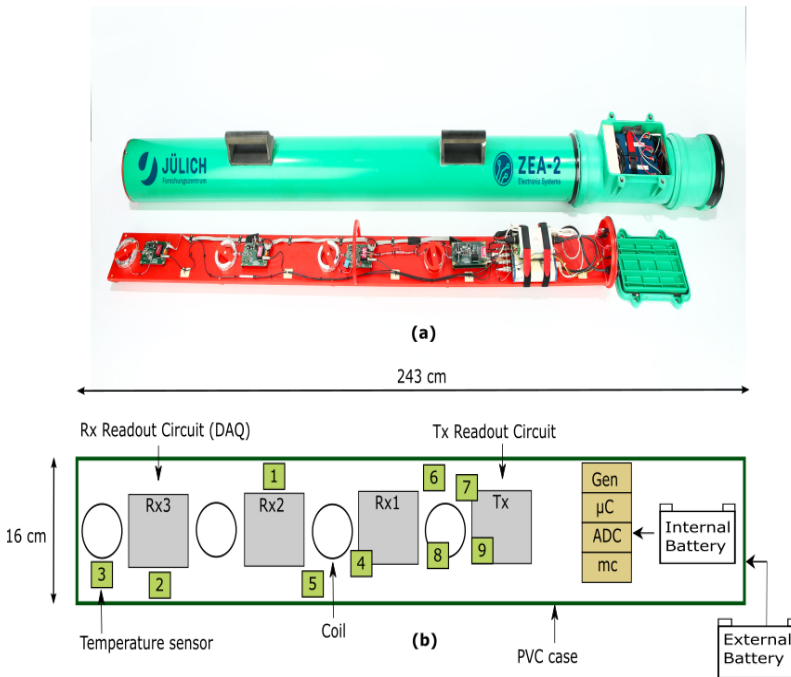


Figure 5.1.: (a) Photo of the modified custom EMI instrument; (b) Simplified schematic representation of the measurement system.

The measurement system described in this study was utilised to conduct 21 calibration measurements at different locations within the Research Center Jülich (Forschungszentrum Jülich GmbH), Germany. The primary objective of developing this system was to explore modular and scalable system concepts and to examine the effects of interference such as system drifts. The measurements were taken during the summer periods of 2021 and 2022, during which the temperature ranges and variations varied.

The temperature sensors embedded in the measurement system recorded temperatures ranging from approximately 10°C to 50°C during the calibration measurements.

To minimise soil effects, the measurement device was also raised 0.7 m above the ground using wooden supports, and data was collected in the VCP configuration. In a previous study by Tazifor et al. [104] (chapter 4), it was demonstrated that for a measurement taken at a height of 0.7 m and an inter-coil spacing of 1.2 m, the expected ECa change due to soil temperature changes is approximately 0.07 mSm⁻¹K⁻¹ (worst-case). This value is relatively low compared to the expected system drift, which is greater than 1 mSm⁻¹K. Therefore, to perform an effective temperature drift analysis, only temperature data with a range of at least 10 K were considered. As a result of this criterion, only 15 datasets were ultimately used in the study. Additionally, only measured data collected after a warm-up time of 2 hours were considered to ensure the accuracy of the measurements.

5.1.2. Drift Correction Model

A model for phase drift is presented in Figure 5.2, wherein pre-selected measured temperatures denoted as T_{ms} are utilised as inputs and used to model the temperature dependent dynamic characteristics of the measurement system using two low-pass filters (LPF_1 and LPF_2) respectively. The LPFs are used to estimate the delayed response of the local internal temperature of the system components to external ambient temperature variations.

The LPF generates the modelled temperatures T_{mod1} and T_{mod2} as outputs. To facilitate the conversion of modelled temperature information into modelled phase values Φ_{mod1} and Φ_{mod2} respectively, a look-up table (LuT) with cubic spline interpolation is used (section 3.4). The combination of the two LPFs and the LuT constitute the complete phase drift model, which is described in more detail subsequently.

The calibration parameters that control the phase drift model are the time constant (τ) from the LPF, the gain (G), and the non-linear variable (NL) of the LuT, as well as the system phase offset (Φ_{offset}). The offset (Φ_{offset}) is not determined in this work, rather it can be determined after drift correction based on a method proposed by Tan et al. [106]. Their method simultaneously determines calibration parameters including multiplicative and additive factors for different coil configuration, as well as an inverted 1D horizontally layered subsurface model consisting of electrical conductivity values and the corresponding thicknesses for each layer.

Other methods for offset calibration have also been implemented by von Hebel et al. [107] who used electrical resistivity tomography with Dipole-Dipole and Schlumberger electrode arrays and vertical electrical soundings. All three methods obtained robust calibration results. The drift model is based on the infinite impulse response (IIR) filter function described in detail by Tazifor et al. [104] and Tazifor et al. [105]

(section 3.3). The inputs for the drift model are pre-selected measured temperatures T_{ms} , which are transformed in a delayed response T_{mod} using the time constant parameter τ and the T_{mod} of the previous time step (Equation 3.17). Here, the filter coefficients a_1 , b_0 and b_1 are also determined using Equations 3.15 and 3.16 respectively.

The LuT has a temperature range from 0°C to 50°C , which is determined based on the measured temperature range. To construct the LuT, three reference temperature points are established, namely $T_{ref_{min}} = 0.0^\circ\text{C}$, $T_{ref_{mid}} = 25.0^\circ\text{C}$, and $T_{ref_{max}} = 50.0^\circ\text{C}$ as described in section 3.4. These reference points serve as the basis for determining the corresponding reference phases, denoted as $\Phi_{ref_{min}}$, $\Phi_{ref_{mid}}$, and $\Phi_{ref_{max}}$, respectively, using the parameters G and NL .

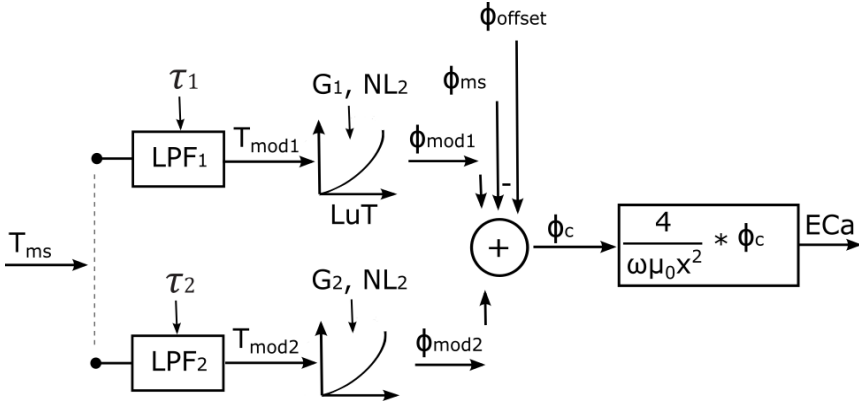


Figure 5.2.: Representation of the phase drift model for temperature drift correction.

By using the LuT and cubic spline interpolation, the modelled temperatures T_{mod1} and T_{mod2} for the 2 LPFs are converted into modelled phases Φ_{mod1} and Φ_{mod2} respectively (chapter 3). The corrected phase Φ_c was then calculated from Φ_{mod1} and Φ_{mod2} as

$$\Phi_c = \Phi_{ms} - \Phi_{mod1} - \Phi_{mod2}. \quad (5.1)$$

and can be converted to ECa values using the approximation in Equation 2.5.

5.1.3. Selection of Temperature Sensors

Determining the optimal placement of temperature sensors on an EMI device can be a challenging task. This is because different components within the device will react

to external ambient temperature changes with different delays. As such, there is a question of whether the sensors should be placed on components with large thermal capacities, such as coils, which react slowly to temperature changes, or simply in the air, which reacts more quickly. To address this issue in our specific case, it is assumed that the components that are susceptible to drift are located in two regions of the EMI device, notably, the Tx coil and Rx coil regions, with an inter-coil spacing of 1.2 m where the entire electronics are located for this coil spacing.

In the Rx region, two sensors are used to measure the air and PVC temperatures (sensors 3 and 2, respectively). These measurements are then compared to determine which sensor is better suited for drift correction. Similarly, in the Tx region, four sensors are used to measure the PVC, heat-sink, Tx coil, and PCB temperatures (sensors 6, 7, 8, and 9, respectively). These measurements are then compared to determine which sensor is better suited for drift correction. Suitable sensors for drift correction were identified by modeling the delayed responses of all 8 measured temperature time series. To achieve this, the first part of the drift correction model in Figure 5.2 is used (excluding the G and NL calibration parameters), which consists solely of low-pass filters (LPFs).

The primary aim of this analysis is to determine whether temperatures that respond quickly can be used to model temperatures with delayed responses, and thus, replace them. Furthermore, this approach is also used to evaluate the ability of the LPFs to accurately model the system component delays. To facilitate comparison between modeled and measured temperatures and to simplify analysis, the root mean square error (RMSE) of the difference between the modeled and measured temperatures is calculated for each combination of the two after fitting the optimal value for the time constant (τ). The RMSE values obtained will help provide valuable insights into the effectiveness of the LPFs in modeling system component delays and identifying suitable sensors for drift correction.

5.1.4. Assessment of Spatial Temperature Variation

To evaluate whether temperature drift correction with two LPFs allows to correct for fast non-uniform temperature variations, it is of interest to determine the temperature distribution within the measurement device. Here the 2 regions described in the previous section are considered, where the drifts are expected to occur. In the first case, the 2 regions of interest (Tx and Rx regions) could have similar temperature variations. With reference to Tazifor et al. [104] (chapter 4), it is assumed that a model with only one LPF will suffice to correct the drift effects.

In a second case, the temperature time series in the 2 regions may have different temperature variations. Here a model with two LPFs will be required to correct the drifts. Therefore to have a better understanding of the effect of uneven temperature variation on the drifts, two types were identified, notably, uniform temperature varia-

tion (UTV) and non-uniform temperature variation (NUTV). UTV describes the case where there is only one dominant temperature component which describes most of the variability in the temperature data measured.

In the case of NUTV, there are multiple significant temperature components that contribute to the variability of measured temperature data which must all be considered for drift modelling and correction. As an universal quantitative method to differentiate UTV and NUTV datasets with temperatures of two or more relevant regions, the principal component analysis (PCA) of the measured temperature data was used (section 3.5). After calculation of the eigenvalues from PCA, they were normalised with the sum of all eigenvalues. These normalised eigenvalues ($E_{val,N}$) facilitate the comparison of different temperature time series with respect to their homogeneity.

The more uniform the temperature variation in a dataset, the closer the magnitude of the first normalised eigenvalue $E_{val,1N}$ is to 1. Here, a threshold value denoted V_{th} was used to differentiate between UTV and NUTV datasets. All temperature datasets with $E_{val,1N}$ greater than or equal to V_{th} were considered UTV data and all datasets with $E_{val,1N}$ less than V_{th} were considered NUTV datasets. It is worth noting that in the case of UTV data, it is also possible that a model with two LPFs may be better to correct temperature drift effects. This is the case where there are electronic components which contributes to drift effects with different reaction times to temperature changes. In contrast to the phase drift model proposed by Tazifor et al. [104] (section 4.1.3), it may be useful to use a model with more than one LPF with the same input temperature.

5.1.5. Determination of the Representative Calibration Parameters

To estimate the calibration parameters $m=(\tau_1, G_1, NL_1, \tau_2, G_2, NL_2)$ for the two LPFs, the misfit between the measured phase Φ_{ms} and the modelled phase Φ_{mod} was calculated using the objective function

$$RMSE = \sqrt{\|\Phi_c - mean(\Phi_c)\|_2} \quad (5.2)$$

based on the L2-norm. Here, the objective function $RMSE$ is used for optimisation without the offset (mean value). It should be noted that the drift model is not limited to only two LPFs but can be adapted to 3 or more as per requirement. In this case, 3 more parameters are added for every additional LPF. Initial tests with local search algorithms showed that the optimisation results were affected by local minima in the objective function, as indicated by different results for different starting values

of the calibration parameters.

For this reason, a global optimisation method named shuffled complex evolution [93] was used to minimise the objective function (section 3.2). In this work, the optimisation search with this algorithm was stopped when the objective function value did not improve by more than 1% in the last 20 loops.

Since a suitable set of calibration parameters should be able to correct all datasets, it is assumed that the intrinsic drift parameters are stable over longer periods of months or years, and do not vary with time. If this would be the case, it would be highly challenging to calibrate the system for drift. Therefore, all datasets were simultaneously fitted. Preliminary analysis showed that the models with more than one LPF showed strong dependencies between individual parameters. For example, it is possible to obtain the same overall G for several combinations of G_1 and G_2 when using two LPFs. It is therefore required to set adequate boundaries for the parameter space. To obtain such boundaries, the range of τ_1 , G_1 , τ_2 , G_2 were determined for a linear version of the drift model by removing the NL term (i.e. setting NL_1 and NL_2 to 1). Wide boundaries were used for the remaining parameters: $0 \text{ s} \leq \tau_1, \tau_2 \leq 4000 \text{ s}$, $-e^{-4} \text{ radK}^{-1} \leq G_1, G_2 \leq e^{-4} \text{ radK}^{-1}$.

To only consider data with approximately linear behaviour, the calibration for the initial ranges considered only a subset of the data. In particular, only data were considered in a reduced temperature range around the mean temperature with a range of 10 K. Furthermore, only NUTV datasets were used to reduce the degree of dependence between the parameters because it is anticipated that the NUTV datasets need two LPFs for drift modelling. The range of the respective calibration parameters across all NUTV datasets were used to estimate new and smaller boundaries for the feasible parameter space. In the final step, the new boundaries were used to calibrate all datasets using the non-linear drift model and the full temperature range ($0^\circ\text{C} - 50^\circ\text{C}$).

In the following, three types of calibrations were performed (named A, B and C) to evaluate the performance of drift models with one and two LPF. In type A calibrations, all datasets were individually fitted with the objective function $RMSE$ in Equation 5.2, using temperature measurement from sensors 3 and 9 and two LPFs. Type A calibrations are expected to provide the lowest fitting error and will serve as a reference. In type B calibration, all datasets were simultaneously fitted with the same temperature sensors and two LPFs. Finally, type C calibration only considered one LPF and the mean of temperature sensors 3 and 9 to perform simultaneous fitting on all datasets and using the initial wide boundaries for the parameter space.

5.2. Results and Discussion

5.2.1. Selection of Temperature Sensors

The 8 temperature sensors were fitted with each other using the LPF part of the drift model to identify the most relevant temperature sensors suitable for drift correction. The plot in Figure 5.3 shows the RMSE value between modelled and measured temperatures to identify representative temperature sensors suitable for drift correction. The colour bar shows the RMSE between modelled and measured temperatures (in Kelvin). An error value of 0 indicates that one sensor can perfectly replace another temperature sensor.

It can be seen that the temperature sensors 2 and 3 in the Rx region (Figure 5.1) result in a small *RMSE* (less than 0.5 K), whereby, sensor 3 models sensor 2 with a delay τ of 336 s. Furthermore it can be seen that sensors 6, 7, 8 and 9 in the Tx region result in a small RMSE (less than 0.45 K), whereby, sensor 9 models sensor 8 with a delay τ of 337 s. Sensor 7 is placed on the heat-sink also showed a small error (less than 0.35 K), but was not considered because the self-heating may not always be representative of the temperature in this region. Temperature sensor 4 in the middle region is more similar to the sensors in the Tx region whereas the temperature sensor 5 is more similar to the Rx₃ region.

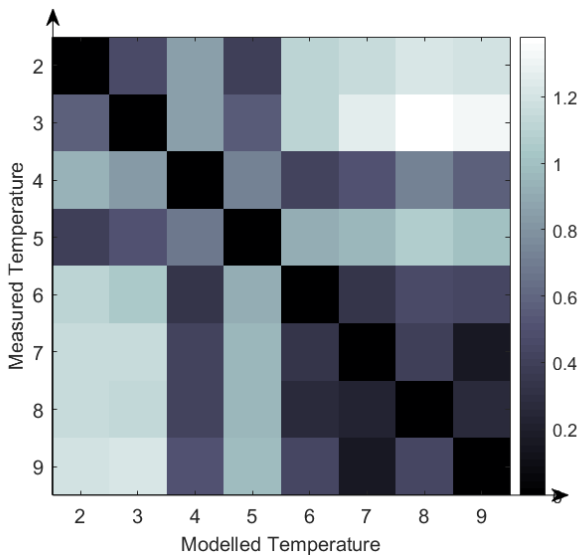


Figure 5.3.: Representation of root mean square error (RMSE) between modelled and measured temperatures.

However, there are no drift-relevant components in this middle region that have an influence on the drift behaviour for the intercoil spacing of 1.2 m. The results show

that slow reacting sensors placed on system components with large heat capacities such as the Tx coil (measured by temperature sensor 8), can be modelled sufficiently well by sensors with a fast response. On the other hand, it is difficult to model sensors with a fast response using sensors with a slow response. Based on this analysis, temperature sensors 3 and 9 were selected as to be representative for the Tx and Rx₃ regions, respectively. These sensors are the fastest sensors which can properly model other sensors, and can therefore be used to replace them.

5.2.2. Assessment of Spatial Temperature Variation

Principal component analysis (PCA) was applied to the time series of the selected temperature sensors 3 and 9 and used to identify UTV and NUTV datasets. The first eigenvalues for respective datasets were obtained after PCA. The residual eigenvalues were evaluated by subtracting the first eigenvalues from a maximum value of one ($1 - E_{val,1N}$). The results of plotting the residual eigenvalues for respective datasets is depicted in Figure 5.4.

The red bars in the plot represent datasets recorded with uniform temperature distributions and the blue plots represent datasets recorded with non-uniform temperature distributions. It can be seen that $1 - E_{val,1N}$ ranges from 0.0013 to 0.03. The smallest values are associated with measurements on cloudy days, whereas larger values are associated with sunny days. In the latter case, there was partial shading on the measurement device that moved with time during the calibration measurements.

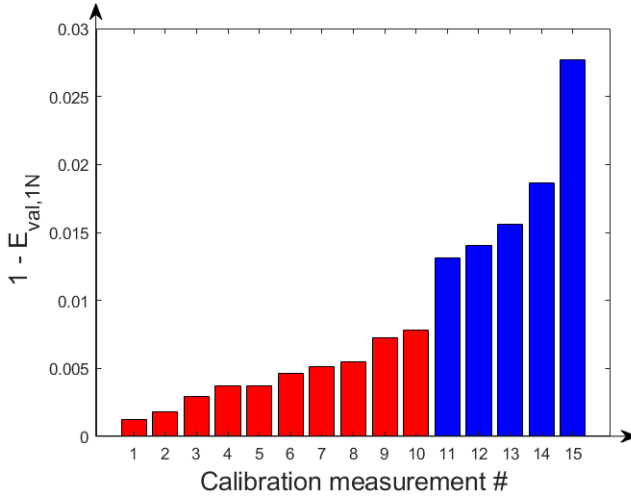


Figure 5.4.: Plot of the first eigenvalue for all datasets obtained from principal component analysis (PCA) on time series of temperature sensors 3 and 9.

It can further be observed from the figure that there is a spring in the eigenvalues between dataset 10 and 11. This is the boundary where a differentiation is made between UTV and NUTV datasets. Based on this, the measurements #1 to #10 were UTV datasets, whereas measurements #11 to #15 were classified as NUTV datasets (Figure 5.4). It should be noted that the PCA method applied here was designed to cover more than two temperatures for future outlooks.

5.2.3. Estimation of Calibration Parameter Boundaries

In order to show the strong dependence between individual calibration parameters, an optimisation (with calibration strategy type A) was done with the correlation test parameter boundaries shown in Table 5.1. The results from evaluating the correlation between the calibration parameters G_1 and G_2 for dataset #10 shows a lot of possible solutions (parameter combinations) where the error is less than 1 mSm^{-1} as shown in Figure 5.5. This is obtained from fitting dataset #10 with the initial boundaries. For a range of $-0.06 \text{ mradK}^{-1} < G_1 < 0.06 \text{ mradK}^{-1}$ and $0 \text{ mradK}^{-1} < G_2 < 0.1 \text{ mradK}^{-1}$, the same minimal fitting errors were obtained. This therefore demonstrates the need to constrain the parameters.

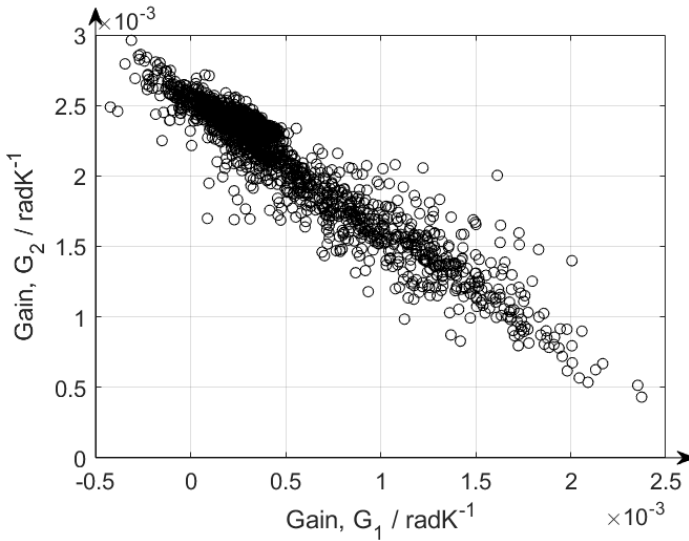


Figure 5.5.: Correlation between the calibration parameters G_1 and G_2 showing all parameter combinations for $RMSE$ values less than 1 mSm^{-1} .

To determine appropriate boundaries for the calibration parameters G and τ , the NUTV datasets were used with a reduced temperature range and a linear drift correction model using a broad feasible parameter space (Table 5.1). After fitting, the minimum and maximum values of G_1 , G_2 , τ_1 , τ_2 were determined and used as the

Table 5.1.: Boundary for the time constant (τ) and gain (G) calibration parameters before and after fitting

Parameters	Bounds	G_1	G_2	τ_1	τ_2	NL_1	NL_2
		(mradK ⁻¹)	(mradK ⁻¹)	(s)	(s)		
Correlation Test	Lower	-0.1	-0.1	0	0	0	0
	Upper	0.1	0.1	4000	4000	2.5	2.5
Initial	Lower	-0.1	-0.1	0	0	1	1
	Upper	0.1	0.1	4000	4000	1	1
Constrained	Lower	-0.06	0.05	0	500	0	0
	Upper	-0.005	0.1	1000	4500	2.5	2.5

new boundaries of the feasible parameter space for the final calibration (Table 5.1). It was found that G_1 is always negative and G_2 is always positive, with an overall sum of 0.033 mradK⁻¹.

5.2.4. Determination of the Representative Calibration Parameters

The reduced feasible parameter space was used to compare the calibration results for calibration strategies A, B and C. The time series variation of measured and modelled ECa for calibration strategy type A as well as the corrected ECa values estimated for the three calibration strategies are depicted in Figure 5.6 and Figure 5.7 respectively. To focus on the changes in ECa rather than absolute values, the ECa values shown in Figure 5.6 were shifted to have a zero mean. The plot in Figure 5.7 shows the root mean square errors ($RMSE$) from fitting with temperature sensors 3 and 9 using calibration strategy types A-C (black, red and blue bars, respectively).

The black bars show the results of drift correction with calibration parameters obtained from fitting individual measurements. The red bars show the correction with the calibration parameters obtained from simultaneously fitting all datasets. The blue bars are the correction results with parameters obtained from simultaneous fitting with one LPF and the mean of temperature sensors 3 and 9. The first 10 datasets on the plot are UTV datasets and the remaining 5 are NUTV datasets. The results for calibration strategy A where all parameters were calibrated individually for each dataset show that this strategy provides the best calibration results. The resulting mean $RMSE$ over all datasets is 0.46 mSm⁻¹.

However, the resulting fitted parameters may not be representative of the entire system drifts because each dataset typically covers a limited temperature range. There is thus a risk that this calibration strategy results in overfitting of the data by ac-

counting for specific peculiarities in each dataset. The results for calibration strategy B which involves simultaneous data fitting with two LPFs showed an overall increase in RMSE values compared to type A.

The outcome of calibration strategy B gave a representative parameter set with a mean error of 0.8 mSm^{-1} over all datasets. The results show that strategy B corrects UTV and NUTV datasets with similar accuracy (Figure 5.7). The results for calibration strategy C which involves simultaneous data fitting using only a single LPF gave a mean error of 2.4 mSm^{-1} . This shows that the drift correction with one LPF provides a lower accuracy in comparison with two. This is particularly visible in the last 3 NUTV datasets (13, 14, 15) where the RMSE values are larger than 4 mSm^{-1} (Figure 5.7) when a single LPF is used.

With regard to the UTV datasets, fitting with one LPF offers less accurate results than expected with a mean error of 1.8 mSm^{-1} . This is also less accurate in comparison to the results in Tazifor et al. [104] (chapter 4) where the mean error is 0.49 mSm^{-1} . This is because the $1 - E_{val,1N}$ values from the first part of this work in chapter 4 are mostly less than 0.0028 across all measurements, which is extremely small in relation to the more complicated datasets in this part. The calibration parameters obtained from the less obvious calibration strategy type B and type C are shown in Table 5.2 (Calibration strategy type A is not shown as it will obviously always offer the best result by default since the parameters obtained from individual measurements are used to correct the same measurements).

It can be seen from the table that when the optimisation is done with calibration strategy type B involving two LPFs, two different gains are obtained, one being negative and the other positive. This implies that the system gains (G_1 and G_2) partly compensate each other, but only if the time constants (τ_1 and τ_2) are equal. However, the table shows different time constants, where LPF_1 has no delay with a corresponding time constant τ_1 of 0.002 s and LPF_2 , has a time constant τ_2 of 1033 s.

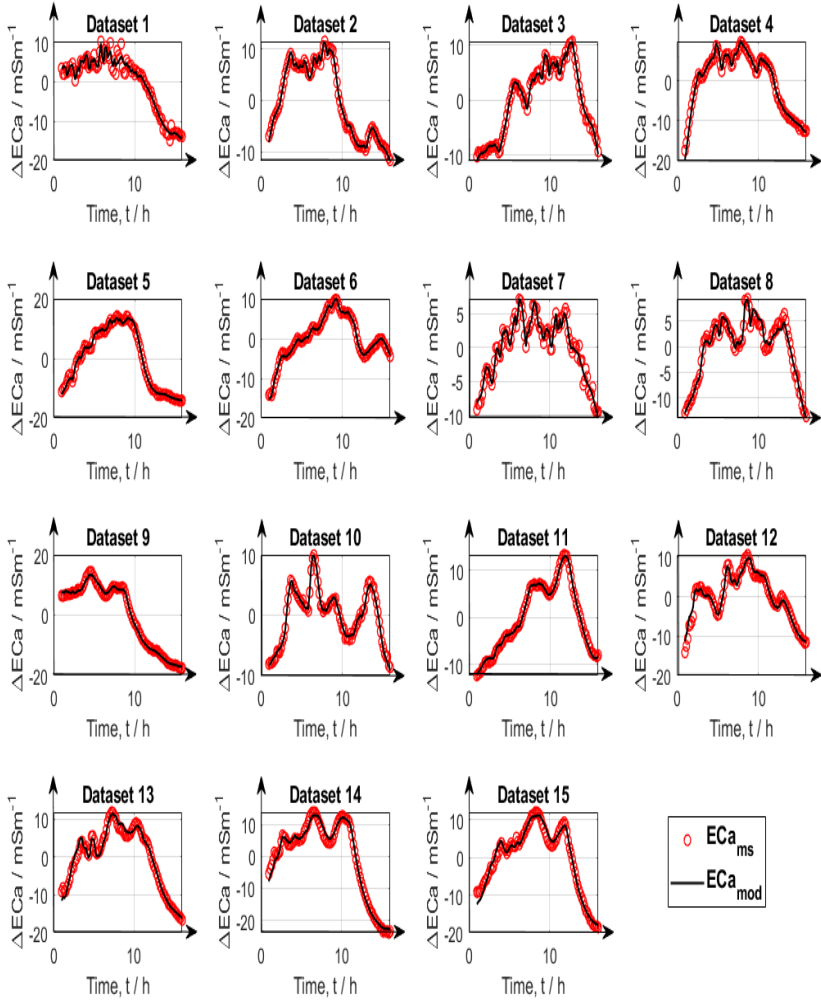


Figure 5.6.: Time series of measured apparent electrical conductivity ($E_{Ca_{ms}}$) and modelled apparent electrical conductivity ($E_{Ca_{mod}}$) for 15 datasets. E_{Ca} values were shifted to have a zero mean.

Furthermore it can be seen the LPF_1 has a strong non-linearity NL with a value of 0.29 whereas the second LPF is linear with a value of 1.02. This shows that it is

important to consider this different gains and time constants when fast temperature changes or non-uniform temperature changes occur. Also, the system's non-linearities must be considered.

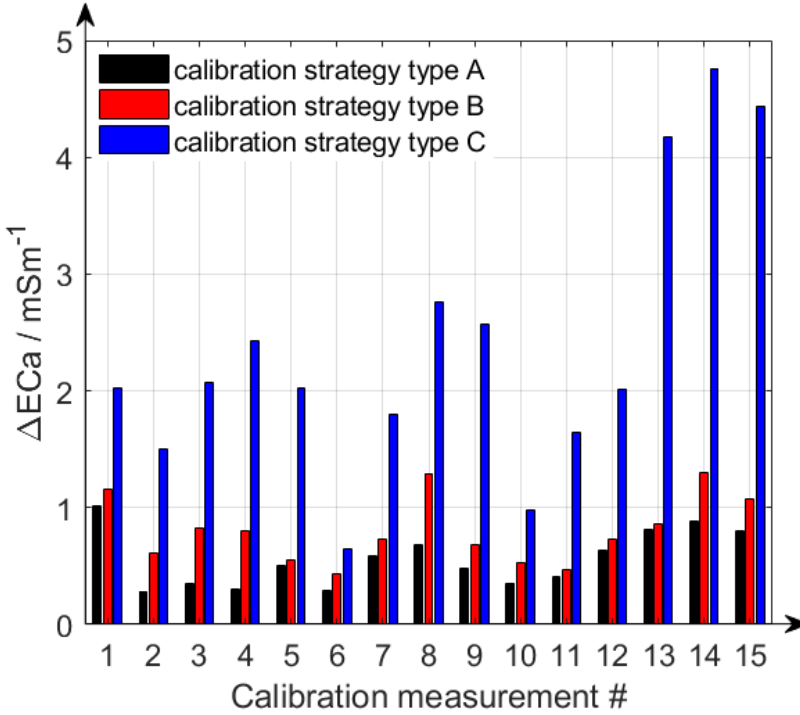


Figure 5.7.: Root mean square errors (RMSE) from fitting with temperature sensors 3 and 9 using calibration strategy types A-C.

For calibration strategy type C, the gain is around the sum of the G_1 and G_2 of calibration type B and NL is 1.48 and the time constant for type C is greater than those in type B. The differences in parameter values between type B and C are likely explained by the fact that the datasets with the large non-uniform temperature distributions can not be properly fitted by calibration type C. The corresponding gains as ECa values for type B were $G_1 = -0.804 \text{ mSm}^{-1}\text{K}^{-1}$, $G_2 = 2.159 \text{ mSm}^{-1}\text{K}^{-1}$ and for type C was $G_1 = 1.7 \text{ mSm}^{-1}\text{K}^{-1}$.

Table 5.2.: Calibration parameters obtained with calibration strategy B and C.

Calibration Strategy	G_1 (mradK ⁻¹)	G_2 (mradK ⁻¹)	τ_1 (s)	τ_2 (s)	NL ₁	NL ₂
Type B	-0.022	0.061	0.002	1033	0.291	1.02
Type C	0.048	-	2057	-	1.48	-

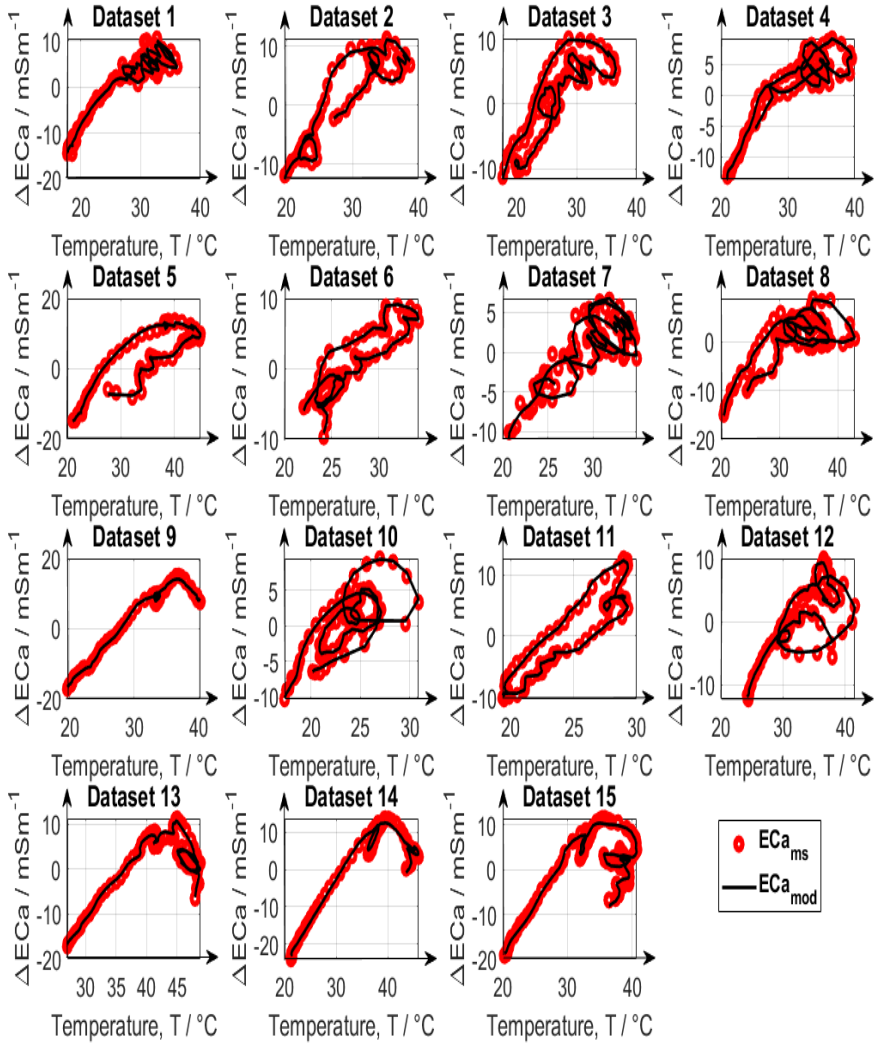


Figure 5.8.: Modelled apparent electrical conductivity and measured apparent electrical conductivity versus the mean of temperatures 3 and 9 for type A. ⁶⁷
 ECa values were shifted to have a zero mean.

Other approaches for temperature drift mitigation rely on the typical static correction methods (without a LPF) where only look-up tables are used to establish unique relationships between temperature and phase. In comparison to these methods, the results in Table 5.2 show a higher fitting accuracy when LPFs are considered, as also confirmed by Tazifor et al. [104] (chapter 4).

In addition to the total error after data correction, the individual measured and modeled data are compared in Figure 5.8, 5.9 and 5.10 for calibration strategies A, B and C, respectively. All ECa values are mean-centered and represented as ECa changes. It is evident that calibration strategy A and B results in accurate fits of the drift model to the measured ECa for datasets with both uniform and non-uniform spatial temperature variations. The hysteresis loops in the relationship between measured ECa values and temperature, which were also reported by Huang et al. [78] and Tazifor et al. [104], are a result of the dynamic heating and cooling history of the system components. They were accurately reproduced by the drift model.

The results obtained from calibration strategy C with only one LPF are shown in Figure 5.10. By comparing the ECa_{mod} values with the ECa_{ms} values, it can be seen that the hysteresis effects were best modelled for data set 6, and that the results are worst for datasets 13, 14 and 15, which are the most complicated NUTV datasets with strong partial shading effects. It is seen clearly here that a drift model with only one LPF can only fit some of the measured data. Overall, the results show that it is possible to correct drift effects resulting from the occurrence of non-uniform temperature variations in measurement systems during EMI data acquisition when two LPFs and two drift-sensitive temperatures are used.

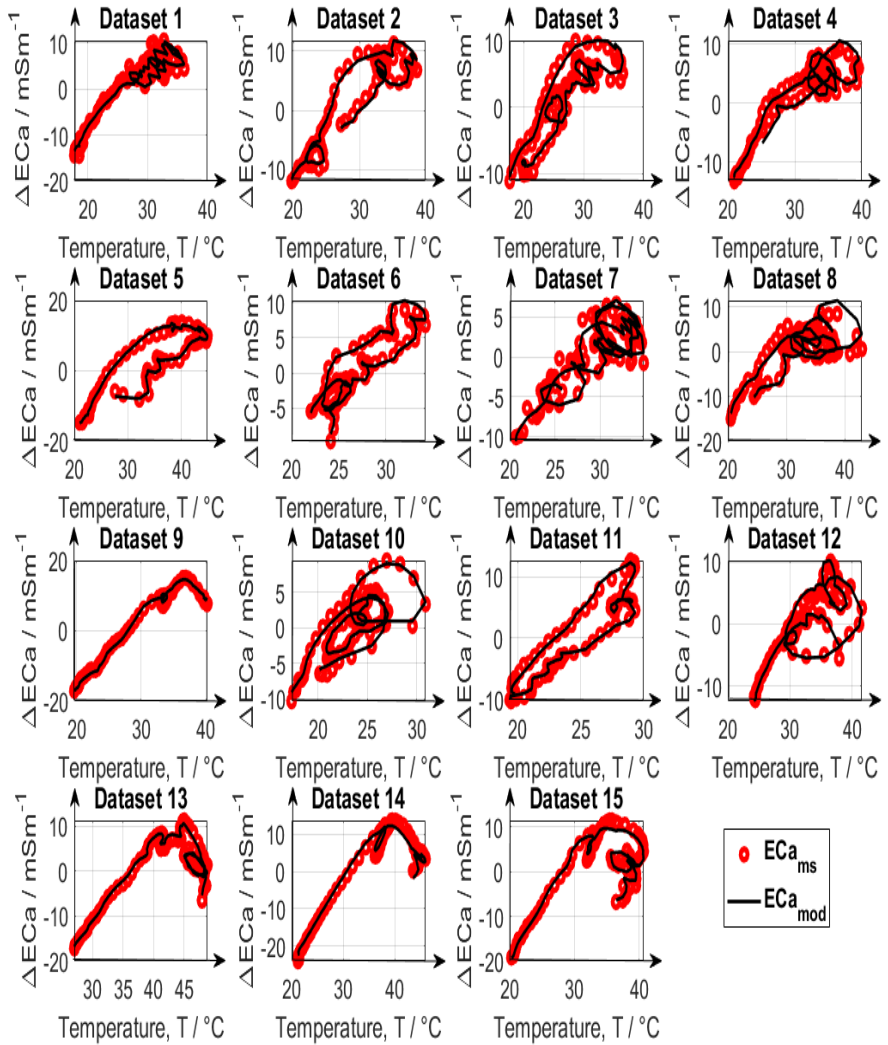


Figure 5.9.: Modelled apparent electrical conductivity and measured apparent electrical conductivity versus the mean of temperatures 3 and 9 for type B. ECa values were shifted to have a zero mean.

In summary advanced dynamic drift correction method was presented that uses

2 low-pass filters (LPF) to model the transient response of electromagnetic induction (EMI) instruments to non-uniform temperature variations. The parameters that control the model are the time constant (τ) from the LPF, the gain (G), and the non-linear variable (NL) of the LuT, as well as the system phase offset (Φ_{offset}). In this study, an EMI instrument was used to perform 15 measurements on different days and at different locations. 8 temperature sensors spread across the device simultaneously measured the ambient internal temperature varying between 10 °C – 50 °C. To develop a drift correction method, it is necessary to place the temperature sensors in the best positions where sources of drift are expected.

The problem here is that the system components have different thermal delays to external ambient temperature change, which leads to the question if localised temperature sensors are required to correct the drifts that arise. This study showed that the fastest reacting sensors can nicely model the thermal delays of the system components with slower reaction times. It is therefore sufficient to place the sensors in air or on other fast reacting components like the PCB where the drifting electronic components are assumed to be. For the EMI system used here, there are two drift-sensitive regions, notably, the transmitter region and the receiver region for an inter-coil spacing of 1.2 m. For these two regions, the temperature sensors 3 and 9 with a quick response were selected.

For a drift model with two or more LPFs, it is difficult to determine calibration parameters through fitting because they are strongly correlated with each other. This creates on the one hand the need for an optimisation method that searches the global minimum. To address this, the shuffled complex evolution (SCE-UA) method was used to estimate optimal calibration parameters. On the other hand, the parameter boundaries must be selected carefully since narrow boundaries may lead to a sub-optimum solution and too wide boundaries may lead to convergence problems and a very large computation time. To address this, an initial optimisation run was performed by individually fitting each dataset in a linear region. Based on these initial runs, relatively narrow boundaries were derived.

Using these constrained boundaries, the correction with parameters from simultaneously fitting all datasets offered satisfactory results with a mean *RMSE* of 0.8 mSm⁻¹ across all datasets, showing that the parameters obtained are characteristic for the system drifts and that the system can be temperature-calibrated. The final calibrated parameters were $G_1 = -0.804$ mSm⁻¹K⁻¹, $G_2 = 2.159$ mSm⁻¹K⁻¹, $\tau_1 = 0$ s and $\tau_2 = 1030$ s, $NL_1 = 0.291$, $NL_2 = 1.02$. Here, it should be noted that both positive and negative gains were obtained, which is particularly problematic for drift correction. For slow uniform temperature changes, the gains compensate each other.

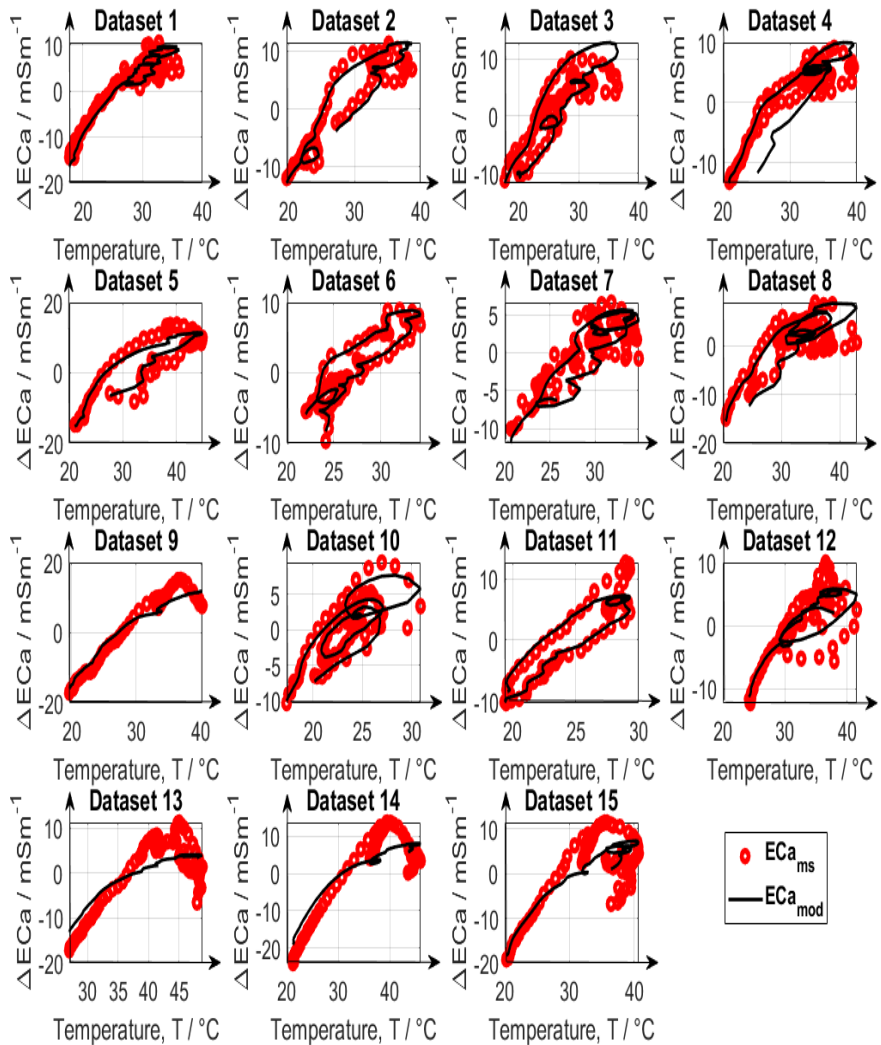


Figure 5.10.: Modelled apparent electrical conductivity and measured apparent electrical conductivity versus the mean of temperatures 3 and 9 for type C. ECa values were shifted to have a zero mean.

However, for fast temperature changes and different time constants, or for non-uniform

temperature changes, the presence of both positive and negative gains results in large drift errors if the two different gains are not considered. This implies that it is very important to estimate these gains. The strong non-linearity of NL_1 shows that a linear model is not sufficient for drift correction, which leads to an increase of dependency between the calibration parameters, so that for each LPF, the NL parameter must also be considered and fitted. The correction with calibration parameters obtained from using only one LPF by simultaneously fitting all datasets showed that the drift correction was generally less accurate than for the case where two LPFs were used. Due to the non-uniformity of the temperature distribution in the device, the drift model needs more than one temperature sensor for the correction.

6. Conclusions and Outlook

The use of EMI systems has become increasingly popular in subsurface electrical conductivity surveys in recent decades. However, studies in the literature have shown that acquiring error-free data using these systems can be challenging. This thesis aims to improve the performance of EMI systems and provide stable and quantitative data for geophysical subsurface investigations. To achieve this goal, two approaches were taken.

The first approach involved investigating the effect of external ambient temperature variations on the internal temperature of the measurement device. It was assumed that a uniform temperature distribution scenario existed. The aim was to understand the impact of these variations on the EMI system's performance and investigate approaches to correct the corresponding drifts. For this, temperature information from 10 sensors spread across 10 locations on the device were used.

The second approach aimed to extend the proposed method to real-life scenarios where the measurement device may have non-uniform internal temperature distributions due to partial shading. The goal of these investigations was two folds: firstly to improve the accuracy of the EMI system's measurements by developing correction methods for the non-uniform internal temperature distribution scenario and secondly to better understand drift effects by determine the fastest temperature sensors in order to know what the best location to place the temperature sensors is. Detailed investigations were carried out, including theoretical analyses, developments of drift correction and calibration methods, and corresponding synthetic model simulations.

6.1. Uniform Temperature Distributions

The results presented in this part demonstrated that the novel model-based dynamic drift correction method using LPF is significantly more accurate than static correction, providing up to four times higher accuracy in drift correction. This approach has proven to be reliable in mitigating temperature drift effects in EMI data, even when there are rapid temperature changes occurring during typical field measurements. Furthermore, the model-based calibration method presented in this part of the study no longer necessitates stable temperature levels, as is the norm for calibration in thermostatically controlled rooms. This makes the calibration process more practical and efficient in field settings, where it can be challenging to maintain stable temperature conditions.

The new correction method requires minimal effort to implement. For calibration, outdoor measurements with sufficient temperature time series ranges are more than enough. Commercial EMI systems can benefit from this novel correction method with the help of manufacturers. In this case, the correction method can be easily applied by installing temperature sensors on the instruments and using the dynamic correction method to improve the accuracy of temperature related drift correction in EMI systems compared to standard static correction. This correction method is relevant in several agricultural settings that require near surface ECa measurements.

6.2. Non-uniform Temperature Distributions

In this part of the thesis, it could be shown for data with extreme non-uniform temperature variations that the ECa error after drift correction with one LPF was very large (4.5 mSm^{-1}). This situation typically arises when partial shading is experienced during measurements. In order to recognize these situations, it is useful to evaluate the uniformity of temperature variation with principal component analysis (PCA). It is of course also possible that at least two dominant temperature components are present in the system with different time constants τ and non-linearities NL , which can not be modelled with only one LPF.

In summary, the dynamic drift correction model with two LPFs provides a reliable solution for removing the effects of temperature related drifts in a wide range of applications involving near-surface EMI systems. This dynamic correction approach can be subsequently extended to commercial devices by integrating the required temperature sensors, since air temperature sensors are sufficient for the proposed correction method. These sensors can be easily integrated through holes on the devices' surface. In view of our modular and scalable EMI system under development, only air temperature sensors will be considered for the development.

A simple method to calibrate the EMI devices is to perform outdoor measurements. The drift of individual electrical components can be measured in temperature chambers by manufacturers. This however does not hold true for the coils and for the entire system since such measurements need a metal-free and low noise environment. Typically, laboratories are not adequate for this. Contrary to the measurement of the drift of single components, the proposed approach is intended to consider the device as an integral drifting system. By incorporating temperature sensors into the instruments and using the new drift correction technique, it is possible to enhance the precision of temperature related drift correction in EMI systems beyond the level achievable with traditionally used correction techniques. The new method has potential applications in various agricultural scenarios where accurate near-surface ECa measurements are required.

6.3. Outlook

The thesis began with the identification of various major objectives, which were successfully achieved. However, there were limitations encountered during the course of the research. Hence, this section presents potential future directions for further development. One of the significant accomplishments of this study was the dynamic drift correction approach presented. This approach paves the way for the construction of a novel EMI system that can provide quantitative ECa measurements by correcting for temperature variations.

Chapter 4 of the thesis explains the drift model, which involved using several temperature sensors placed randomly on various components. Chapter 5 highlights the reduction of sensors by identifying the best drift-sensitive locations. In future modular EMI systems, it is crucial to apply this methodology by placing sensors at the identified sender and receiver regions in each module to improve the system's drift performance.

In addition, using two temperature sensors to separately monitor the transmitter and receiver regions provides a more flexible EMI system compared to the conventional rigid-boom EMI system. The use of modular tubes in this system increases transportation efficiency but also creates different thermal conditions that can be monitored. Considering the accuracy of drift correction achieved with the custom rigid-boom EMI system, the application of this novel method to modular EMI systems has significant potential for quantitative geophysical and agricultural applications. To improve the accuracy and reliability of the modular EMI system, further research is required, particularly in real-world scenarios like the towing behind tractors for fast mapping. It is essential to test this new correction method on such modular systems. Addressing these limitations will allow the creation of an EMI system that can provide reliable data for subsurface investigations.

Bibliography

- [1] Corwin D. L. and Rhoades J. D. “Establishing soil electrical conductivity - Depth relations from electromagnetic induction measurements”. In: *Communications in Soil Science and Plant Analysis* 21.11-12 (1990), pp. 861–901. DOI: 10.1080/00103629009368275.
- [2] Nimmo J. R. “Vadose Water”. In: 2009, pp. 766–777. ISBN: 9780123706263. DOI: 10.1016/B978-012370626-3.00014-4.
- [3] Wightman W. E., Jalinoos F., Sirles P., and Hanna K. “Application of Geophysical Methods to Highway Related Problems”. In: 2004.
- [4] Campbell S., Briggs M., Roy S., Douglas T., and Saari S. “Ground-penetrating radar, electromagnetic induction, terrain, and vegetation observations coupled with machine learning to map permafrost distribution at Twelvemile Lake, Alaska”. In: *Permafrost and Periglacial Processes* 32.3 (2021), pp. 407–426. DOI: 10.1002/ppp.2100.
- [5] Won I. J., Keiswetter D. A., Fields G. R. A., and Sutton L. C. “GEM-2: A New Multifrequency Electromagnetic Sensor”. In: *Journal of Environmental and Engineering Geophysics* 1.2 (1996), pp. 129–137. DOI: 10.4133/JEEG1.2.129.
- [6] Adamchuk V., Hummel J. W., M. Morgan, and Upadhyaya S. K. “On-the-go soil sensors for precision agriculture”. In: *Computers and Electronics in Agriculture* 44.1 (2004), pp. 71–91. ISSN: 0168-1699. DOI: 10.1016/j.compag.2004.03.002.
- [7] Won I. J., Oren A., and Funak F. “GEM2A: A programmable broadband helicopter-towed electromagnetic sensor”. In: *Geophysics* 68.6 (2003), pp. 1888–1895. DOI: 10.1190/1.1635041.
- [8] Heil K. and Schmidhalter U. “Theory and Guidelines for the Application of the Geophysical Sensor EM38”. In: *Sensors* 19.19 (2019). ISSN: 1424-8220. DOI: 10.3390/s19194293.
- [9] Daly E. and Porporato A. “A Review of Soil Moisture Dynamics: From Rainfall Infiltration to Ecosystem Response”. In: *Environmental Engineering Science* 22.1 (2005), pp. 9–24. DOI: 10.1089/ees.2005.22.9.
- [10] Lesch S. M., Strauss D. J., and Rhoades J. D. “Spatial Prediction of Soil Salinity Using Electromagnetic Induction Techniques: 2. An Efficient Spatial Sampling Algorithm Suitable for Multiple Linear Regression Model Identification and Estimation”. In: *Water Resources Research* 31.2 (1995), pp. 387–398. DOI: 10.1029/94WR02180.

- [11] Akbar M. A., Kenimer A. L., Searcy S., and Torbert H. A. "Soil Water Estimation Using Electromagnetic Induction". In: *American Society of Agricultural Engineers* 48.1 (2005), 129135. ISSN: 00012351. DOI: 10.13031/2013.17955.
- [12] Corwin D. L., Lesch S., Segal E., Skaggs T., and Bradford S. "Comparison of Sampling Strategies for Characterizing Spatial Variability with Apparent Soil Electrical Conductivity Directed Soil Sampling". In: *Journal of Environmental Engineering Geophysics* 15.3 (2010), pp. 147–162. DOI: 10.2113/JEEG15.3.147.
- [13] Allred B., Ehsani M. R., and Daniels J. J. "General considerations for geophysical methods applied to agriculture". In: *Handbook of Agricultural Geophysics (1st ed.)* CRC Press, 2008, pp. 3–16.
- [14] Samouélian A., Cousin I., Tabbagh A., Bruand A., and Richard G. "Electrical resistivity survey in soil science: a review". In: *Soil and Tillage Research* 83.2 (2005), pp. 173–193. ISSN: 0167-1987. DOI: 10.1016/j.still.2004.10.004.
- [15] Corwin D. L. "Past, present, and future trends of soil electrical conductivity measurement using geophysical methods". In: *Handbook of Agricultural Geophysics (1st ed.)* CRC Press, 2008, pp. 17–44. DOI: 10.1201/9781420019353.
- [16] Rhoades J. D., Chanduvi F., and Lesch S. M. "Soil salinity assessment: methods and interpretation of electrical conductivity measurements". In: 1999.
- [17] Topp J. C. and Davis J. L. "Detecting infiltration of water through soil cracks by time-domain reflectometry". In: *Geoderma* 26.1 (1981), pp. 13–23. ISSN: 0016-7061. DOI: 10.1016/0016-7061(81)90073-2.
- [18] Topp J. C., Zebchuk W. D., Davis J. L., and Bailey W. G. "The Measurement of soil water content using a portable TDR hand probe". In: *Canadian Journal of Soil Science* 64.3 (1984), pp. 313–321. DOI: 10.4141/cjss84-033.
- [19] Kachanoski R. G., Gregorich E. G., and van Wesenbeeck I. "Estimating Spatial Variations of Soil Water Content Using Noncontacting Electromagnetic Induction Methods". In: *Canadian Journal of Soil Science* 68 (1988), pp. 715–722. DOI: 10.4141/cjss88-069.
- [20] Vanderborght J., Huisman J. A., van der Kruk J., and Vereecken H. "Geophysical Methods for Field-Scale Imaging of Root Zone Properties and Processes". In: *Soil–Water–Root Processes: Advances in Tomography and Imaging*. John Wiley Sons, Ltd, 2013. Chap. 12, pp. 247–282. ISBN: 9780891189596. DOI: 10.2136/sssaspecpub61.c12.
- [21] Guinea A., Playa E., Rivero L., and Himi M. "Electrical resistivity tomography and induced polarization techniques applied to the identification of gypsum rocks". In: *Near Surface Geophysics* 8 (2010). DOI: 10.3997/1873-0604.2010009.

- [22] Herring T., Heagy L. J., Pidlisecky A., and Cey E. “Hybrid parametric/smooth inversion of electrical resistivity tomography data”. In: *Computers Geosciences* 159 (2022), p. 104986. ISSN: 0098-3004. DOI: 10.1016/j.cageo.2021.104986.
- [23] Robinson D. A., Gardner C. M., Evans J., Cooper J. D., Hodnett M. G., and Bell J. P. “The dielectric calibration of capacitance probes for soil hydrology using an oscillation frequency response model”. In: *Hydrology and Earth Systems Science* 2.1 (1998), pp. 111–120. DOI: 10.5194/hess-2-111-1998.
- [24] Fares A. and Kumar A. “Soil Water Components Based on Capacitance Probes in a Sandy Soil”. In: *Soil Science Society of America Journal* 64 (2000), pp. 311–318. DOI: 10.2136/sssaj2000.641311x.
- [25] Cassiani G., Kemna A., Villa A., and Zimmermann E. “Spectral induced polarization for the characterization of free-phase hydrocarbon contamination of sediments with low clay content”. In: *Near Surface Geophysics* 7.5-6 (2009), pp. 547–562. DOI: 10.3997/1873-0604.2009028.
- [26] Gao Z., Haegel F.-H., Esser O., Zimmermann E., Vereecken H., and Huisman J. A. “Spectral Induced Polarization of Biochar in Variably Saturated Soil”. In: *Vadose Zone Journal* 18.1 (2019), p. 180213. DOI: 10.2136/vzj2018.12.0213.
- [27] Kurniawan A. “Evaluation on the Cathodic Protection Inspection Methods for Underground Pipeline”. In: 2014.
- [28] Robinson D. A., Binley A., Crook N., Day-Lewis F., Ferré T., Grauch V. J. S., Knight R., Knoll M., Lakshmi V., Miller R., Nyquist J., Pellerin L., Singha K., and Slater L. “Advancing process-based watershed hydrological research using near-surface geophysics: A vision for, and review of, electrical and magnetic geophysical methods”. In: *Hydrological Processes* 22.18 (2008), pp. 3604–3635. DOI: 10.1002/hyp.6963.
- [29] Mirza A. F., See C. H., Danjuma I. M., Asif R., Abd-Alhameed R. A., Noras J. M., Clarke R. W., and Excell P. S. “An Active Microwave Sensor for Near Field Imaging”. In: *IEEE Sensors Journal* 17.9 (2017), pp. 2749–2757. DOI: 10.1109/JSEN.2017.2673961.
- [30] Gupta V. K. and Jangid R. A. “Roughness effect of the soil of Alwar on passive and active microwave remote sensing”. In: *2008 International Conference on Recent Advances in Microwave Theory and Applications*. 2008, pp. 207–210. DOI: 10.1109/AMTA.2008.4763002.
- [31] Kumar S. V., Holmes T. R., Bindlish R., de Jeu R., and Peters-Lidard C. “Assimilation of vegetation optical depth retrievals from passive microwave radiometry”. In: *Hydrology and Earth System Sciences* 24.7 (2020), pp. 3431–3450. DOI: 10.5194/hess-24-3431-2020.
- [32] Gao H. R., Zhang Z. J., Zhang W. C., Chen H., and Xi M. J. “Spatial Down-scaling Based on Spectrum Analysis for Soil Freeze/Thaw Status Retrieved From Passive Microwave”. In: *IEEE Transactions on Geoscience and Remote Sensing* 60 (2022), pp. 1–11. DOI: 10.1109/TGRS.2021.3051683.

- [33] Shock C., Pereira A., Feibert E., Shock C., Akin A., and Unlenen L. “Field Comparison of Soil Moisture Sensing Using Neutron Thermalization, Frequency Domain, Tensiometer, and Granular Matrix Sensor Devices: Relevance to Precision Irrigation”. In: *Journal of Water Resource and Protection* 8.2 (2016), pp. 154–167. DOI: 10.4236/jwarp.2016.82013.
- [34] Evett S. R. “Soil Water Measurement by Neutron Thermalization”. In: *Encyclopedia of Water Science*. Marcel Dekker, Inc. (2003).
- [35] Hinedi Z. R., Kabala Z. J., Skaggs T. H., Borchardt D. B., Lee R. W. K., and Chang A. C. “Probing Soil And Aquifer Material Porosity With Nuclear-Magnetic-Resonance”. In: *Water Resources Research* 29.12 (1993), pp. 3861–3866. DOI: 10.1029/93WR02302.
- [36] Bevan B. and Kenyon J. “Ground-penetrating radar for historical archaeology”. In: *MASCA Newsletter (Museum Applied Science Center for Archaeology)* 11.2 (1975), pp. 2–7.
- [37] Huisman J. A. and Bouten W. “Accuracy and Reproducibility of Mapping Surface Soil Water Content with the Ground Wave of Ground-Penetrating Radar”. In: *Journal of Environmental & Engineering Geophysics* 8.2 (2003), pp. 67–75. DOI: 10.4133/JEEG8.2.67.
- [38] Galagedara L., Parkin G. W., Redman J. D., von Bertoldi A., and Endres A. “Field studies of the GPR ground wave method for estimating soil water content during irrigation and drainage”. In: *Journal of Hydrology* 301.1-4 (2005), pp. 182–197. ISSN: 0022-1694. DOI: 10.1016/j.jhydro1.2004.06.031.
- [39] Doolittle J. A., Dobos R., Peaslee S., Waltman S., Benham E., and Tuttle W. “Revised ground-penetrating radar soil suitability maps”. In: *Journal of Environmental & Engineering Geophysics* 15.3 (2010), pp. 111–118. ISSN: 1083-1363. DOI: 10.2113/JEEG15.3.111.
- [40] Newman G. A., Hohmann G. W., and Anderson W. L. “Transient electromagnetic response of a Three-Dimensional body in a layered earth”. In: *GEO-PHYSICS* 51.8 (1986), pp. 1608–1627. DOI: 10.1190/1.1442212.
- [41] McNeill J. D. “Electromagnetic Terrain Conductivity Measurement at Low Induction Numbers”. In: *Geonics Limited, Technical Note TN-6, Mississauga* 6 (1980).
- [42] Sørensen K. I. and Auken E. “SkyTEM—a New High-resolution Helicopter Transient Electromagnetic System”. In: *Exploration Geophysics* 35.3 (2004), pp. 194–202. DOI: 10.1071/EG04194.
- [43] Wait J. R. “Induction by a horizontal oscillating magnetic dipole over a conducting homogeneous Earth”. In: *Eos, Transactions American Geophysical Union* 34.2 (1953), pp. 185–188. DOI: 10.1029/TR034i002p00185.

- [44] Robinson D. A., Lebron I., Kocar B., Phan K., Sampson M., Crook N., and Fendorf S. “Time-lapse geophysical imaging of soil moisture dynamics in tropical deltaic soils: An aid to interpreting hydrological and geochemical processes”. In: *Water Resources Research* 45.4 (2009). DOI: 10.1029/2008WR006984.
- [45] Corwin D. L. and Lesch S. M. “Application of Soil Electrical Conductivity Measurements in Agriculture”. In: *Computers and Electronics in Agriculture* 46 (2005), pp. 11–43. DOI: 10.1016/j.compag.2004.10.005.
- [46] Schmäck J., Weihermüller L., Klotzsche A., von Hebel C., Pätzold S., Welp G., and Vereecken H. “Large-scale detection and quantification of harmful soil compaction in a post-mining landscape using multi-configuration electromagnetic induction”. In: *Soil Use and Management* 38.1 (2022), pp. 212–228. DOI: 10.1111/sum.12763.
- [47] Gebbers R., Lück E., Dabas M., and Domsch H. “Comparison of instruments for geoelectrical soil mapping at the field scale”. In: *Near Surface Geophysics* 7.3 (2009), pp. 179–190. DOI: 10.3997/1873-0604.2009011.
- [48] Corwin D. L. and Lesch S. M. “Application of Soil Electrical Conductivity to Precision Agriculture”. In: *Agronomy Journal* 95.3 (2003), pp. 455–471. DOI: 10.2134/agronj2003.4550.
- [49] Doolittle J. A. and Brevik E. C. “The use of electromagnetic induction techniques in soils studies”. In: *Geoderma* 223-225 (2014), pp. 33–45. ISSN: 0016-7061. DOI: <https://doi.org/10.1016/j.geoderma.2014.01.027>.
- [50] Visconti F. and De Paz J. M. “A semi-empirical model to predict the EM38 electromagnetic induction measurements of soils from basic ground properties”. In: *European Journal of Soil Science* 72.2 (2021), pp. 720–738. DOI: 10.1111/ejss.13044.
- [51] Cameron D. R., Dejong E., Read D., and Oosterveld M. “Mapping salinity using resistivity and electromagnetic inductive techniques”. In: *Canadian Journal of Soil Science* 61 (1981), pp. 67–78. DOI: 10.4141/cjss81-008.
- [52] Visconti F. and De Paz J. M. “Field Comparison of Electrical Resistance, Electromagnetic Induction, and Frequency Domain Reflectometry for Soil Salinity Appraisal”. In: *Soil Systems* 4.4 (2020). ISSN: 2571-8789.
- [53] Corwin D. L. and Rhoades J. D. “Measurement of Inverted Electrical Conductivity Profiles Using Electromagnetic Induction”. In: *Soil Science Society of America Journal* 48.2 (1984), pp. 288–291. DOI: <https://doi.org/10.2136/sssaj1984.03615995004800020011x>.
- [54] Badewa E., Unc A., Cheema M., Kavanagh V., and Galagedara L. “Soil Moisture Mapping Using Multi-Frequency and Multi-Coil Electromagnetic Induction Sensors on Managed Podzols”. In: *Agronomy* 8.10 (2018). ISSN: 2073-4395. DOI: 10.3390/agronomy8100224.

- [55] Boaga J. “The use of FDEM in hydrogeophysics: A review”. In: *Journal of Applied Geophysics* 139 (2017), pp. 36–46. ISSN: 0926-9851. DOI: 10.1016/j.jappgeo.2017.02.011.
- [56] Altdorff D., Galagedara L., Nadeem M., Cheema M., and Unc A. “Effect of agronomic treatments on the accuracy of soil moisture mapping by electromagnetic induction”. In: *CATENA* 164 (2018), pp. 96–106. ISSN: 0341-8162. DOI: 10.1016/j.catena.2017.12.036.
- [57] van’t Veen K. M., Ferré T. P. A., Iversen B. V., and Børgesen C. D. “Using machine learning to predict optimal electromagnetic induction instrument configurations for characterizing the shallow subsurface”. In: *Hydrology and Earth System Sciences* 26.1 (2022), pp. 55–70. DOI: 10.5194/hess-26-55-2022.
- [58] Weller U., Zipprich M., Sommer M., Castell W. Z., and Wehrhan M. “Mapping Clay Content across Boundaries at the Landscape Scale with Electromagnetic Induction”. In: *Soil Science Society of America Journal* 71.6 (2007), pp. 1740–1747. DOI: 10.2136/sssaj2006.0177.
- [59] Guillemoteau J., Simon F-X., Lück E., and Tronicke J. “1D sequential inversion of portable multi-configuration electromagnetic induction data”. In: *Near Surface Geophysics* 14.5 (2016), pp. 423–432. DOI: 10.3997/1873-0604.2016029.
- [60] Rhoades J. D. and Corwin D. L. “Determining Soil Electrical Conductivity-Depth Relations Using an Inductive Electromagnetic Soil Conductivity Meter”. In: *Soil Science Society of America Journal* 45.2 (1981), pp. 255–260. DOI: 10.2136/sssaj1981.03615995004500020006x.
- [61] De Smedt P., Delefortrie S., and Wyffels F. “Identifying and removing micro-drift in ground-based electromagnetic induction data”. In: *Journal of Applied Geophysics* 131 (2016), pp. 14–22. ISSN: 0926-9851. DOI: 10.1016/j.jappgeo.2016.05.004.
- [62] Altdorff D., Sadatcharam K., Unc A., Krishnapillai M., and Galagedara L. “Comparison of Multi-Frequency and Multi-Coil Electromagnetic Induction (EMI) for Mapping Properties in Shallow Podsolc Soils”. In: *Sensors* 20.8 (2020). ISSN: 1424-8220. DOI: 10.3390/s20082330.
- [63] Saey T., De Smedt P., Islam M. M., Meerschman E., Van De Vijver E., Lehouck A., and Meirvenne M. “Depth slicing of multi-receiver EMI measurements to enhance the delineation of contrasting subsoil features”. In: *Geoderma* 189-190 (2012), pp. 514–521. ISSN: 0016-7061. DOI: 10.1016/j.geoderma.2012.06.010.
- [64] Allred B., Ehsani M. R., and Saraswat D. “The impact of temperature and shallow hydrologic conditions on the magnitude and spatial pattern consistency of electromagnetic induction measured soil electrical conductivity”. In: *Transactions of the ASAE* 48 (6 2005), pp. 2123–2135. DOI: 10.13031/2013.20098.

- [65] Mester A., van der Kruk J., Zimmermann E., and Vereecken H. “Quantitative Two-Layer Conductivity Inversion of Multi-Configuration Electromagnetic Induction Measurements”. In: *Vadose Zone Journal* 10.4 (2011), pp. 1319–1330. DOI: 10.2136/vzj2011.0035.
- [66] Geonics Limited-Geophysical. *Short guide for electromagnetic conductivity mapping and tomography*. <http://www.geonics.com/html/conductivitymeters.html>. Accessed: 2023-8-4.
- [67] GF Instruments. *Profiler manual*. <http://www.gfinstruments.cz/>. Accessed: 2023-8-4.
- [68] GSSI Inc. *Ground penetrating radar (GPR) equipment*. en. <http://www.geophysical.com/>. Accessed: 2023-8-4. Sept. 2017.
- [69] Dualem Inc. *Dualem EM Equipment*. en. <http://www.dualem.com>. Accessed: 2023-8-4. July 2019.
- [70] Abdu H., Robinson D. A., Seyfried M., and Jones S. B. “Geophysical imaging of watershed subsurface patterns and prediction of soil texture and water holding capacity”. In: *Water Resource Research* 44.4 (2008). DOI: 10.1029/2008WR007043.
- [71] Lück E., Gebbers R., Joerg R., and Spangenberg U. “Electrical conductivity mapping for precision farming”. In: *Near Surface Geophysics* 7.1 (2009), pp. 15–26. DOI: 10.3997/1873-0604.2008031.
- [72] Moghadas D., André F., Bradford J. H., van der Kruk J., Vereecken H., and Lambot S. “Electromagnetic induction antenna modelling using a linear system of complex antenna transfer functions”. In: *Near Surface Geophysics* 10.3 (2012), pp. 237–247. DOI: 10.3997/1873-0604.2012002.
- [73] Minsley B. J., Smith B. D., Hammack R., Sams J. I., and Veloski G. “Calibration and filtering strategies for frequency domain electromagnetic data”. In: *Journal of Applied Geophysics* 80 (2012), pp. 56–66. ISSN: 0926-9851. DOI: 10.1016/j.jappgeo.2012.01.008.
- [74] Sudduth K., Drummond S.T., and Kitchen N. “Accuracy issues in electromagnetic induction sensing of soil electrical conductivity for precision agriculture”. In: *Computers and Electronics in Agriculture* 31.3 (2001), pp. 239–264. ISSN: 0168-1699. DOI: 10.1016/S0168-1699(00)00185-X.
- [75] Nüsch A-K., Dietrich P., Werban U., and Behrens T. “Acquisition and reliability of geophysical data in soil science”. In: 2010.
- [76] Robinson D. A., Lebron I., Lesch S. M., and Shouse P. “Minimizing Drift in Electrical Conductivity Measurements in High Temperature Environments using the EM-38”. In: *Soil Science Society of America Journal* 68.2 (2004), pp. 339–345. DOI: 10.2136/sssaj2004.3390.

- [77] Delefortrie S., De Smedt P., Saey T., Van De Vijver E., and Meirvenne M. “An efficient calibration procedure for correction of drift in EMI survey data”. In: *Journal of Applied Geophysics* 110 (2014), pp. 115–125. ISSN: 0926-9851. DOI: 10.1016/j.jappgeo.2014.09.004.
- [78] Huang J., Minasny B., Whelan B. M., Mcbratney A. B., and Triantafyllis J. “Temperature-dependent hysteresis effects on EM induction instruments: An example of single-frequency multi-coil array instruments”. In: *Computers and Electronics in Agriculture* 132 (2017), pp. 76–85. ISSN: 0168-1699. DOI: 10.1016/j.compag.2016.11.013.
- [79] Abdu H., Robinson D. A., and Jones S. B. “Comparing Bulk Soil Electrical Conductivity Determination Using the DUALEM-1S and EM38-DD Electromagnetic Induction Instruments”. In: *Soil Science Society of America Journal* 71.1 (2007), pp. 189–196. DOI: 10.2136/sssaj2005.0394.
- [80] Hanssens D., Van De Vijver E., Waegeman W., Everett M., Moffat I., Sarris A., and De Smedt P. “Ambient temperature and relative humidity-based drift correction in frequency domain electromagnetics using machine learning”. In: *Near Surface Geophysics* 19.5 (2021), pp. 541–556. DOI: 10.1002/nsg.12160.
- [81] Mester A., Zimmermann E., van der Kruk J., Vereecken H., and van Waasen S. “Development and drift-analysis of a modular electromagnetic induction system for shallow ground conductivity measurements”. In: *Measurement Science and Technology* 25.5 (Apr. 2014), p. 055801. DOI: 10.1088/0957-0233/25/5/055801.
- [82] Tan X. “Development of Electromagnetic Induction Measurement and Inversion Methods for Soil Electrical Conductivity Investigations”. unpublished thesis. PhD thesis. RWTH Aachen, 2019.
- [83] Knödel K., Krummel H., and Lange G. *Handbuch zur Erkundung des Untergrundes von Deponien und Altlasten*. Vol. 3. New York: Springer, 2005. DOI: 10.1007/978-3-642-58852-5.
- [84] Bonsall J., Fry R., Gaffney C., Armit I., Beck A., and Gaffney V. “Assessment of the CMD Mini-Explorer, a New Low-frequency Multi-coil Electromagnetic Device, for Archaeological Investigations”. In: *Archaeological Prospection* 20.3 (2013), pp. 219–231. DOI: 10.1002/arp.1458.
- [85] Nelder J. A. and Mead R. A. “A Simplex Method for Function Minimization”. In: *The Computer Journal* 7.4 (Jan. 1965), pp. 308–313. ISSN: 0010-4620. DOI: 10.1093/comjnl/7.4.308.
- [86] Lagarias J. C., Reeds J. A., Wright M. H., and Wright P. E. “Convergence Properties of the Nelder-Mead Simplex Algorithm in Low Dimensions”. In: *Society for Industrial and Applied Mathematics* 9.1 (1998), pp. 112–147.
- [87] Gao F. and Han L. “Implementing the Nelder-Mead simplex algorithm with adaptive parameters”. In: *Computational Optimization and Applications* 51 (2012), pp. 259–277. DOI: 10.1007/s10589-010-9329-3.

- [88] Duan Q., Sorooshian S., and Gupta V. K. “Effective and Efficient Global Optimization for Conceptual Rainfall-Runoff Models”. In: *Water Resources Research* 28.4 (1992), pp. 1015–1031. DOI: 10.1029/91WR02985.
- [89] von Hebel C., Matveeva M., Verweij E., Rademske P., Kaufmann M. S., Brogi C., Vereecken H., Rascher U., and van der Kruk J. “Understanding Soil and Plant Interaction by Combining Ground-Based Quantitative Electromagnetic Induction and Airborne Hyperspectral Data”. In: *Geophysical Research Letters* 45.15 (2018), pp. 7571–7579. DOI: 10.1029/2018GL078658.
- [90] Mangel A. R., Moysey S. M. J., and van der Kruk J. “Resolving Infiltration-Induced Water Content Profiles by Inversion of Dispersive Ground-Penetrating Radar Data”. In: *Vadose Zone Journal* 16.10 (2017), vzt2017.02.0037. DOI: 10.2136/vzj2017.02.0037.
- [91] Liu T., Klotzsche A., Pondkule M., Vereecken H., Su Y., and van der Kruk J. “Radius estimation of subsurface cylindrical objects from ground-penetrating-radar data using full-waveform inversion”. In: *GEOPHYSICS* 83.6 (2018), H43–H54. DOI: 10.1190/geo2017-0815.1.
- [92] Busch S., Weihermüller L., Huisman J. A., Steelman C. M., Endres A. L., Vereecken H., and van der Kruk J. “Coupled hydrogeophysical inversion of time-lapse surface GPR data to estimate hydraulic properties of a layered subsurface”. In: *Water Resources Research* 49.12 (2013), pp. 8480–8494. DOI: 10.1002/2013WR013992.
- [93] Duan Q. and Gupta V. K. “Shuffled complex evolution approach for effective and efficient global minimization”. In: *Journal of Optimization Theory and Applications* 76 (3 1993), pp. 501–521. DOI: 10.1007/BF00939380.
- [94] Isermann R. and Münchhof M. “Identification of Dynamic Systems”. In: Springer, 2010. ISBN: 978-3-540-78879-9. DOI: 10.1007/978-3-540-78879-9.
- [95] Rorabaugh B. C. “Digital filter designer’s handbook: featuring C routines book and disc (electronic design construction)”. In: Tab Books, 1993. ISBN: 9780830644315.
- [96] Tan L. and Jiang J. “Chapter 8 - Infinite Impulse Response Filter Design”. In: *Digital Signal Processing: Fundamentals and Applications*. 2013, pp. 301–403. ISBN: 9780124158931. DOI: 10.1016/B978-0-12-415893-1.00008-1.
- [97] Heiniger R. W., McBride R. G., and Clay D. E. “Using Soil Electrical Conductivity to Improve Nutrient Management”. In: *Agronomy Journal* 95 (2003), pp. 508–519. DOI: 10.2134/agronj2003.5080.
- [98] De Caires S. A., Wuddivira M. N., and Bekele I. “Spatial analysis for management zone delineation in a humid tropic cocoa plantation”. In: *Precision Agriculture* 16 (2015), pp. 129–147. DOI: 10.1007/s11119-014-9366-5.

- [99] Jolliffe I. T. “PRINCIPAL COMPONENT ANALYSIS: A BEGINNER’S GUIDE — I. Introduction and application”. In: *Weather* 45.10 (1990), pp. 375–382. DOI: 10.1002/j.1477-8696.1990.tb05558.x.
- [100] Trench W. F. “Minimization problems for (R,S)-symmetric and (R,S)-skew symmetric matrices”. In: *Linear Algebra and its Applications* 389 (2004), pp. 23–31. ISSN: 0024-3795. DOI: 10.1016/j.laa.2004.03.035.
- [101] General Description. *DS18B20 Programmable Resolution 1-Wire Digital Thermometer*. <https://www.analog.com/media/en/technical-documentation/data-sheets/DS18B20.pdf>. Accessed: 2023-8-5.
- [102] Ward S. H. and Hohmann G. W. “4. Electromagnetic Theory for Geophysical Applications”. In: *Electromagnetic Methods in Applied Geophysics: Volume 1, Theory*. 1988, pp. 130–311. DOI: 10.1190/1.9781560802631.ch4.
- [103] Tarantola A. *Inverse Problem Theory and Methods for Model Parameter Estimation*. Society for Industrial and Applied Mathematics, 2005. DOI: 10.1137/1.9780898717921.
- [104] Tazifor M., Zimmermann E., Huisman J. A., Dick M., Mester A., and van Waasen S. “Model-Based Correction of Temperature-Dependent Measurement Errors in Frequency Domain Electromagnetic Induction (FDEMI) Systems”. In: *Sensors* 22.10 (2022). ISSN: 1424-8220. DOI: 10.3390/s22103882.
- [105] Tazifor M., Zimmermann E., Huisman J. A., Dick M., Mester A., and van Waasen S. “Low-Pass Filters for a Temperature Drift Correction Method for Electromagnetic Induction Systems”. In: *Sensors* 23.17 (2023). ISSN: 1424-8220. DOI: 10.3390/s23177322.
- [106] Tan X., Mester A., von Hebel C., Zimmermann E., Vereecken H., van Waasen S., and van der Kruk J. “Simultaneous calibration and inversion algorithm for multiconfiguration electromagnetic induction data acquired at multiple elevations”. In: *GEOPHYSICS* 84.1 (2019), EN1–EN14. DOI: 10.1190/geo2018-0264.1.
- [107] von Hebel C., van der Kruk J., Huisman J. A., Mester A., Altdorff D., Endres A. L., Zimmermann E., Garre S., and Vereecken H. “Calibration, Conversion, and Quantitative Multi-Layer Inversion of Multi-Coil Rigid-Boom Electromagnetic Induction Data”. In: *Sensors* 19.21 (2019). ISSN: 1424-8220. DOI: 10.3390/s19214753.
- [108] Campo P. P., Brihuega A., Anttila L., Turunen M., Korpi D., Allén M., and Valkama M. “Gradient-Adaptive Spline-Interpolated LUT Methods for Low-Complexity Digital Predistortion”. In: *IEEE Transactions on Circuits and Systems I: Regular Papers* 68.1 (2021), pp. 336–349. DOI: 10.1109/TCSI.2020.3034825.
- [109] Maxwell J. C. *A Treatise on Electricity and Magnetism*. Cambridge Library Collection - Physical Sciences. Cambridge University Press, 2010.

- [110] Hiptmair R. “Finite elements in computational electromagnetism”. In: *Acta Numerica* 11 (2002), pp. 237–339. DOI: 10.1017/S0962492902000041.

A. Overview of the Maxwell's Equations

The phenomenon of electromagnetic induction follows the principles outlined in Maxwell's equations [109], which provide a comprehensive framework for understanding the generation of electric and magnetic fields through charges, currents, and variations in the fields themselves. In the time domain, the differential form of these equations can be expressed as follows [110]:

$$\nabla \cdot D = q \quad \textit{Gauss' law for electric fields} \quad (\text{A.1})$$

$$\nabla \cdot B = 0 \quad \textit{Gauss' law for magnetic fields} \quad (\text{A.2})$$

$$\nabla \times E = -\frac{\partial B}{\partial t} \quad \textit{Faraday's law} \quad (\text{A.3})$$

$$\nabla \times H = J + \frac{\partial D}{\partial t} \quad \textit{Ampère - Maxwell's law} \quad (\text{A.4})$$

where D represents the dielectric displacement, which is measured in units of Coulombs per square meter (Cm^{-2}), B stands for the magnetic flux density, also known as magnetic induction, and is measured in Tesla (T), E represents the electric field intensity and is measured in volts per meter (Vm^{-1}), H denotes the magnetic field intensity and is measured in Amperes per meter (Am^{-1}), J represents the electric current density, measured in Amperes per square meter (Am^{-2}) and q represents the electric charge density, measured in Coulombs per cubic meter (Cm^{-3}). The divergence and curl operators are denoted by $\nabla \cdot$ and $\nabla \times$, respectively. The dielectric displacement D , the magnetic flux density B and the electric current density J can be described by the following constitutive laws:

$$D = \epsilon E \tag{A.5}$$

$$B = \mu H \tag{A.6}$$

$$J = \sigma E \tag{A.7}$$

where ϵ corresponds to the dielectric permittivity, measured in farads per meter (Fm^{-1}), μ represents the magnetic permeability, measured in henries per meter (Hm^{-1}) and σ represents the electric conductivity, measured in siemens per meter (Sm^{-1}).

B. Static and Dynamic Drift Correction

One of the key challenges in using these meters is dealing with the non-linear relationship between temperature and phase, which can have a significant impact on measurement accuracy. To address this challenge, researchers have developed modeling techniques to capture the non-linear behavior of these meters. One popular approach involves using lookup tables, which provide a static way to represent the non-linear relationship between variables without the need for complex equations.

This is because lookup tables allow for fine-grained control of gradients and interpolating coefficients, which can be adjusted to optimize system modeling. In order to implement a lookup table, it is necessary to determine the control points that define the non-linear relationship between temperature and phase [108]. This can be achieved using a gradient-based algorithm, which allows for the efficient and accurate determination of control points.

Once the control points have been determined, they can be used to create a lookup table that represents the non-linear behavior of the electromagnetic induction soil conductivity meter. The diagram in Figure 4.4 shows the optimisation model whereby only the red path involving the look-up table is used. The parameters that control the model are the gain G and non-linear term NL of the look-up table and the system offset. G and NL are obtained using cubic spline interpolation as discussed in section 3.4.

The objective function defined in Equation 4.5 was used to determine the parameters that minimize the model by evaluating the root mean square error, RMSE. The Nelder-Mead optimisation method was used and the model was applied to a series of 16 temperature data (T_{ms}) measured with the set-up in Figure 4.1.

The plots in Figure B.1 show the measured ECa values over a period of 30 hours for the 16 datasets. To focus on the changes in ECa rather than absolute values, the ECa values were shifted to have a zero mean. It can be seen that across most datasets, the ECa values has a peak to peak value of about ± 20 mSm⁻¹. These measurements were then corrected with the static drift model and the results are depicted in Figure B.2. The ECa values shown were shifted to have a zero mean to focus on the changes in ECa instead of the absolute values.

The optimisation results show the corrected ECa values obtained after static drift

correction with a look-up table. It is observed that the ECa value is usually about $\pm 5 \text{ mSm}^{-1}$. Overall it can be seen that the correction with a static model corrects the measured ECa by a factor of four. The 16 datasets are again fitted, this time with the dynamic drift model with the low pass filter, LPF, (blue path) in Figure 4.1 and using the mean temperature value.

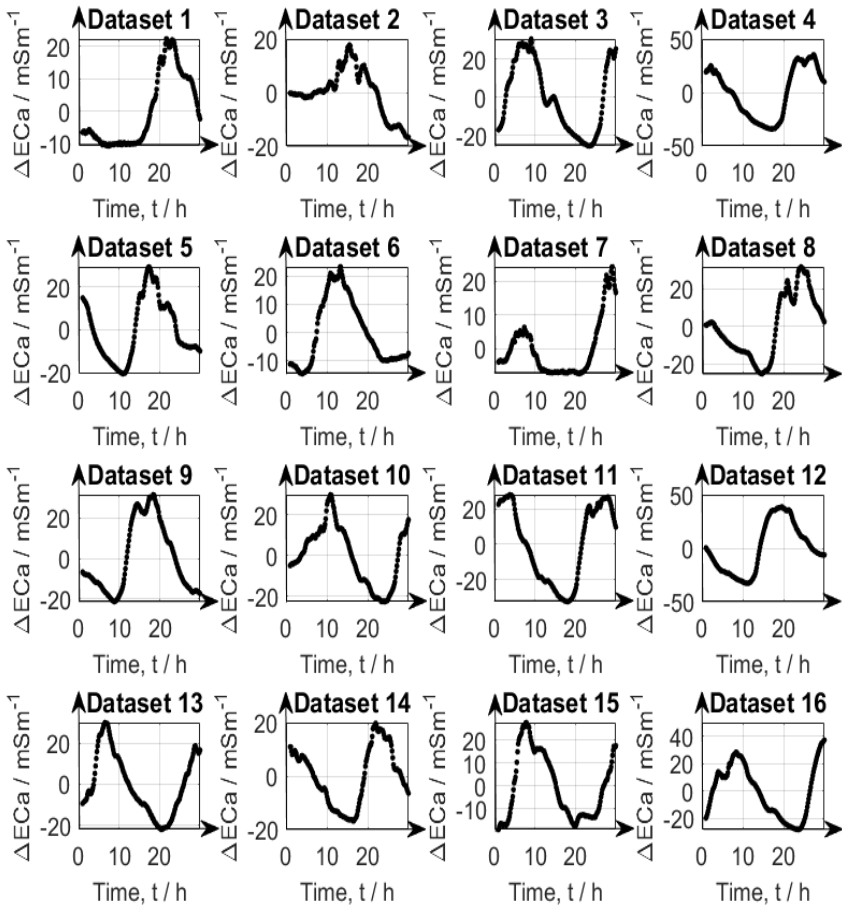


Figure B.1.: Plot of uncorrected ECa over time for 16 datasets.

It is seen from the results in shown in Figure B.3 that the dynamic correction with the LPF offers much improved results. To emphasize the fluctuations in ECa rather

than the exact values, the ECa values presented were adjusted to have an average of zero. Here the corrected ECa values generally have an ECa value of about $\pm 2 \text{ mSm}^{-1}$ across all datasets. These results show that although the typically used look-up table method corrects for static (present) temperature-dependent drift characteristics in EMI devices, the dynamic model based on the LPF offers more accurate results as this takes into account the dynamic (past and present) thermal behaviour of the device.

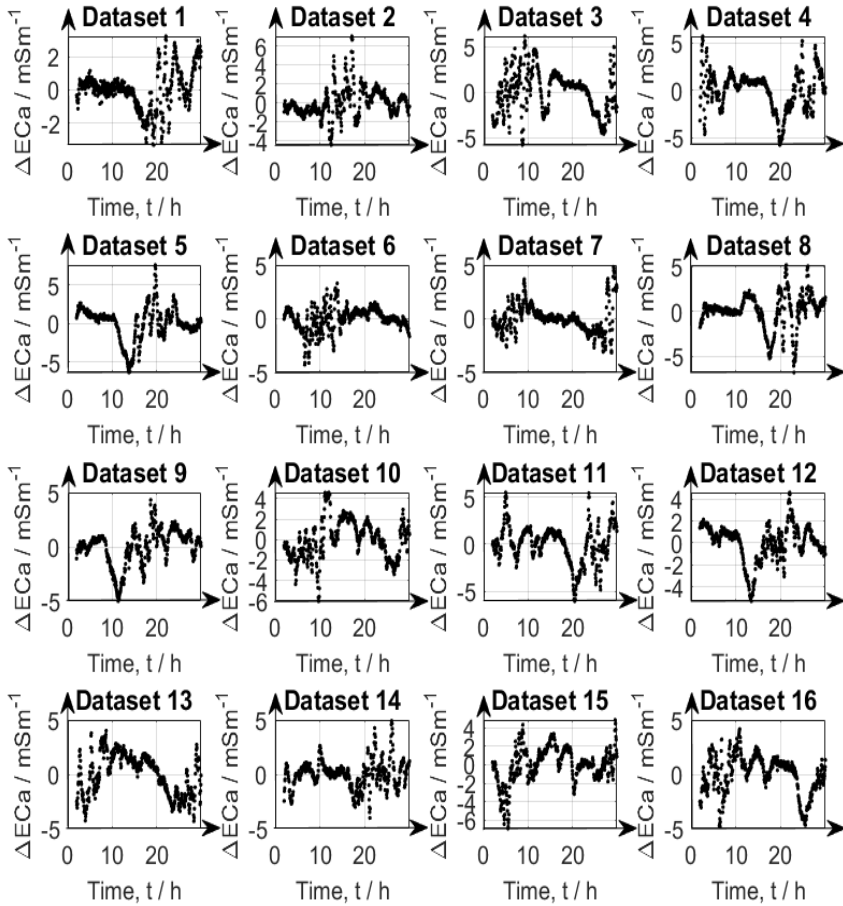


Figure B.2.: Plot of corrected ECa over time for 16 datasets after static correction.

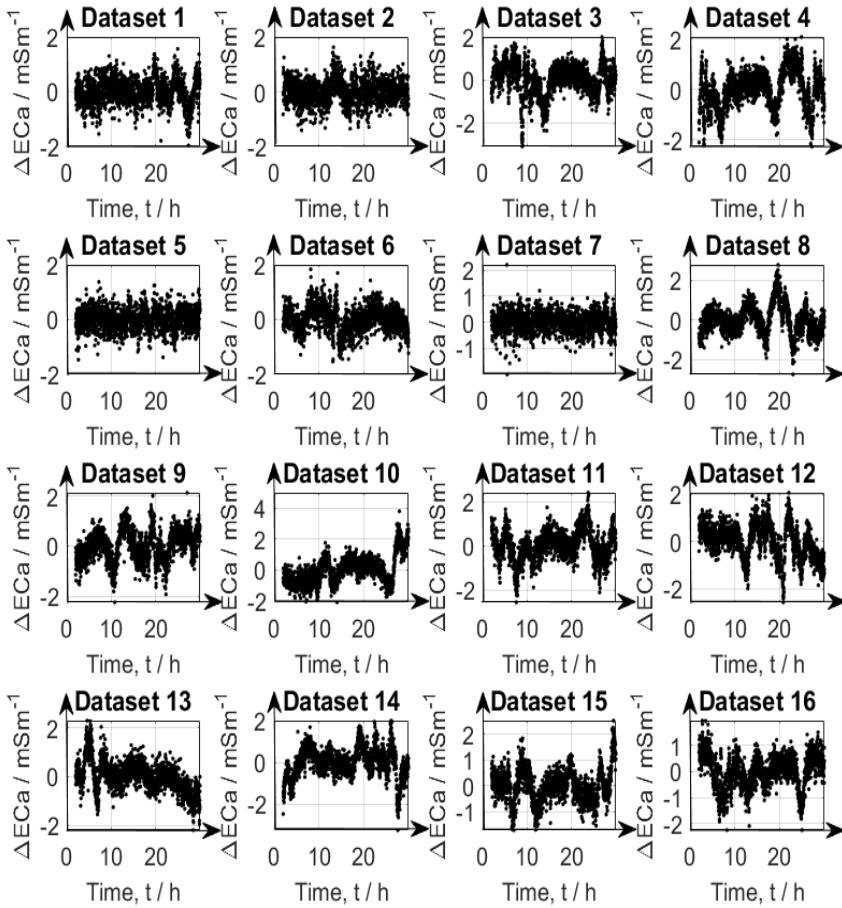


Figure B.3.: Plot of corrected ECa over time for 16 datasets after dynamic correction.

C. Data Optimisation and Parameter Calculation

The 16 datasets in chapter 3 were filtered using the method described in section 5.1.4 to evaluate the the residual eigenvalues $1 - E_{val,1N}$. The plot in Figure C.1 shows that all 16 datasets here have a residual eigenvalue less than 0.0028 which in comparison to the 15 datasets in chapter 4 only correspond to dataset #1.

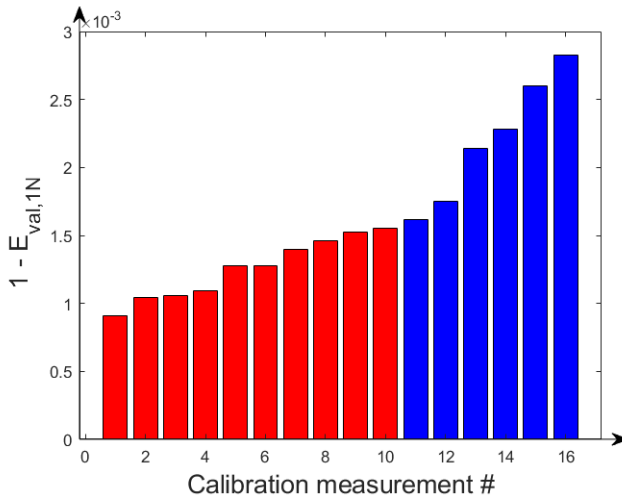


Figure C.1.: Plot of the residual eigenvalues ($1 - E_{val,1N}$) for all datasets obtained from principal component analysis (PCA).

Therefore the temperature data (#2 - 9) classified as UTV datasets in chapter 4 can be considered in reality to have some relative degree of non-linearity in their distribution. This was tested by applying the drift correction model with one LPF introduced in chapter 3 to dataset #5 in Figure 5.4, using the initial calibration parameters in Table 5.1. The results obtained from a simultaneous fit are shown in Figure C.2. In order to place emphasis on the fluctuations of ECa rather than the absolute values, a zero mean was applied to shift the ECa values. The corrected ECa has a value of 10 mSm^{-1} . This indicates that the optimisation with the simplex method does not offer satisfactory results, even for only small degrees of non-linearities in the internal temperature distribution of the EMI system.

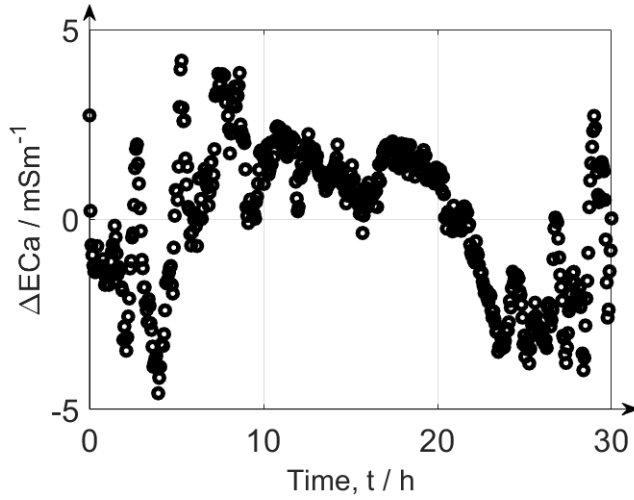


Figure C.2.: Corrected ECa obtained through simplex fitting with 1 LPF.

The 1 LPF drift model is again used to simultaneously fit the same data, with the SCE optimisation this time. The results obtained in Figure C.3 shows that the corrected ECa has a value of 8 mSm^{-1} . This signifies that even with a global optimisation algorithm like the SCE, it is not possible to fit the data, even with the slight non-uniform temperature distribution present.

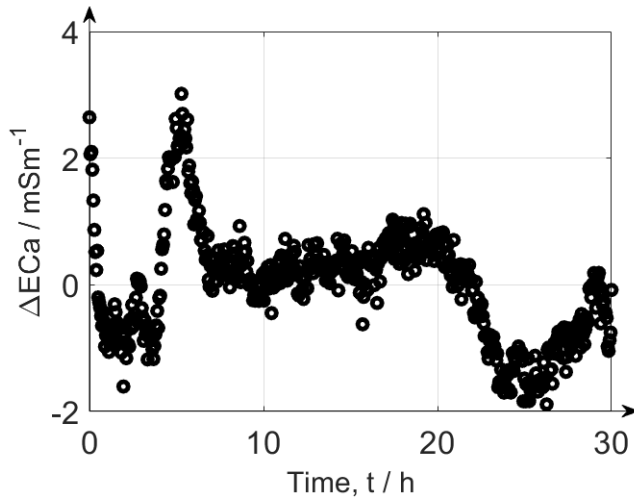


Figure C.3.: Corrected ECa obtained through SCE fitting with 1 LPF.

Next it was tested to see how the 2 LPF drift model in combination with the Nelder-Mead optimisation algorithm now perform with the same dataset. The results were identical to those in Figure C.3 with a corrected ECa value of 10 mSm^{-1} . This confirms the already known fact that when the number of calibration parameters used increases due to addition of a LPF, the Nelder-Mead optimisation gets lost in a local minimum during the fitting run and does not find the global solution. Based on this results, it was concluded that the SCE was the best choice and this was later on confirmed as seen from the results discussed in chapter 4.

Curriculum Vitae

Martial Tazifor Tchantcho

PhD Student in Electrical Engineering

tchantchotazifor@gmail.com

Central Institute of Engineering, Electronics and Analytics,
Electronic Systems (ZEA-2)

www.fz-juelich.de

Wilhelm-Johnen-Straße
52425 Jülich, Germany

Jülich Research Centre

Education

University of Duisburg-Essen

Ph.D. Student, Electrical Engineering, 2020 to 2023

University of Duisburg-Essen

M.Sc., Electrical Engineering, 2019

University of Buea

B.Sc., Electrical Engineering, 2014

St. Joseph's College - Sasse

GCE Advanced Level, 2010

Our Lady Seat of Wisdom College - Fontem

GCE Ordinary Level, 2007

Tenfa Bilingual Primary School - Douala

First School Leaving Certificate, 2003

Professional Experience

Jülich Research Centre, Jülich, Germany

PhD-Student , Zea2, 2020 - 2023

Research Assistant , Zea2, 2019 - 2020

University of Duisburg / Jülich Research Centre, Duisburg / Jülich, Germany

Assistant Lecturer, Measurement and sensor systems, 2021 - 2022

Open Grid Europe GmbH, Essen, Germany

Working Student, Pipeline integrity management, 2019

Master Thesis Student, Pipeline integrity management, 2019

University of Buea, South West Region, Cameroon

Assistant Project Coordinator , Renewable Energy Project, 2015 - 2016

AES Sonel, Douala, Cameroon

Internship, Electrical power plant, 2013 - 2014

Languages

Fluent English

Fluent French

C1 level German

Band / Volume 621

Ceria-based composites for application in Oxygen transport membranes

L. Fischer (2024), xiii, 216 pp

ISBN: 978-3-95806-739-4

Band / Volume 622

Investigations of Air Quality Aspects with the Urban Climate Model PALM4U

R. Wegener, U. Javed, R. Dubus, and D. Klemp (2024), 93 pp

ISBN: 978-3-95806-741-7

Band / Volume 623

The Chemical Budget of Radicals and Reaction Mechanisms of the Atmospheric Oxidation of Monoterpenes Investigated in the Atmospheric Simulation Chamber SAPHIR

Y. S. Pang (2024), VI, 158 pp

ISBN: 978-3-95806-742-4

Band / Volume 624

Optimizing spectral electrical impedance tomography technology for improved subsurface characterization

H. Wang (2024), xxix, 113 pp

ISBN: 978-3-95806-744-8

Band / Volume 625

On a multi-spectral method for measuring aerosol properties, suitable for operation on iagos passenger aircraft

P. Weber (2024), ca 123 pp

ISBN: 978-3-95806-746-2

Band / Volume 626

Modellierung der flächendifferenzierten Grundwasserneubildung für Schleswig-Holstein

Endbericht

I. McNamara, B. Tetzlaff, T. Wolters, F. Wendland (2024), 96 pp

ISBN: 978-3-95806-748-6

Band / Volume 627

Modeling orographic gravity waves from source to termination to improve parameterization schemes in climate models

S. Rhode (2024), xii, ii, 138 pp

ISBN: 978-3-95806-750-9

Band / Volume 628

**Abscheidung kolumnarer Wärmedämmschichten mittels
Suspensionsplasmaspritzen (SPS) und Plasma Spray – Physical Vapor
Deposition (PS-PVD) Prozess**

J. Joeris (2024), vii, 133 pp

ISBN: 978-3-95806-752-3

Band / Volume 629

**Structure and properties of electrochemical interfaces
from first principles simulations**

R. Tesch (2024), xvi, 161 pp

ISBN: 978-3-95806-753-0

Band / Volume 630

Elucidation of Barocaloric Effect in Spin Crossover Compounds

H. Shahed (2024), x, 261 pp

ISBN: 978-3-95806-758-5

Band / Volume 631

**Computational Investigation of Solvation Phenomena
at Metal-Electrolyte Interfaces**

O. Cheong (2024), xvii, 142 pp

ISBN: 978-3-95806-759-2

Band / Volume 632

**Senkung zukünftiger Stickoxid- und Partikelemissionen in Nordrhein-
Westfalen durch den Einsatz alternativer Energieträger und Antriebe**

J. L. Breuer (2024), vii, 339 pp

ISBN: 978-3-95806-760-8

Band / Volume 633

**Development of Model-Based Correction Methods for Temperature-
Dependent Electromagnetic Induction (EMI) Measurement Errors in Soil
Conductivity Estimations**

T. M. Tchantcho Amin (2024), xx, 100 pp

ISBN: 978-3-95806-761-5

Energie & Umwelt / Energy & Environment
Band / Volume 633
ISBN 978-3-95806-761-5